Atomic Layer Deposited 3D Nanostructured Materials for Efficient Energy Storage

Submitted in partial fulfillment of the requirements

of the degree of

Doctor of Philosophy

By

Arpan Kumar Dhara

(Roll No. 10I17007)

Supervisors:

Prof. Shaibal K. Sarkar

Prof. Sagar Mitra



Department of Energy Science and Engineering

Indian Institute of Technology Bombay

2019

Declaration

I declare that this written submission represents my ideas in my own words and where other ideas or words have been included, I have adequately cited and referenced the original sources. I also declare that I have adhered to all principles of academic honesty and integrity and have not misrepresented or fabricated or falsified any idea/data/fact/source in my submission. I understand that any violation of the above will be cause for disciplinary action by the Institute and can also evoke penal action from the sources which have thus not been properly cited or from whom proper permission has not been taken when needed.

Arpan Kumar Dhara

Roll No.: 10I17007

Date:

Abstract

The rapid advancement in the field of nanotechnology in the past several years has promised great potential for controlling materials at the nanoscale and stimulated vast opportunities to architect materials with desirable properties. This evolution has also contributed significantly to the development in the area of energy storage, which is a crucial technology in the present time. Electrode architecture always plays an important role in the domain of energy storage. In specific, engineering at nanoscale offers exclusive properties resulting in an improvement in the performance of electrodes and electrolytes in different energy storage technologies. Accordingly, significant efforts have been put forward in recent years to accomplish the present demands of energy storage using these advanced nanostructured materials. Various nanostructured materials with larger surface area and low bulk volume are presently being studied to improve the energy and power densities together for next-generation storage devices.

The main objective of this thesis is to develop three-dimensional (3D) nanostructured electrodes with superior energy density and power density for electrochemical energy storage. Controlling the thickness of the active material in a few nanometers ensures the short diffusion length and full utilization of the active material. To get the nano level control, the ALD technique is used for active material deposition. Highly conducting templates like CNTs, graphenes and metal nanostructures are utilized to anchor the active material ensuring the effective electron transportation. Three-dimensional electrodes represent a unique way to improve the storage density and rate capability without the complex process of material development.

This thesis presents the synthesis of 3D hybrid nanostructured electrodes with superior energy density and power density for electrochemical energy storage using template assisted methods. Carbon nanotubes (CNT) and Cu-NWs are used as template layer because of their high surface area and electrical conductivity. The active material is being deposited on these template layers by atomic layer deposition (ALD) process because of its extreme conformal and sub-nanometer thickness control.

Due to its high theoretical capacity, energy density and excellent reversibility with Li/Li^{+}, molybdenum oxides are one of the vastly studied electrode material in lithium-ion batteries.

However, like most of the oxides, it also suffers from poor cyclic stability because of their low electrical conductivity. In 3D core-shell structure prepared by ALD coating provide superiority in nanoscale decoration because of its extreme conformality and precise thickness control on high aspect ratio surfaces. The first part of this thesis focuses on the fabrication and electrochemical activities of 3D CNT/MoO_x electrodes. These electrodes exhibit much higher areal and overall cell capacity than its planer 2D counterpart. An optimal thickness of MoO_x on CNT is also found out in order to attain the most stable cyclic performance of this nanostructure. A stable reversible areal capacity of 645 µAh cm^{-2} with a specific capacity of 915 mAh g^{-1} is achieved from optimized MoO_x/CNT assembly.

The second part of the thesis focuses on increasing the conductivity of the MoO_x layer by N-incorporation for better electrochemical performance. It is well studied that the transition metal oxynitrides have better conductivity than their pure oxide phase. This particular work highlighted three important factors, (i) synthesis, (ii) electron transportation and (iii) electrochemical performances of N-incorporated MoO_x films. It is found that N-atoms are homogeneously distributed throughout the films at the deposition temperature, no post-annealing is required for diffusion. The conductivity of those films increases with increasing nitrogen concentration. The electrochemical study reveals the superior performance of N-incorporated films against Li/Li^+ than that of the pristine materials. The highest discharge capacity of 1287 mAh g^{-1} was achieved in the first cycle at a current rate of 0.1 A g^{-1} and a stable capacity of 974 mAh g^{-1} and 610 mAh g^{-1} achieved when discharged at 0.1 and 2 A g^{-1} from the core-shell 3D CNT/MoO_x:N electrodes.

In the final part, Cu-nw scaffold is used as template layer by replacing CNTs. The high abundance, low-cost and high electronic conductivity make the choice simpler to use Cu as an affordable scaffold layer. Cu/ MoO_x electrode showed a stable capacity of 993 mAh g^{-1} at the rate of 0.1 A g^{-1} and retained 45% of its initial capacity with 40 times higher current rate. This kind of state-of-the-art fabrication method helps to deposit more amount of active material with less Li^+ diffusion length and ease the electron/ion transportation during the charge-discharge process.

Table of Contents

List of Figures ix
List of Tables xiv
Abbreviations xiv

1 Chapter 1 Introduction and Literature Review 1

1.1 Importance of nanostructured materials in the energy field 3
1.2 Lithium-ion battery (LIB) 3
1.3 Supercapacitor 5
1.4 Atomic layer deposition (ALD) for electrochemical energy storage 6
1.4.1 Atomic layer deposition 6
1.4.2 Why ALD for energy storage process? 6
1.5 Motivation 7
1.6 The aim of the thesis 7
1.7 Layout of the thesis 8
1.8 Literature review 9
1.8.1 Fundamentals of ALD 9
1.8.2 Utilizing ALD technique for electrochemical storage 17
1.8.3 MoO_3 as anode material in LIB 23
1.8.4 Electrochemical activity of molybdenum oxynitrides 24
1.9 References 27

2 Chapter 2 Experimental Techniques and Characterizations 41

2.1 Material Synthesis 43
2.2 MWCNT pre-treatment and deposition 45
2.3 Material characterizations 45
2.3.1 *In-situ* characterization 46
2.3.2 *Ex-situ* characterizations 48
2.3.3 Li-ion cell fabrication and electrochemical characterization 50
2.4 References 52

3 Chapter 3 Controlled 3D Carbon Nanotube Architecture Coated with MoO_x Material by ALD technique: A High Energy Density Lithium-ion Battery Electrode 53

3.1 Experimental 55
3.1.1 ALD of MoO_x 55
3.1.2 MWCNT pre-treatment and deposition 55
3.1.3 Electrochemical cell fabrication 56
3.2 Results and Discussions 56
3.2.1 Growth study by *in-situ* QCM 56
3.2.2 Residual gas analysis (RGA) 58
3.2.3 Film characterization 59
3.2.4 Electrochemical Characterization 61
3.3 Conclusion 70
3.4 References 72

4 Chapter 4 Development of Nitrogen Incorporated Molybdenum Oxide by Atomic Layer Deposition and Its Enhanced Electrochemical Activity . 75

4.1 Experimental 77
4.2 Results and discussions 77
4.2.1 *In-situ* QCM study 77
4.2.2 Secondary ion mass spectrometry (SIMS) and energy diffractive area X-ray (EDAX) elemental mapping 78
4.2.3 X-ray photoelectron spectroscopy (XPS) 79
4.2.4 Raman spectra 79
4.2.5 Ultraviolet photoelectron spectroscopy (UPS) 80
4.3 Electrical Characterization 81
4.4 Electrochemical characterization 85
4.5 Conclusion 91
4.6 References 93

5 Chapter 5 Cu-Nw Template Based 3D Nanostructure Electrode for LIB 97

5.1 Results and discussions 100
5.1.1 Synthesis and characterization of Cu-nw and MoOx@Cu-nw structure 100
5.1.2 Prevention of Copper oxidation 104
5.1.3 Electrochemical characterization 105
5.2 Conclusions 107

6 Chapter 6 Summary and Future Sopes 111

6.1 Summary and conclusions 113

6.2 Future scopes 114

7 Appendix-I Two-Stage Chemical Bath Deposition of Moo_3 Nanorod Films 115

7.1 Experimental 117

7.2 Results and discussions 117

7.3 Conclusions 125

7.4 References 126

8 Appendix-II Low-Temperature Fabrication of Coaxial ALD Cobalt Oxide Coated Carbon Nanotubes and Their Pseudocapacitive Behaviour 127

8.1 Experimental 129

8.2 Results and Discussion 130

8.3 Conclusion 136

8.4 References 136

List of publication 137

Acknowledgement 139

List of figures

Figure 1.1 Schematic representation of a lithium-ion battery 5

Figure 1.2 Schematic of a complete ALD cycle. 11

Figure 1.3 (a) Typical self-saturated growth characteristic as a function of precursor exposure during ALD and (b) Possible growth behavior as a function of temperature during ALD 12

Figure 1.4 Surface modification of LIB electrodes by ALD. a) SEM image of Al_2O_3 coated $LiCoO_2$, b) cycling performance of bulk $LiCoO_2$, uncoated nano-$LiCoO_2$, and Al_2O_3 coated nano-$LiCoO_2$.[71] c) cycling performances of $LiNi_{0.5}Mn_{1.5}O_4$/graphite cells with different coatings: uncoated, $LiAlO_2$ and Al_2O_3 coated.[76] 18

Figure 1.5 Surface modification of V_2O_5 supercapacitor electrodes. a) SEM image of 100 cycles of ALD V_2O_5 coated CNTs and b) Specific capacitance of CNTs samples coated with 100, 300, and 500 cycles of ALD V_2O_5.[96] 20

Figure 1.6 a) SEM and b) TEM images of ALD $LiFePO_4$ coated CNT, c) Cycling performance of the CNT@$LiFePO_4$ cathode for lithium storage.[113] d) SEM image and e) cycling behavior of ALD TiO_2 coated carbon cloth/carbon nanowire as a LIB anode.[114] 22

Figure 2.1 Block diagram of custom-built ALD reactor setup used for film deposition. 43

Figure 2.2 photograph of the custom build ALD reactor used for this work 44

Figure 2.3 Photograph of QCM holder arrangement used for *in-situ* studies 46

Figure 2.4 Schematic representation of different parts of a 2032 coin cell 51

Figure 3.1 Schematic representation of different thickness MoOx coating on porous CNT layer. ALD helps to form a uniform and conformal MoO_x layers without disturbing the interconnected CNT mesh structure. With increasing the number of ALD cycles the thickness of the MoOx layer gets increases and the porosity of the layer decreases. 56

Figure 3.2 (a) Mass gain with ALD cycles monitored by *in-situ* QCM at a substrate temperature of 170 ^{0}C, (b) mass change during $Mo(CO)_6$ and O_3 precursors dose at 170 ^{0}C, (c) growth rate *vs.* no. of $Mo(CO)_6$ dose and (b) mass change with substrate temperature variation. 58

Figure 3.3 RGA spectra recorded right after $Mo(CO)_6$ and ozone dosing 59

Figure 3.4 (a) XPS survey of as ALD MoO_x film on Si substrate, (b) high-resolution Mo 3d core level XPS scan, (c) Raman spectrum of as-deposited MoO_x film and (d) de-convoluted Raman peaks in the range of 600-1100 cm^{-1}. 60

Figure 3.5 Cyclic voltammetry of commercial MoO_3 powder at a scan rate of 10 μV/S in the range of (a) 3-0 V and (b) 3-0.6 V vs Li/Li^+. (c) ex-situ XRD study of MoO_3 electrodes at a different potential and (d) ex-situ XPS Mo-3d profile of MoO_3 electrodes at different potentials. 62

Figure 3.6 (a) XRD and XPS spectra of commercial MoO_3 powder (3-0.6 V range) at a different potential (b) XPS peaks of O-1S and Li-1S at a different stage of lithiation and delithiation. 62

Figure 3.7 cyclic voltammograms of (a) an as-deposited bare MoO_x electrode and (b) a MoO_x/MWCNT electrode at a scan rate of 0.2 mVs^{-1} within a potential window of 3-0.1 V against Li/Li^+..... 64

Figure 3.8 electrochemical characterization of as-deposited MoO_x grown on SS substrate. (a) Areal discharge capacity and (b) 1st cycle charge-discharge profiles of 100, 300, 500 and 1000 cycle MoO_x electrodes, (c-d) show the SEM images of a 1000 ALD cycle before and after cycling and (e) Coulombic efficiency of all four samples. 65

Figure 3.9 SEM images of MWCNTs after different ALD cycles (0, 100, 300, 500 and 1000) of MoO_x coating. 66

Figure 3.10 Electrochemical comparison of different MoO_x/MWCNT electrodes. (a,b) areal and specific capacity comparison, (c) 1st cycle charge-discharge profiles, (d) Coulumbic efficiency and (e) rate performance of 100, 300, 500 and 1000 cycle MoO_x/MWCNT 68

Figure 3.11 (a) cyclic voltammogram and (b) charge-discharge characteristics of bare CNT electrodes. 69

Figure 3.12 (a) Scanning electron microscope images of 100, 300, 500 and 1000 cycle MoO_x/MWCNT electrodes after 50th charge-discharge cycle and (b) TEM images of 100 ALD cycle MoO_x/MWCNT electrode before and after 50 charge-discharge cycles. 70

Figure 4.1 (a) A schematic of the film stack used for growing different compositions of nitrogen-doped MoO_x films by ALD. (b) In-situ QCM results showing mass gain after various doses of precursor deposition at 170 °C..... 78

Figure 4.2 (a) TOF-SIMS spectra of MoOx:N (9:1) film deposited on Si substrate showing Mo, O, N, and Si elemental count profiles; (b) EDAX elemental mapping of Mo, O, and N atoms in the MoO_x:N film..... 79

Figure 4.3 (a) XPS profile of Mo 3d in and (b) Raman spectra of MoO_x, N-incorporated MoO_x and MoN_x films.....80

Figure 4.4 UPS spectra of different nitrogen incorporated MoO_x films plotted with respect to Fermi level- (a) Magnified view of valence band onset, (b) full spectrum, (c) close view of secondary electron cut-off and (d) schematic of tentative energy level alignment diagram....81

Figure 4.5 Room-temperature resistivity and electron density as a function of R_{NH3}.....82

Figure 4.6 Variation in thermal emf (dV in Volts) with temperature difference (dT in K) between hot and cold probes for (a) a pristine and (b) N-incorporated films. 82

Figure 4.7 (a) Temperature-dependent resistivity curves for different MoO_x:N samples. The inset shows resistivity plots to extract the activation energy in a high-temperature regime. Vertical arrows indicate the temperature at which the $\rho(T)$ curve deviates from the activation behavior, (b) Variation in sub-bandgap absorption ($h\nu<E_g$) for different N-incorporated samples. The solid line indicates the measured data fitted according to the Urbach equation. The inset shows the extracted Urbach energy values as a function of R_{NH3}. 83

Figure 4.8 Optical transmittance spectra of all N-incorporated films grown on quartz substrates 84

Figure 4.9 Variation of lnρ as a function of $(1/T)^{1/4}$. The linear behavior implies the dominance of Mott variable range hopping conduction in the low-temperature range.....85

Figure 4.10 (a) CV of a N-incorporated MoO_x, bare MoO_x and MoN_x films in the first cycle and (b) CV of a MoO_x:N electrode in 2nd and 3rd cycle, (c) charge-discharge capacities, Coulombic efficiency and (d) 1st cycle lithiation-delithiation voltage profiles of different electrodes vs Li/Li+. 87

Figure 4.11: Cyclic voltammogram of (a) MoOx, and (b) MoNx in the 1st, 2nd and 3rd cycle 88

Figure 4.12 (a) Schematic representation of CNT and MoO_x@CNT structure, (b) SEM images of CNTs after MoO_x (or MoO_x:N) coating, (d) rate performance of CNT/MoOx and CNT/MoOx:N electrodes at different current rate and (e) electrochemical impedance spectra of CNT/MoOx and CNT/MoOx:N at OCP, (f) galvanostatic charge-discharge cycling and Coulombic efficiency of CNT/MoOx:N electrode, (d) Charge-discharge profiles of CNT/MoOx:N electrodes for few initial cycles at 0.1 A g^{-1}. 89

Figure 5.1 (a) Graph of fraction f of Zn(I1) existing as Cu^{2+}(aq), $Cu(OH)^{+}$(aq), $Cu(OH)_2$(aq), $Cu(OH)^{3-}$, and $Cu(OH)_4^{2-}$(aq) over a range of pH at 25 ^{0}C; (b) photograph of Cu-nw formed during reaction and (c) optimized bath condition for Cu-nw synthesis. 100

Figure 5.2 SEM images of Cu NWs obtained from different EDA and HZ concentration where other parameters are kept constant 101

Figure 5.3 SEM images of (a,b) as synthesized Cu nw, (c,d) ALD MoO_x coated Cu nw and (e) XRD of as-prepared Cu-nw and 300 cycles MoO_x coated Cu-nw 102

Figure 5.4 High-resolution TEM images of (a) Cu-nw and (b) MoO_x@Cu-nw..... 103

Figure 5.5 HRTEM images of (a) Cu-nw and (b) Cu-MoO_3 interfaces 103

Figure 5.6 Figure 5.7 (a,b) SEM images of pristine and MoO_x coated Cu-sheet respectively and (c,d) XRD of MoO_x coated Cu-sheet and log plot of the same plot respectively 104

Figure 5.8 protection of Cu from oxidation. (a) XRD of MoO_x/Cu without protecting layer, MoO_x/Cu with AlO_x (20cyl) protection and MoO_x/Cu with MoN_x (30 cyl) protection (b) TEM image of MoNx protection layer sandwiched between Cu and MoO_x layer 105

Figure 5.9 Electrochemical activities of a 200 cycle MoO_x ALD coated Cu electrode. (a) Cyclic voltammograms of the electrode with and without protection, (b) charge-discharge cycling, (c) rate performance at different current densities and (d) in-situ electrochemical impedance spectroscopy at different potential during charge-discharge. 106

Figure 7.1 (a) XRD pattern of the as-deposited films obtained from 0.1 M HMA and 5.2 M HNO_3 in the Bragg–Brentano configuration. (b) SEM micrograph revealing hexagonal rod-like morphology of the deposit. (c) The TEM image and SAED pattern showing mono crystallinity of the individual rods. 118

Figure 7.2 Schematic representation of single stage and double stage deposition process of h-MoO_3 nanorod films..... 119

Figure 7.3 (a) XPS Mo peaks obtained from an as-deposited film (b) FTIR transmission spectra showing N–H and O–H stretching and bending vibrations of as-deposited and air-annealed (at 200 ^{0}C) samples. 119

Figure 7.4 Scanning electron micrograph of the films obtained with (a) 0.1 M, (b) 0.065 M and (c) 0.05 M HMA concentration. The HNO_3 concentration was constant at 5.2 M..... 119

Figure 7.5 Mo 3d XPS spectrum after the 1st stage 120

Figure 7.6 SEM images of the as-deposited films obtained from (a) 0.1 M, (b) 0.065 M (c) 0.025 M and (d) 0.01 M of HMA. 121

Figure 7.7 SEM images of the films obtained from (a) fresh solution and (b) 30 min aged solution for the 2nd stage deposition. The first stage deposition was kept unaltered at 30 min (the inset shows the cross-section micrograph of the same films). 122

Figure 7.8 SEM image of the films obtained from (a) 2 min, (b) 5 min, (c) 10 min (d) 20 min (e) 30 min and (f) 45 min of 1st stage deposition while the 2nd stage deposition was kept unaltered. 123

Figure 7.9 Distribution of nanorod diameters of the films obtained from 2 min, 5 min, 10 min, 20 min, 30 min and 45 min of 1ststage deposition while the 2nd stage deposition is kept unaltered. 125

Figure 8.1 Schematic representation of different CoO_x coatings on porous MWCNT layer. As deposited MWCNT layer forms an interconnected mesh kind of structure. ALD helps to deposit cobalt oxide on the free CNT surfaces. Interconnections remain undisturbed after deposition 130

Figure 8.2 RGA spectra recorded after 1st dose of $[Co_2(CO)_8]$, 1st dose of O_3 and 2^{nd} dose of $[Co_2(CO)_8]$ 131

Figure 8.3 (a) Grazing incident XRD of as-deposited film, (b) XPS survey of the as-deposited and inset showing the 2p peaks of Cobalt and (c) Raman spectra of MWCNT and CoO_x@MWCNT 132

Figure 8.4 surface SEM images of different CoO_x/MWCNT electrodes 133

Figure 8.5 (a,b) TEM images of CoO_x/MWCNT structure showing the core-shell structure throughout all the MWCNTs, (c) SAED pattern of MWCNT and CoO_x/MWCNT sample .. 134

Figure 8.6 (a) CV curves of MWCNT, 30cyl, 50cyl and 100cyl at 5mV/s, (b) 30cyl CV at different voltage sweep rate, (c) GCD graph of all four device at 0.5 mA/cm^2, (d) 30cyl GCD curves at different current loads, (e) Ragone plot showing energy and power density of all four symmetric device. 135

List of tables

Table 1-1 List of materials grown by ALD[30] 11

Table 1-2 Comparison of deposition temperatures using halide and organic based precursors 16

Table 3-1 comparison of C-rate and areal capacity for all the electrodes..... 68

Table 3-2 Electrochemical performance comparison of MoO_3 anodes used recent times in Li-ion batteries 71

Table 4-1 electrochemical performance comparison of CNT/MoO_x:N amd CNT/MoO_x electrodes 90

Table 4-2 Comparison of MoO_3 anodes used in Li-ion batteries by recent literature 92

Abbreviations

ALD	Atomic Layer Deposition
ALE	Atomic Layer Epitaxy
BE	Binding Energy
CBD	Chemical Bath Deposition
CNT	Carbon Nanotube
CV	Cyclic Voltammogram
CVD	Chemical Vapour Deposition
DI	De-Ionized
EDAX	Energy-Dispersive X-Ray Analysis
EIS	Electrochemical Impedance Spectroscopy
ELDC	Electric Double Layer Capacitor
FESEM	Field-Emission Scanning Electron Microscopy
FTIR	Furrier-transform Infrared
FTO	Fluorine Doped Tin Oxide
GCD	Galvanostatic Charge-Discharge
GITT	Galvanostatic Intermittent Titration Technique
HMA	Ammonium Heptamolybdate
HPLC	High Performance Liquid Chromatography
HRTEM	High-Resolution Transmission Electron Microscope
LIB	Li-Ion Battery

MEMS	Micro-Electro-Mechanical Systems
MWCNT	Multi-Walled Carbon Nanotube
OCP	Open Circuit Potential
PE-ALD	Plasma-Enhanced Atomic Layer Deposition
PID	Proportional–Integral–Derivative
QCM	Quartz Crystal Microbalance
RGA	Residual Gas Analysis
SAED	Selected Area Electron Diffraction
SEI	Solid Electrolyte Interface
SEM	Scanning Electron Microscope
SIMS	Secondary-Ion Mass Spectroscopy
SS	Stainless Steel
TEM	Transmission Electron Microscopy
UPS	Ultra-Violet Photon Spectroscopy
WF	Work Function
XPS	X-Ray Photoelectron Spectroscopy
XRD	X-Ray Diffraction
XRR	X-Ray Reflectivity

Chapter 1

Introduction and Literature Review

This chapter can be divided into two parts. The first part introduces the importance of nanomaterials and their application is energy field along with the brief introduction of ALD and different energy storage methods. Motivation and objectives of the thesis are also discussed here. The second part discusses the literature review of the ALD processes and their application in energy storage.

1.1 Importance of nanostructured materials in the energy field

Nanomaterials can be generally defined as a physical substance having dimensions in the range from 1-1000 nm with a very high surface-to-volume ratio.[1] These materials (like nanowires, nanotubes, nanoparticles, nanosheets, nanofilms etc.) are of immense elementary and technological interest, as they essentially bridge the gap between sub-atomic and bulk properties of a material. Fundamental properties (like electrical,[2] optical[3,4] and magnetic[5]) of a nanomaterial can be varied depending upon its size[6] and shape[7]. Apart from many other applications, nanomaterials have significant importance in energy harvesting and storage devices.[8–10]

Due to their high surface-to-volume ratio, nanomaterials provide vital improvement possibilities in both conventional[11] and renewable energy technologies.[9,12] Employment of nanomaterials in new generation solar cells extends promises to reduce the cost of photovoltaic devices with an improved photon to the electrical energy conversion efficiency.[13] On a similar note, photocatalytic water splitting using nanomaterials make the process more efficient. Of interest to the current work, nanostructured materials also have a significant influence on major advancements in energy storage, in lithium-ion batteries (LIB) and supercapacitors.[10,14] Performance of electrochemical devices can be enhanced using nanomaterials by employing their higher surface electrochemical reactions and heterogenic catalytic interactions.[15] Significant changes in the surface reaction rates and electrical or ionic transport of the material cause a remarkable improvement in energy generation and storage.

1.2 Lithium-ion battery (LIB)

An electrochemical energy storage device is capable of storing and producing electric energy through chemical reactions. Batteries are the most traditional electrochemical energy storage devices and can be classified into two categories; primary and secondary batteries. Primary batteries are mainly designed for single use and cannot be recharged for example alkaline batteries, whereas secondary batteries are rechargeable.

Among other rechargeable batteries, LIB is found, though often argued, to be one of the most promising and commercially viable technologies in the present time because of its high volumetric energy density. In these devices, Li^+ ions move from negative electrode (anode) to positive electrode (cathode) while discharging and vice-versa during charging. Schematic

representation of a LIB is given in Figure 1.1. Cathodes mainly consist of intercalated lithium-containing metal oxides (like $LiCoO_2$, $LiMnO_2$, $LiFePO_4$ etc.).[16] These metal oxide framework structures have a specific location inside the crystal where lithium ions can be intercalated during discharge or extracted easily during charging without distorting the crystal structure. In the case of $LiCoO_2$, which has a layer-by-layer structure, Li^+ intercalates between two consecutive layers. Most commercially used cathode material is $LiCoO_2$ because of its high energy density and better cycle lifetime. However, high cost and toxicity involve in cobalt make researchers turn their attention into other possible replacements. $LiMnO_2$ henceforth is found to be the alternative due to its low cost, high availability and easy synthesis method. But, its relatively lower stability with cycling found to be a major bottleneck for commercial application. As a general note, the requirement for ideal cathode material would be abundance, affordable and safe in continuous usage .[17,18]

As an anode material, graphite is the most commonly used in commercial LIBs. In an idealized structure, one lithium-ion for every six carbon atoms (LiC_6) can be stored, which corresponds to a specific discharge capacity of 372 mAh g^{-1}. In principle, all carbonaceous materials containing sp and sp^2 hybridized carbon are capable of storing lithium. However, the layered structure of graphite makes it more suitable for Li^+ intercalation. The amount of Li^+ intake into different carbonaceous materials varies depending on the crystal structure, surface area and shape of the particles. Apart from graphite, most commonly used carbonaceous materials are carbon nanotube, graphene, mesoporous carbon etc. Although carbonaceous materials are good options for anode material, they suffer from low discharge capacity and the formation of Li dendrites during rapid charge-discharge because of the similar reduction potential as Li-metal.[19] To overcome these drawbacks and improve energy storage, a new anode material with high capacity and better electrochemical stability is desired.

Drawbacks of the above prospectively overcome in transition metal oxides and its derivatives.[20] These oxides are generally conversion based materials, where metal oxides react with lithium to form metal particles (M) and corresponding lithium compound (Li_2O). They usually possess considerably high capacity and excellent reversibility with Li/Li^+ system. The main disadvantages of this kind of material are their insulating nature and low Li^+ ion diffusion in the bulk of the material. Low bulk volume of nanoparticles helps to counteract Li^+ ion diffusion problem and provide a larger surface for better reactivity and reversibility.

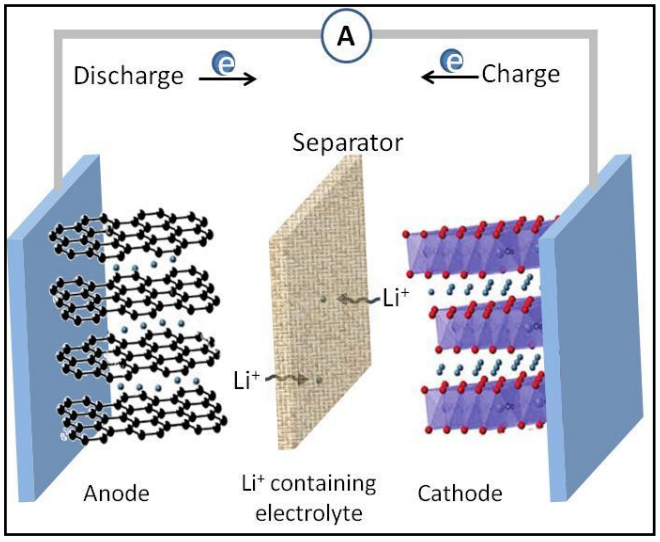


Figure 1.1 Schematic representation of a lithium-ion battery

1.3 Supercapacitor

Supercapacitors are another type of devices that electrochemically store energy either through absorption-desorption of ions or through fast reversible surface Faradic reactions or a combination of both. These devices possess much higher power densities but lower energy densities in comparison to batteries.[21] Thus, it bridges the gap between the battery and the electrostatic capacitor. It can store 2-3 orders of magnitude more energy than electrostatic capacitor and able to charge-discharge much faster than the battery. Rapid charge-discharge reversibility (in few seconds) is the major advantage of such kind of devices makes them useful for short term high energy applications.[22,23] Supercapacitors also have the similar configuration like batteries, two active electrodes separated by a separator. Both aqueous and non-aqueous electrolyte can be used for them. Aqueous electrolyte limits the maximum working potential of a device to 1.2 V, above which water will dissociate. Non-aqueous electrolytes can be used for higher potential.[24]

Transition metal oxides (*e.g.* MnO_2, RuO_2, NiO, Co_3O_4) are also one of the major domain for supercapacitor materials because of their excellent redox reversibility leading higher capacity. However their poor electronic conducting found to be the major bottleneck in long term usage. Low dimensional thin metal oxide particle with very less ionic diffusion length can solve the problem to a better extent.[25,26] A few nanometers of active material coating on the high surface area conducting template layer like carbon nanotubes, graphene, activated carbon, carbon

aerogel and porous carbon can also be a reasonably prospective solution. Yet, such deposition processes are not trivial.[27,28]

1.4 Atomic layer deposition (ALD) for electrochemical energy storage

The importance of nanostructure materials in energy applications is discussed previously. One of the simplest and effective solutions for high energy and power density storage is the fabrication of nanostructured electrodes which helps in loading a higher amount of active material with enhanced reaction kinetics. Different deposition techniques are there *e.g.* sol-gel, solvothermal, electrodeposition etc. to coat high surface area carbonaceous materials. Most of the above methods do not have appropriate control over deposition and more often suffer from non-uniformity issue. Whereas, vapour phase techniques have shown superiority in terms of the control and uniformity of the deposited material over the extremely high surface area.

1.4.1 Atomic layer deposition

ALD is a self-limiting thin film deposition technique based on sequential exposure of gaseous precursors. In a typical ALD reaction, precursors are dosed consecutively into the reaction chamber and separated by a purging of inert gas. When a precursor is dosed into the system, it reacts with the available surface species on the surface leaving behind new surface species for the next precursor to react. By exposing the precursors in a cyclic manner to the growth substrate, a thin film is formed. Unlike other deposition methods, materials deposited by ALD principally allow atom by atom growth. Since the process is self-limiting in nature, ideally a monolayer is formed after one cycle of ALD. This produces extremely conformal and pinhole free coating that is highly uniform in thickness, even on high aspect ratio substrates.[29,30]

1.4.2 Why ALD for energy storage process?

Initially, the usage of ALD was only limited to the deposition of a protective layer on the electrodes for better cycling stability. Introduction of the concept of depositing active material by ALD method for energy storage is rather a recent trend. ALD is best known for its ability to deposit conformal and pinhole free nanolamination layer on extreme high surface area. Thus the conformal coating of active electrode materials on different high surface area conducting substrates and precise control over the thickness of the active layer makes ALD one of the most promising techniques for 3D nanostructures energy storage devices.

Therefore, considering the advantages and opportunities of ALD grown materials, this technique is undertaken in this work for the deposition of active materials.

However, the main disadvantage of ALD is their high cost and low deposition rate, which could be further compensated by deploying this technique to grow an optimally thick electrode material on a 3D architecture the with the extremely large surface-to-volume ratio. Nonetheless, there are some technological advancements are coming with low-cost and large size reactor for emerging applications. In this regard, atmospheric ALD[31,32] and roll-to-roll[33] deposition can surmount the low deposition rate obtained from conventional ALD systems.

1.5 Motivation

Essentially the next generation LIBs require high power density as well as high areal energy density to commercialize in any type of electronic portable devices[19,34] The miniaturization of this technology effectively demands more active material per areal footprint.[35] As a consequence, the nanostructured materials with very high surface area remain the main thrust for the high-performance LIBs.

Development in energy storage capacity can possibly be improved in two ways, (i) either by discovering new materials with very high capacity and good stability or (ii) by doing structural engineering with the best material available. To make a high energy density storage device, higher active mass loading is needed. That, in turn, leads to an increase in the resistive path and higher ionic-diffusion length. High resistance eventually disrupts power performance of the device. Such issues can be resolved by appropriate structural engineering of active materials. Fabrication of three-dimensional nanostructures with the high surface area would be an easy solution for high mass loading instead of two-dimensional staking of active material. Nano or microporous three-dimensional nanostructures can improve the performance of a device to a greater extent. Different nanostructures like nanorods, nanowires, nanosheets will provide very high surface area and maximum usage of active material whereas porous nature will give suitable contact with electrolyte.[22,24,25,36]

1.6 The aim of the thesis

The main objective of this work is to develop three-dimensional nanostructure materials with superior energy density and power density for electrochemical energy storage. Such electrodes

represent a unique way to improve the storage density and rate without the complex process of material development. Controlling the thickness of the active material in the nanometer dimension ensures the short diffusion length and full utilization of the active material. ALD technique will be used for an active material deposition because of its precise control and conformality at the nano level. Highly conducting template like CNT, graphene, metal nanostructures will be used to anchor the active material ensuring the effective electron transport. Optimization in thickness of the electrode materials will also be tried to achieve better performance. Also, enhancement in the conductivity of the electrochemically active oxide material with minimum changes in the pristine material is another objective of this work.

Currently, the production cost of CNTs and graphene are still higher and it is difficult for large scale synthesis. Hence, the next objective of this project would be the replacement of CNTs by the cheap and abundant metal nanostructures template layer. Copper (Cu) is one of highly available cheap material on the earth. It is being used in most of the integrated circuit and printed circuit board because of superior conductivity. Thus it is believed that active material coated Cu nanostructure would be a cost-effective solution for different energy storage devices.

1.7 Layout of the thesis

The complete thesis consists of total six chapters and two appendixes altogether. The present chapter (Chapter 1) is divided into two parts. The first part discusses about the importance of nanostructure in the field of energy storage. It also describes the advantages of ALD over other thin film deposition processes followed by the motivation and aim of the thesis. Last part of this thesis deals with the literature review of fundamental features of ALD processes and its application in the field of electrochemical storage. Chapter 3 dedicated to the detail experimental work to synthesize the material of our interest and different techniques in-situ and ex-situ used to characterize the materials. It further describes the electrochemical cell fabrication procedure and related characterization techniques to study the device performances. Chapter 3 represents the detail study of MoO_x coated CNT 3D nanostructures as anode material for lithium ion battery. How these electrodes produce much improved performance than their planar counterpart is discussed in depth. It also describes the lithiation-delithiation mechanism in commercial MoO_3 powder and compared with ALD grown

samples. Insulating nature of oxide materials is one of the major concerns for its low energy density and cycling stability. In this context, chapter 4 deals with how the electrical conductivity enhancement of oxide material helps to improve the electrochemical performance of a device. The conductivity is improved by incorporating nitrogen in the oxide layer. Detail study is done on electrical transportation properties of these N-incorporated oxide samples. In chapter 5, Cu-NW scaffold is used as template layer by replacing CNT. The main problem associated with Cu-NW is the unwanted surface oxidation occurs during oxide layer deposition. A thin layer of molybdenum nitride is applied in between of two materials to prevent the oxidation. Chapter 6 summarizes and concludes the complete work carried out in this thesis. It also discusses the possible future works that can be carried forward as a continuation of this work.

Apart from the main chapters discussed above, this thesis also includes two appendixes related to the work carried out. The aim of this work described in appendix-I, was to deposit self-standing 3D MoO_3 nanorods on a substrate for the application in LIB as anode material. Thin films of highly crystalline hexagonal MoO_3 nanorods are deposited by chemical bath deposition. However, the deposition only occurs on oxide substrates and cannot be deposited on any metal substrate to use in LIB. Appendix-II describes the low temperature fabrication of cobalt oxide coated CNT structures and their pseudocapacitance behaviour. It also showed the change in capacitance properties with the cobalt oxide thickness.

1.8 Literature review

This section of the thesis will majorly discuss the available literatures on the fundamental properties of ALD processes and its importance in the field of energy storage. Fundamental ALD reactions, its characteristic features and different kind of ALD techniques are discussed. This gives an idea to justify the choice of the ALD process used in this work for the deposition of different materials. Importance of ALD processes used in energy storage devices is discussed in the later part of this section, that provides an idea about the work done and opportunities lie in this direction of research.

1.8.1 Fundamentals of ALD

ALD is a sequential self-limiting vapor phase thin film deposition technique capable of depositing a wide range of materials. It has revealed great potential in semiconductor and

energy conversion technologies. As the current technologies push toward miniaturization and more dimensionally challenging configurations, ALD has exhibited potential benefits over alternative deposition techniques, such as CVD and other physical vapor deposition methods. Self-limiting nature gives an advantage of depositing conformal and uniform films on high aspect-ratio and challenging surfaces.[37,38]

ALD was initially introduced back in 1977 as atomic layer epitaxy (ALE) by Suntola et al., for the deposition of ZnS used in flat panel displays.[38] Further in advance, different metal and metal oxides were deposited non-epitaxially using this process and then a more general term ALD was adopted. It is worth noting, that initial development many ALD processes were followed from a variety of CVD procedures. The fundamental difference between CVD and ALD is that in case of CVD the reactants are dosed simultaneously into the reaction chamber whereas ALD precursors are dosed in an alternative sequence.[30,37]

1.8.1.1 ALD process

ALD is a sequential self-limiting deposition process. Consecutive exposure of the precursors in a cyclic manner on a suitable substrate forms a film. Each ALD cycle comprises four steps,

- Step-1: Reactant-1 dosing onto a substrate
- Step-2: Purging the by-products and excess chemicals from the reaction chamber
- Step-3: Reactant-2 dosing
- Step-4: Second purging

A typical ALD cycle can be described as shown in Figure 1.2. Here, precursor pulses are sequentially dosed and separated by a purging time given for evacuating by-products and unreacted molecules. Step-1 and 2 combinedly constitute the first half-cycle namely ‘A’, whereas step-3 and 4 constitute the second half-cycle namely ‘B’. The whole AB sequence is called as one ALD cycle. Hence, repeating the sequence ABABAB... gives desired film thickness. Ideally, each half cycle reactions are saturative and self-limiting, ensuring many beneficial qualities, such as layer by layer growth, excellent thickness control, large-area uniformity, repeatability and large-scale batch processing capacity. The main disadvantage of ALD is their slow deposition rate. This issue can be overlooked with the wider perspective of depositing high-quality materials and angstrom level thickness control. Table 1-1 shows the list of materials grown by ALD technique.[30,38]

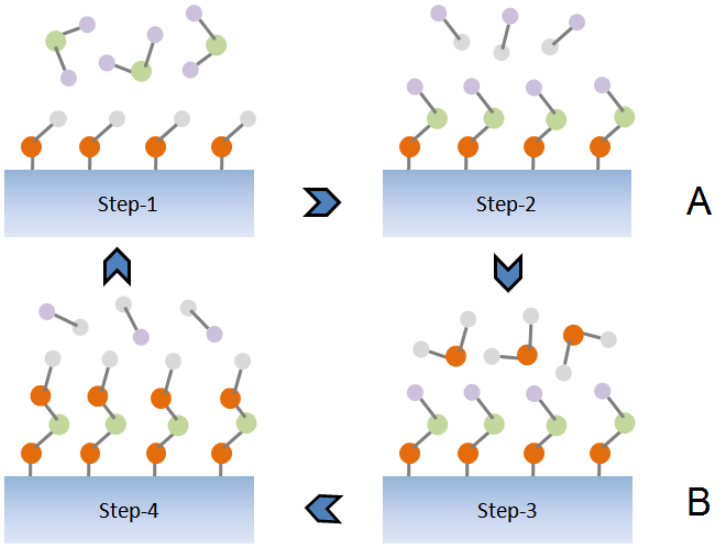


Figure 1.2 Schematic of a complete ALD cycle.

Table 1-1 List of materials grown by ALD[30]

Elemental	Oxides	Nitrides	Sulfides	Other compounds
C, Al, Si, Ti, Fe, Co, Ni, Cu, Zn, Ga, Ge, Mo, Ru, Rh, Pd, Ag, Ta, W, Os, Ir, Pt	Li, Be, B, Mg, Al, Si, P, Ca, Sc, Ti, V, Cr, Mn, Fe, Co, Ni, Cu, Zn, Ga, Ge, Mo, Sr, Y, Zr, Nb, Ru, Rh, Pd, In, Sn, Sb, Ba, La, Ce, Pr, Nd, Sm, Eu, Gd, Tb, Dy, Ho, Er, Tm, Yb, Lu, Hf, W, Ir, Pt, Pb, Bi	B, Al, Si, Ti, Cu, Ga, Zr, Nb, Mo, In, Hf, Ta, W	Ca, Ti, Mn, Cu, Zn, Sr, Y, Cd, Mo, In, Sn, Sb, Ba, La, W	Li, B, Mg, Al, Si, P, Ca, Ti, Cr, Mn, Co, Cu, Zn, Ga, Ge, As, Sr, Y, Cd, In, Sb, Te, Ba, La, Pr, Nd, Lu, Hf, Ta, W, Bi

1.8.1.2 Temperature window of ALD and self-limiting growth

Self-limiting growth and deposition temperature window are the two salient features of an ALD process. One ALD cycle fundamentally consists of two half cycle reactions. During each half cycle reactions, precursors in the vapor phase are chemisorbed on the surface, while the unreacted reactants and the gaseous by-products are purged out. A number of available surface sites on a surface are limited and there will be no reaction further when all the sites are reacted with the incoming reactants, thus no further reaction will be observed even with the presence of excess reactants. This mechanism is called a self-limiting or self-saturating condition which is a very unique feature of the ALD process. Therefore, ideally only one monolayer of the absorbed species will be formed after each ALD cycle.[39] Hence, the monolayer by monolayer growth helps to form conformal pinhole-free films on any kind of surface. However, in reality sometimes due to the limited number of surface sites and steric

hindrance caused by the adjacent atoms or molecules do not allow complete monolayer growth and growth rate often found to be a fraction of a monolayer thickness.[40] Figure 1.3a illustrates the self-limiting nature of an ALD process.

Since the chemisorption process is involved in ALD reactions, the absorption-desorption kinetics of the reactions will be highly temperature dependent. The term 'temperature window' of an ALD process portrays a temperature range in which self-limiting nature is observed for that particular reaction. Figure 1.3b shows the growth rate dependency with temperature often observed during different ALD grown compounds.

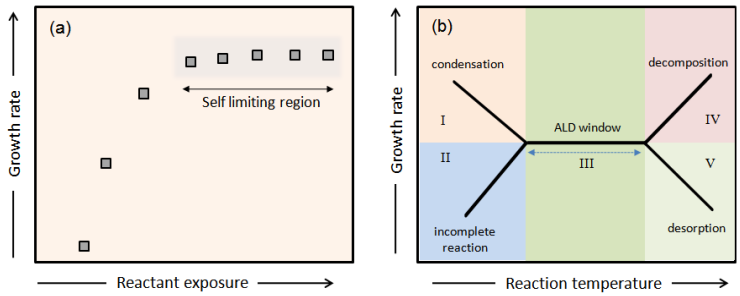


Figure 1.3 (a) Typical self-saturated growth characteristic as a function of precursor exposure during ALD and (b) Possible growth behavior as a function of temperature during ALD

At low temperatures, growth rates are observed either to decrease from higher values (as in Region I) or increase from lower values (as in region II) before reaching a constant. In region-I, the growth is governed by the condensation of reactants on the surface. The rate of deposition will decrease in this case with an increase in temperature because of the increase in the desorption rate. On the other hand, some processes can be thermodynamically limited at the lower temperatures due to insufficient thermal energy required to activate the reaction, fall in region II. In such cases, the rise in temperature will provide the adequate activation energy for the reaction to occur, thus the growth rate increases. Similarly, at higher deposition temperatures two types of growth rate observed. The growth rate may either increase (region IV) or decrease (region V) with an increase in temperature. The growth characteristics of region IV can be explained by the decomposition of precursors at high temperature leading to uncontrolled CVD like depositions. In another scenario, there is always a possibility of desorption of adsorbed molecules from the surface at a higher temperature leading to a decrease in the deposition rate that the reaction which is exactly the case in region-V. In between these regions, there is a temperature range (as shown in region-III) where the growth rate does not change much with the temperature, called 'ALD temperature window'. In this

region, the molecules have enough thermal energy to overcome the activation barrier but not enough energy to decompose or desorb, ensure completion of near ideal self-limiting surface reactions.[39–41]

It is worth mentioning that, although ALD window is one of the most desirable features of an ALD process which allows self-saturation and reproducible growth, this is not the absolute requirement for ALD growth.[42]

1.8.1.3 Nucleation and growth

Nucleation and growth are two fundamental characteristics of any film growth process. Each of them has a vital role in the growth rate and growth characteristics of deposited materials. After a nonlinear nucleation regime, in the beginning, the reaction enters into the linear growth process where the film thickness is increased linearly with the ALD cycles. The growth process of any gaseous phase deposition can be broadly divided into three categories- i) two-dimensional growth, ii) island growth and iii) combination of two-dimensional and island growth. In the case of two-dimensional growth also known as Frank van-der Merwe growth, the nucleation density is considerably high and almost forms a monolayer on the substrate. This kind of growth produces continuous thin films with low roughness. On the other hand, when the reactants do not react effectively with the initial surface, it results in non-uniform nucleation sites. The lack of uniformity in nucleation often leads to island type growth as illustrated by Volmer-Weber growth mechanism. As deposited thin films formed through this mechanism usually have high surface roughness and non-conformal. The third type of nucleation is called Stanski-Krastanov growth which is a combination of both the previous types of growth modes. Here, initially, films grow in a layer-by-layer manner up to a certain critical thickness and growth takes place following the island type manner from the succeeding layers. The critical layer thickness depends on the surface strain and chemical potential of the deposited material.[39,40,43]

Effective nucleation of any ALD reaction requires the surface species present on the substrate to react readily with the incoming precursors. ALD of oxide materials on the hydroxylated surface often found to produce effective nucleation. Hydroxyl groups are usually reactive with most of the metal-organic compounds that lead to almost a monolayer type growth. On the other hand, nucleation is found to be difficult for the metal oxides on the hydrogen passivated

Si substrates due to the significant mismatch in the surface energy between them. Depending on the nature of the surface functional groups, nucleation and growth characteristics of ALD reactions are often found significantly different and very much depends on the deposition chemistry.[44,45]

1.8.1.4 Different types of ALD

As discussed earlier, ALD is closely related to CVD processes based upon a simple ligand exchange binary reactions (A+B= product+ by-product). To make a reaction occur in the forward direction, the free energy (ΔG) has to be negative and certain thermal energy is required to overcome the activation barrier. That thermal energy is given in terms of temperature or high energy plasma during deposition. In a few cases, deposition is done at a higher temperature even though the reaction can occur even at room temperature. This is done to avoid condensation inside the reaction chamber at a low temperature. With the progression of time, there are mainly three types of ALD popularly used based upon the reaction conditions during deposition; (a) thermal ALD, (b) catalytic ALD and (c) plasma or radical-enhanced ALD (PE-ALD).

Thermal ALD is widely used and most sought after method for the deposition of a variety of materials. Here, the activation energy is given in terms of temperature applied that often ranges (100-500 ^{0}C) for spontaneous binary reactions. This process offers to deposit a wide range of material ranging from metals to metal oxides, sulfides, nitrides, phosphides and fluorides.[40]

In ***Catalytic ALD,*** the binary reactions are catalyzed through a Lewis acid-base reaction. Here the reaction temperature can be reduced extensively. Usage of catalyst in gaseous phase reaction is non-trivial. However, deposition on temperature sensitive substrates such as nanostructure devices, polymer or biologic samples needs relatively low deposition temperature. One of the most widely used materials in the semiconductor industry is SiO_2. The deposition of SiO_2 is done using $SiCl_4$ and H_2O as the precursors ($SiCl_4 + 2H_2O = SiO_2 + 4HCl$; ΔH =-32 kcal). Although the reaction is spontaneous at normal temperature, the surface reactions are significantly slow and only occur at a temperature of $\geq$325 ^{0}C with very long reactants exposure.

To achieve a reasonable growth rate, the reaction is catalyzed using a Lewis base (pyridine or NH_3). The presence of Lewis base enhances the reaction kinetics through the formation of intermolecular hydrogen bonding with the surface species. When these Lewis bases interact with Si-OH* surface species, the –O-H bond strength decreases and make oxygen stronger nucleophilic center. This, in turn, facilitates the interaction with incoming $SiCl_4$ molecules. Similarly, the interaction between H_2O and Lewis base makes oxygen stronger nucleophile and easily interacts with SiCl* surface species. These kinds of catalytic reactions also applied for other materials like TiO_2, ZrO_2 etc. One of the disadvantages in catalytic ALD is the formation of salt produced from the secondary reaction between Lewis base and reaction by-product (e.g. NH_3+ HCl= NH_4Cl). This kind of salts has finite vapor pressure and has to be removed properly else it will poison the surface.[46,47]

Plasma or radical-enhanced ALD is another kind of technique where the energy for the surface reaction to proceed is given by radicals or other energetic species in the plasma. In most of the nitride and metal film depositions, the energy produced from thermal energy is not sufficient to activate the reaction. Radicals or plasma helps to induce the energy required for reactions that are often found challenging through thermal route. Plasma-enhanced ALD of Ti was first demonstrated using hydrogen radicals produced from a hot tungsten filament.[48] Surface reaction of Ti ALD can be simply represented as-[49]

Step-1: $Ti^* + TiCl_4 \rightarrow TiTiCl_4^*$
Step-2: $TiCl_4^* + 4H^{\cdot} \rightarrow Ti^* + 4HCl$

1.8.1.5 ALD precursors

Precursor chemistry plays a major role in every ALD process. In principle, the precursor should have high volatility and thermal stability at the deposition temperature. During deposition, the precursors have to be either chemisorbed on the substrate or should readily react with the surface species to achieve the self-saturation condition in a short duration ensuring a reasonable growth rate. Type of precursors used in ALD processes can be divided into two broad categories which are halide based and organic based precursors.

Halide precursors, especially metal chlorides are the most widely used precursors for deposition of oxides, nitrides, and sulfides starting from the very early phase of ALD to till date. Metal chlorides are in general solid at room temperature, thus sometime pre-heating is

required to obtain a reasonable vapor pressure during deposition. These precursors are easier to synthesize and they offer simple ligand exchange chemistry often resulting in perfect self-saturative growth. However, the deposition temperature of material using a halide precursor is found to be very high because of the strong ionic bond between metal and halide atoms. Another drawback of metal-halide precursors is the corrosive by-products obtained after each reaction.[50]

Table 1-2 Comparison of deposition temperatures using halide and organic based precursors

Material	Organic precursors	Deposition Temp	Ref	Halide precursors	Deposition Temp	Ref
SiO_2	Tetramethyl orthosilicate (TMOS)	150°C	[51]	$SiCl_4$	323-523°C	[52]
	$H_2N(CH_2)_3Si(OEt)_3$	100-200°C	[53]			
HfO_2	$HfCl_2[NSiMe_3]_2$	200°C	[54]	$HfCl_4$	200-400°C	[55]
	$(MeCp)_2HfMe_2$	350-450°C	[56]			
ZrO_2	$(MeCp)_2ZrMe_2$	300-400°C	[57]	$ZrCl_4$	280-400°C	[58]
	Cp_2ZrCl_2	275-300°C	[57]			
	$Zr[OCH(CH)_3]_4$	80-200°C	[59]			
Al_2O_3	$Al(CH_3)_3$ (TMA)	150-300°C	[60]	$AlCl_3$	300-800°C	[61]
	$(CH_3)_2AlOCH(CH_3)_2$	150°C	[62]			
ZnO	$Zn(C_2H_5)_2$ (DEZn)	100-180°C	[63]	$ZnCl_2$	480-500°C	[64]
	$Zn(CH_3)_2$ (DMZn)	80-150°C				
	$Zn(CH_3COO)_2$	230-250°C				
TiO_2	$Ti(OCH(CH_3)_2)_4$	80-200°C	[59]	$TiCl_4$	150-525°C	[65]

Metal-organic based precursors are comparatively lately introduced but have gained rapid attention. They offer several notable advantages over metal-halides. The deposition temperature of a material can be brought down to a large extent using metal-organic precursor than its halide analog. A comparative study of halide and organic based precursors is shown in Table 1-1. Metal alkyls are highly regarded precursors for ALD reactions because of their high volatility and spontaneous reaction with the surface species. In many cases, they almost behave ideally in depositing oxide and sulfide materials. Along with alkyls, metal alkoxides and β-diketonates are also widely used organic precursors for ALD. Although metal-organic

precursors provide lots of advantages, the availabilities of this kind of compounds are often limited to their unstable nature.[50]

1.8.2 Utilizing ALD technique for electrochemical storage

Electrode materials play a pivotal role in determining the overall performance in electrochemical storage devices. Initially, ALD has been mostly used for surface modification, where interface related issues are observed, but later on, it has shown great potential in constructing unique nanostructure active materials with added advantages over other processing techniques. On the basis of unique benefits offered by ALD, the following discussion is presented in three major aspects: ALD for surface modification; ALD for active material deposition and ALD for novel nanostructure fabrication.

1.8.2.1 ALD for surface modification on electrodes

Performance of an electrochemical storage device is greatly influenced by the crystal structure and interfacial chemistry. The improvement in electrochemical performances through surface modification using exclusive properties of ALD is emphasized as following.

1.8.2.1.1 Surface modification for LIB cathodes

It is known that the undesired side reactions occurred at the interface between the cathode material and electrolyte sometimes cause slow degradation of electrodes during cycling.[66] A slight surface modification or thin protective layer improves the electrochemical performance of cathode materials. Coating of a thin layer of different oxide, phosphate or fluoride on electrode materials are observed to be often beneficial in term of improvement in cycling lifetime and rate performance.[67–69] These materials act as a physical protective layer as well as sometime fluorine scavenger layer, with better ionic-conductivity and clean surface chemistry.[66] ALD offers high-level conformal surface coverage with sub-nanometer scale thickness control on the electrode in comparison with other traditional deposition processes.

Surface modification with a few nanometers of ALD Al_2O_3 coating directly on different electrode materials without disturbing the inter-particle connection network is the most common example reported in the literature.[70,71] This kind of protective layer acts as an artificial solid electrolyte interface with improved interfacial reactions during electrochemical processes. However, when the Al_2O_3 layer was first coated onto active materials and then

applied to an electrode, the electrochemical performance was observed to be not so encouraging. This is because of the fact that the insulating nature of Al_2O_3 retards electrical conductivity inside the electrode. A study by Scott et al. showed the improvement in electrochemical activity of $LiCoO_2$ powder electrode when 1-2 nm of Al_2O_3 is uniformly deposited by ALD.[71] Al_2O_3 coated electrodes maintained almost 100% capacity retention even after 200 cycles, whereas the capacity of uncoated electrode dropped rapidly after few cycles. The rate performances also improved to a better extend in case of Al_2O_3 coated electrodes. Similar kind of improvements are also noticed in other cathode materials, where similar kind of improvements can be found with Al_2O_3 coating by ALD.[70,72,73,74,75]

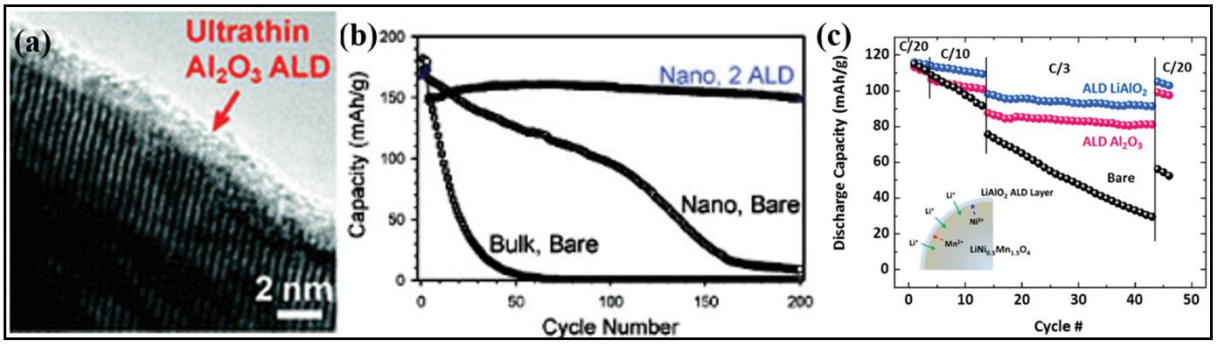


Figure 1.4 Surface modification of LIB electrodes by ALD. a) SEM image of Al_2O_3 coated $LiCoO_2$, b) cycling performance of bulk $LiCoO_2$, uncoated nano-$LiCoO_2$, and Al_2O_3 coated nano-$LiCoO_2$.[71] c) cycling performances of $LiNi_{0.5}Mn_{1.5}O_4$/graphite cells with different coatings: uncoated, $LiAlO_2$ and Al_2O_3 coated.[76]

The major problem associated with Al_2O_3 coating is its insulating nature which retards Li^+ ion conductivity through the layer. To eliminate this problem, researchers have replaced Al_2O_3 with other materials such as $LiAlO_2$, TiO_2, ZnO and $FePO_4$.[77–81] Park et al. showed that the electrodes with $LiAlO_2$ coating performed better than Al_2O_3 coated samples.[76] This is due to the better Li^+-ion conductivity of $LiAlO_2$ than that of Al_2O_3 layer. In another study by Sun's group showed that 2 ALD cycle coating of Al_2O_3 gives the best performance than thicker coating, while ZrO_2 coated samples showed best rate capabilities.[82] Another interesting study by Liang et al. reported that ALD CeO_2 coated $LiMn_2O_4$ electrode showed much improved electrochemical activities in comparison to Al_2O_3 and ZrO_2 modified surface. It was believed that the Li^+ conductivity in ALD CeO_2 layer is better than other two layers.[83] In a nutshell, it is clearly depicted from the ongoing studies that the ALD coated protective layer (majorly oxides) reveal better cycling stability and device performance.

1.8.2.1.2 Surface modification for LIB anodes

Mostly used anode material in commercial LIB is graphite because of its suitable Li insertion and extraction mechanism. However, the major concern with graphite anode is the safety issue due to the formation of solid electrolyte interface on the surface.[84] Researchers have tried to protect the graphite surface and reduce the formation of a solid interface by modifying the interface. Modification of surface through a thin layer of ALD Al_2O_3 on graphite showed significant improvement in electrochemical performance as well as safety at a higher temperature.[85] Electrode showed approximately 98% of its initial capacity retained after with just 5 cycles of ALD even after 200 cycles of charge-discharge at 50 ^{0}C while the unprotected electrode showed only 25% capacity retention. In another work by Wang et al. have used ALD TiO_2 protection layer on natural graphite and observed improved stability at 55 ^{0}C.[86]

Apart from graphite, alloyed materials, like Si and Sn-based compound took a lot of attention recently for their very high capacities and relatively lower onset potential.[87,88] However, these materials undergo severe volume expansion and contraction during lithium insertion and extraction, resulting in irreversible structural deformation of particles. In this scenario, He et al. showed that a thin layer of ALD Al_2O_3 coating on patterned Si electrode not only solves the issue of the unstable surface electrolyte but also it provides mechanical strength during charge-discharge cycling.[89] In addition to that surface modified electrodes also showed superior columbic efficiency in comparison to uncoated analog. Further study on ALD Al_2O_3 surface modified Si thin film and Si nanowires moreover showed similar kind of improvement in performance.[90,91]

Metal oxides have shown a lot of promises as next-generation electrode materials, because of their high capacities and safety factor. Volume expansion and pulverization issue stand for many of them also. Surface modification helped them improving from those issues. Lipson et al. reported that a thin layer of ALD Al_2O_3 on MnO anode successfully prevent the formation of solid electrolyte interface and maintain the same capacity over 100 charge-discharge cycles. Similar kind of phenomena observed for other metal oxides like Fe_2O_3, MoO_3 and $Li_4Ti_5O_{12}$ etc.[92–94]

Above clearly indicate that the surface modification of LIB electrodes could efficiently restrain the unwanted side reactions, provide mechanical strength prevent electrolyte decomposition at the interface.

1.8.2.1.3 ALD surface modification for supercapacitor electrodes

Surface modification of supercapacitor electrodes by ALD technique has been extended like LIB electrodes. Carbonaceous materials are widely used for supercapacitor electrodes, because of their high electrical conductivity, huge surface area and better electrochemical stability.[95] However, these materials offer very less capacitance. Extension of working voltage window can be an option to increase the capacity. Nonetheless, most of them are not stable at the high-voltage region. To solve this issue, a thin layer of ALD Al_2O_3 has been applied by Hong et al. The ALD coated electrodes exhibited good stability until 3 V with an organic electrolyte.[95] The ALD layer helps in protecting surface functional groups and prevents the decomposition of electrolyte on the electrode surface. Another option to improve the energy density of carbonaceous materials is to coat a thin layer of different materials (such as V_2O_5, Fe_2O_3, Bi_2O_3)[96,97] which contribute in additional capacitance without sacrificing much of the power density. For example, ALD V_2O_5 coating on CNT electrodes reported by Boukhalfa et al. has demonstrated high energy density as well as good cycling ability.[96] Similar kind of results obtained from other materials also such as Fe_2O_3, NiO, Co_3O_4, RuO_2 etc.[98]

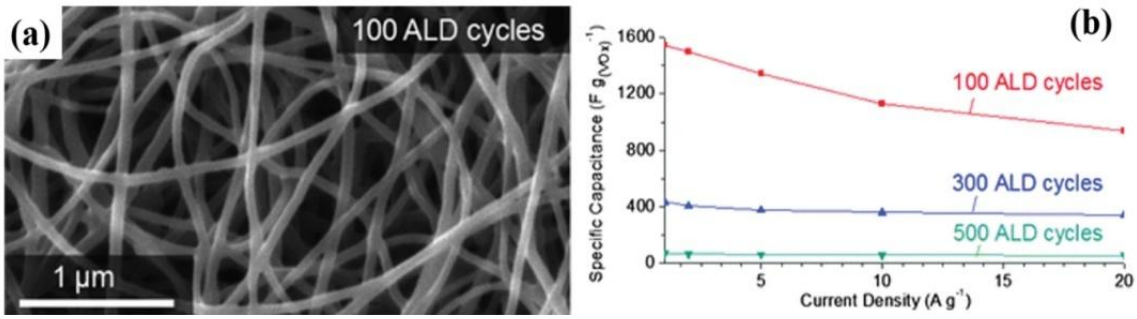


Figure 1.5 Surface modification of V_2O_5 supercapacitor electrodes. a) SEM image of 100 cycles of ALD V_2O_5 coated CNTs and b) Specific capacitance of CNTs samples coated with 100, 300, and 500 cycles of ALD V_2O_5.[96]

1.8.2.2 ALD for active material deposition

We have previously discussed that the ALD coated materials help in protecting the electrodes from unwanted interfacial side reactions. On the other hand, deposition of self-standing active materials directly on the substrate by ALD technique has guided to the development of

various electrode structures. This process helps to study fundamental electrochemical activities of different materials solely without adding different fillers required during electrode fabrication. This section will discuss the active materials being used in different energy storage devices developed by the ALD process.

A wide range of materials has been developed by ALD on 3D complex substrate, used as both cathode and anode for electrochemical energy storage. Few examples are oxides, such as TiO_2, ZnO, Co_3O_4, MnO_2, V_2O_5, RuO_2, SnO_2, $FePO_4$, $LixMn_2O_4$, $LiCoO_2$;[99–106] sulfides such as Cu_2S, MoS_2, GaS_x;[107–109] and nitrides such as MoN_x,[110] WN_x[110] etc. Planar 2D electrodes showed excellent electrochemical stability and reversibility. Conformal nature of ALD makes it a very promising technique to nanolaminate high surface area 3D hierarchical substrates with active materials.

1.8.2.2.1 ALD of active materials on 3D nanostructures

ALD method provides an extra advantage during active material coating on nanostructures substrates, where both the thickness and porosity can be well controlled for optimized Li+ diffusion length in the active materials. Ye et al. studied the electrochemical performance of 2 nm ALD TiO_2 coated nanoporous gold electrode.[111] A power density of 13 KW Kg^{-1} and high energy density of 130 Wh Kg^{-1} is observed with 225 nm in pore size. Large pore size is needed for the electrolyte to infiltrate throughout the electrode, ensuring efficient electrochemical interaction and a thin layer of active material certainly benefits with the short Li^+ diffusion length. An ALD SnO_2 coated Ni nanofoam was successfully fabricated by Haag et al. electrode has shown a capacity of 546 mAh g^{-1} with good cycling stability.[112] High area 3D substrates with high conductivity provide efficient conducting network and ultrathin active layer withstands the volume change during charge-discharge cycling for a long time. Other reported ALD coated 3D hierarchical metal substrates are Ni/TiO_2, Al/TiO_2, Ni/V_2O_5.[112]

1.8.2.2.2 ALD of active materials on carbonaceous materials

Carbonaceous materials are the typical class of materials used in electrochemical energy storage because of their high electrical conductivity, high surface area and lightweight, which are crucial for high rate capability. On the other hand, metal oxides and nitrides offer very

high capacity, beneficial for higher energy density. For that reason, a hybrid structure with the combination of carbonaceous materials and metal oxides or nitrides shows a lot of promises in the field of electrochemical storage. Considering the conformal deposition and thickness control ability of ALD processes, decoration of active materials on carbonaceous substrates by ALD is the matter of interest for high performing energy storage devices.

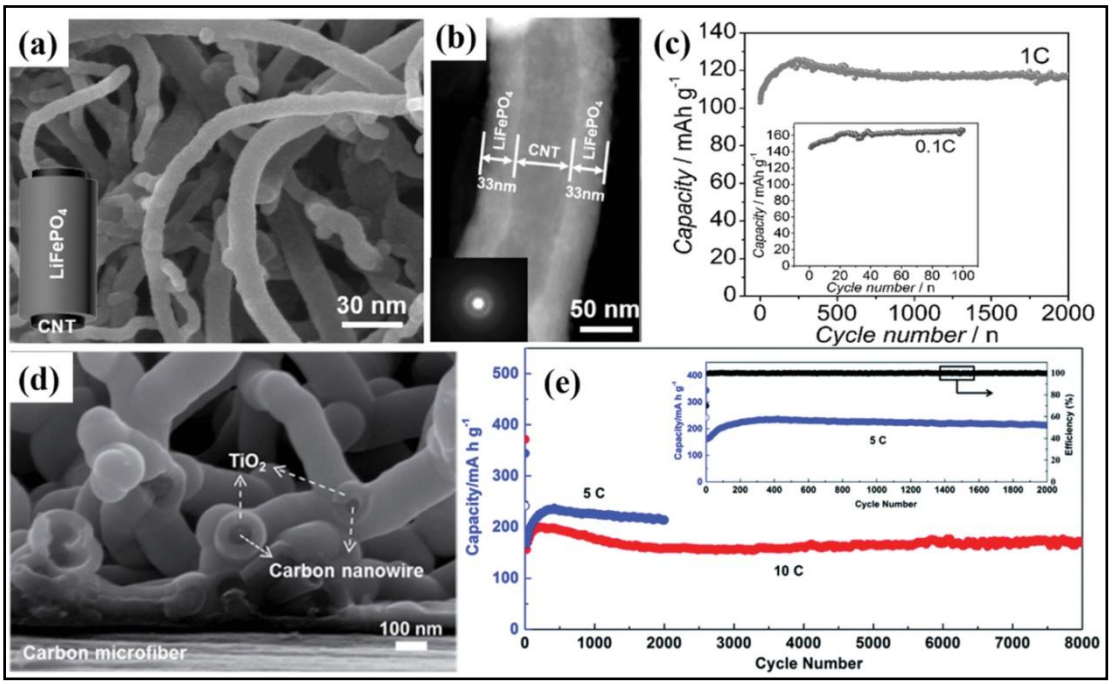


Figure 1.6 a) SEM and b) TEM images of ALD $LiFePO_4$ coated CNT, c) Cycling performance of the CNT@$LiFePO_4$ cathode for lithium storage.[113] d) SEM image and e) cycling behavior of ALD TiO_2 coated carbon cloth/carbon nanowire as a LIB anode.[114]

ALD deposited cathode material of $LiFePO_4$ coating on conducting CNTs network, developed by Liu et al. has shown a high discharge capacity of ~160 mAh g−1 at 0.1C rate (Figure 1.6c).[113] It also demonstrated excellent rate performance (71 mAh g−1 at 60C) and capacity retention (120 mAh g−1 after 2000 cycles at 170 mA g^{-1}). The outstanding electrochemical performance of $LiFePO_4$/CNTs electrode was derived from the distinctive permutation of carbon nanostructure and ALD technique.

In another study, Wang et al. fabricated ALD TiO_2 coated carbon nanowire arrays on flexible carbon cloth and used as LIB anode.[114] Mass loading on 3D nanostructure arrangement found to be ~300 times higher than that of the planar counterpart. C/TiO_2 arrangement demonstrated discharge capacity of 309 mAh g^{-1} at 0.2C rate and 100 mAh g^{-1} at 20C rate. Excellent cycling stability up to 8000 cycles is also accomplished at 10C rate. Several other groups have

tried similar structure arrangement with different active materials, for example, CNT/V_2O_5, CNT/Ru, graphene/ZnO, and graphene/NiO.[115–118]

1.8.3 MoO_3 as anode material in LIB

Transition metal oxides are one of the major domains of the research in LIBs because of their high theoretical capacity and excellent reversibility with Li/Li^+ system. However, the major problem associated with these oxide materials is the poor electronic and ionic conductivity and high volume expansion-contraction during charge-discharge cycles.[20,119] Among several other transition metal oxides, MoO_3, a highly abandoned and low-cost material, is one of the widely studied oxides as both cathode and anode for LIBs. As an anode material, MoO_3 attracted more interest because of various redox reaction obtained from different valency state of Mo and a high reversible theoretical capacity of ~1110 $mAhg^{-1}$ based on the full conversion reaction against Li^+ as given below[120–122] —

$MoO_3 + 6Li^+ + 6e^- \rightarrow 3Li_2O + Mo$

Despite of having a high initial capacity of MoO_3 anodes, most of the report showed the capacity fading with cycling even in nanostructured electrodes.[123,124] Increase in conductivity can address this issue towards achieving a stable capacity. CNTs and graphene are the most used material along with the active material because of their high conductivity, lightweight, and high chemical and mechanical stability.[125,126] Therefore, in most of the cases, the conductivity was increased by forming hybrid hetero-nanostructure just by adding CNTs or graphene into the composite or by growing MoO_3 onto the same. Carbon coating on MoO_3 nanobelt helped to obtain a high capacity that approximately reached its theoretical value as shown by Hassan et al.[120] In another study, pre-heat treatment of binder rich MoO_3 composite facilitating the coating of a uniform conductive layer resulting in a high capacity as well as good cycling stability.[127]

Different deposition techniques are tried for coating active material on CNTs or graphene sheets. Solvothermal, spray pyrolysis, hydrothermal, electrodeposition and other solution deposition processes are widely used but often suffer from the difficulties of uniformity and thickness control.[28,128–130] High volume changes during charge-discharge processes lead to detachment of the active layer synthesized using the above-mentioned deposition techniques from the template layer and as a result, low capacity retention and poor cycle lifetime are obtained. ALD reveals the potential to overcome those limitations to a great extent with its

excellent uniformity and thickness control over the deposited active material. Few reports illustrate the usage of ALD to develop high areal capacity cathodes and anodes on nanostructures like metal nanorod, nanowire, CNTs and graphene.[27,109,131–134]

Till date, the MoO_x ALD is not a widely studied process. $Mo(CO)_6$ and $Mo(NtBu)_2(NMe_2)_2$ are the only two precursors so far used as molybdenum source to deposit amorphous MoO_x by ALD.[135–137] However, the molybdenum hexacarbonyl precursor offers a lower deposition temperature (155—172 ^{0}C) than the later one (200—300 ^{0}C).

Amorphous materials are an overlooked group indeed in electrochemical storage applications. In few recent works of literature, the amorphous materials showed to have better electrochemical properties. High cycling lifetime and self-increasing capacity are the most common facts regarding these amorphous materials.[134,138] In one of the reports by Li et al. observed that a thin amorphous layer coating of the same material on crystalline $LiFePO_4$ nanoparticles showed an ultra high rate performance (60 mAh/g at 400 C).[139] It is proposed that the different energy sites at the surface of the amorphous layer helped to enhance the charge transfer kinetics of the Li^+ ions during charge and discharge. Hence, the amorphous molybdenum oxide coated CNT hybrid nanostructure is chosen to be the active material for the present work.

1.8.4 Electrochemical activity of molybdenum oxynitrides

Nitrogen-doped oxides or sometimes called as oxynitrides of transition metals gained considerable attention in materials research due to tunability in optoelectronic properties.[140–142] Nitrogen, with respect to oxygen, with higher charge and less electronegativity that introduces more covalency in the lattice results alteration of electronic properties by partial anion substitution. The valance band of the binary transition metal compounds is majorly contributed by the anion (2*p*-orbitals for oxides and nitrides) while the *d*-orbitals of the metal dominates the lower part of the conduction band.

Formation energy of nitrogen defects in transition metal nitride is lower than the oxygen vacancy in the oxides resulting in higher electronic conductivity in the metal-nitrides. Also the oxygen 2*p* bonds that contribute to the valance band in oxides are energetically low lying than the nitrogen that gives rise to the higher bandgap in oxides than the nitrides. As a

consequence, a combination of these anions results in a good degree of freedom in controlling the conductivity and the optical properties of the transition metal compounds. Thus a bandgap tuned dielectrics like TiO_2, CeO_2 and even perovskite oxynitrides etc. are used for efficient photoelectrochemical water splitting or as a photocatalyst. Again, some transition metal oxynitrides like VO_xN_y, NbO_xN_y etc. shows improved conductivity and hence better electrochemical performance in Li-ion batteries in comparison to their respective binary compounds.

Nature of nitrogen incorporation metal oxides varies substantially. Often a stable intermediate oxynitride phase (e.g. $NbO_{1.3}N_{0.7}$, $Sm_2Mo_2O_{3.83}N_{3.17}$ etc.) or solid solution, like $Ce_{1-y}Ce_yO_{2-3x/2-y/2}N_x$ ($x \leq 0.09$, $y \leq 0.06$), are well reported in the literature. In layered binary oxides, like MoO_3, WO_3, substitution of terminal oxygen by nitrogen in the lattice is most common where the change of lattice parameter along b-axis ({0k0} planes) significantly higher than other axes. Thus be it substitution or a solid solution, controlled incorporation of nitrogen in binary metal oxides are often challenging.

One of the most common methods of nitrogen incorporation in metal oxides is by annealing under either NH_3 or N_2/H_2 ambient at high temperature. However, this process involves high temperature and often results the partial reduction of the host material.[143,144] Urea, amide, azide etc. can be alternative nitrogen sources other than NH_3. Several techniques like pulsed laser deposition (PLD), magnetron sputtering, high-pressure synthesis and different low-temperature chemical routes etc. are also used for the synthesis of oxynitrides but often they suffer from uniformity and proper control issues.

In this scenario, ALD can be explored as an alternative route for dopant incorporation in a controlled manner. ALD is a well-established deposition technique for depositing thin films with an added advantage of their surface limited reaction chemistry that provides conformal and atomic layer thickness control over the deposition. For *doping*, nanolaminate structures with varied periodicity and thickness of binary compounds are grown that allows inter-diffusion with or without post-deposition treatments. Because of its excellent control over dopant concentration in the host materials, electrical properties can also be regulated precisely.

Due to their better electronic conductivity than pure oxide, LIB technology also finds some extent of research activities with such oxynitrides.[145,146,147] However, the thrust put in exploring the potential of these oxynitrides in energy storage are not up to the mark. In the present circumstances, new anode material with high capacity and better electrochemical stability is always desirable towards improved energy storage. Transition metal oxides, an extraordinary option in terms of capacity and stable reversible reaction against Li, are extensively studied material in LIBs. However, the vital problem associated with these oxide materials is its intrinsically poor electrical conductivity and high volume change during charge-discharge.[20,119] Several researchers have attempted different methods to overcome this issue. One of the efficient techniques is to blend oxide materials with a different kind of conducting carbonaceous materials like graphene, CNT etc. However, using the carbon brings a safety issue in the picture.[125,134,148,149] Therefore, the other alternative way is to dope the metal oxides with nitrogen to improve the electrical conductivity it which results in enhanced and more stable electrochemical performance of these materials in LIBs.

As mentioned earlier, MoO_3, a highly abandoned and low-cost material, is also one of the most widely studied oxides both as cathode and anode for LIB. As an anode material, it attracted considerable interest because of its high theoretical capacity of approximately ~1110 mAh/g based on full conversion reaction.[121] However as mentioned before, its insulating nature and high volume expansion during lithiation (approximately 100% volume increase) become the bottleneck for stable cycling performance.[124] Though prelithiated MoO_3 showed improved conductivity but the capacity fading issue remains as a big challenge so far. Nitrogen incorporated MoO_3 and molybdenum oxynitride, $[Mo(O,N)_3]$ showed much improved and stable electrochemical performance compared to pristine MoO_3. Kuhn et al. synthesized $Mo(O,N)_3$ structure which has higher electronic and ionic conductivity than pristine MoO_3.[150] In another case, ammonolyzed MoO_3 was used as superior cathode material by Wang et al.[151] Partially nitrided MoO_3 was also reported as a better anode material for LIB by Zhou et al.[143] and Ji et al.[144] Several other metal oxynitrides (*e.g.*- VO_xN_y, NbO_xN_y, WO_xN_y etc.) also showed better electrochemical performance in LIBs than their respective pure oxides.

1.9 References

(1) Buzea, C.; Pacheco, I. I.; Robbie, K. Nanomaterials and Nanoparticles: Sources and Toxicity. *Biointerphases* **2007**, *2* (4), MR17-MR71.

(2) Andrievskii, R. A.; Khachoyan, A. V. Role of Size-Dependent Effects and Interfaces in Physicochemical Properties of Consolidated Nanomaterials. *Russ. J. Gen. Chem.* **2010**, *80* (3), 555–566.

(3) Eustis, S.; El-Sayed, M. A. Why Gold Nanoparticles Are More Precious than Pretty Gold: Noble Metal Surface Plasmon Resonance and Its Enhancement of the Radiative and Nonradiative Properties of Nanocrystals of Different Shapes. *Chem. Soc. Rev.* **2006**, *35* (3), 209–217.

(4) Moskovits, M. Surface-Enhanced Spectroscopy. *Rev. Mod. Phys.* **1985**, *57* (3), 783–826.

(5) Singh, A. K.; Srivastava, O. N.; Singh, K. Shape and Size-Dependent Magnetic Properties of Fe_3O_4 Nanoparticles Synthesized Using Piperidine. *Nanoscale Res. Lett.* **2017**, *12*, 0–6.

(6) Guisbiers, G. Size-Dependent Materials Properties toward a Universal Equation. *Nanoscale Res. Lett.* **2010**, *5* (7), 1132–1136.

(7) Drozdz, E. The Influence of the Method of Addition of Al2O3to 3YSZ Material on Its Thermal and Electrical Properties. *J. Therm. Anal. Calorim.* **2014**, *118* (2), 1345–1353.

(8) *Nanotechnology for Microelectronics and Photonics*, 2nd ed.; Elsevier, 2017.

(9) Chen, X.; Li, C.; Grätzel, M.; Kostecki, R.; Mao, S. S. Nanomaterials for Renewable Energy Production and Storage. *Chem. Soc. Rev.* **2012**, *41* (23), 7909–7937.

(10) Chen, B. Next-Generation Energy Conversion and Storage. *IEEE Nanotechnol. Mag.* **2012**, *6* (3), 4–7.

(11) Kim, H. C.; Fthenakis, V. Life Cycle Energy and Climate Change Implications of Nanotechnologies: A Critical Review. *J. Ind. Ecol.* **2013**, *17* (4), 528–541.

(12) Mao, S. S.; Chen, X. Selected Nanotechnologies for Renewable Energy Applications. *Int. J. Energy Res.* **2007**, *31* (2), 619–636.

(13) Kamat, P. V.; Schatz, G. C. Nanotechnology for next Generation Solar Cells. *J. Phys. Chem. C* **2009**, *113* (35), 15473–15475.

(14) Liu, Y.; Zhou, G.; Liu, K.; Cui, Y. Design of Complex Nanomaterials for Energy Storage: Past Success and Future Opportunity. *Acc. Chem. Res.* **2017**, *50* (12), 2895–

2905.

(15) Sheng, T.; Xu, Y. F.; Jiang, Y. X.; Huang, L.; Tian, N.; Zhou, Z. Y.; Broadwell, I.; Sun, S. G. Structure Design and Performance Tuning of Nanomaterials for Electrochemical Energy Conversion and Storage. *Acc. Chem. Res.* **2016**, *49* (11), 2569–2577.

(16) Daniel, C.; Mohanty, D.; Li, J.; Wood, D. L. Cathode Materials Review. *AIP Conf. Proc.* **2014**, *1597* (1), 26–43.

(17) Kiani, M. a.; Mousavi, M. F.; Rahmanifar, M. S. Synthesis of Nano- and Micro-Particles of LiMn2O4: Electrochemical Investigation and Assessment as a Cathode in Li Battery. *Int. J. Electrochem. Sci.* **2011**, *6* (7), 2581–2595.

(18) Scrosati, B.; Garche, J. Lithium Batteries: Status, Prospects and Future. *J. Power Sources* **2010**, *195* (9), 2419–2430.

(19) Tarascon, J. M.; Armand, M. Issues and Challenges Facing Rechargeable Lithium Batteries. *Nature* **2001**, *414* (6861), 359–367.

(20) Poizot, P.; Laruelle, S.; Grugeon, S.; Dupont, L.; Tarascon, J.-M. Nano-Sized Transition-Metal Oxides as Negative-Electrode Materials for Lithium-Ion Batteries. *Nature* **2000**, *407* (5), 496–499.

(21) González, A.; Goikolea, E.; Barrena, J. A.; Mysyk, R. Review on Supercapacitors: Technologies and Materials. *Renew. Sustain. Energy Rev.* **2016**, *58* (1), 1189–1206.

(22) Wu, Z.-S.; Parvez, K.; Feng, X.; Müllen, K. Graphene-Based in-Plane Micro-Supercapacitors with High Power and Energy Densities. *Nat. Commun.* **2013**, *4* (2487), 1–8.

(23) Portet, C.; Taberna, P. L.; Simon, P.; Flahaut, E.; Laberty-Robert, C. High Power Density Electrodes for Carbon Supercapacitor Applications. *Electrochim. Acta* **2005**, *50* (20), 4174–4181.

(24) Wang, G.; Zhang, L.; Zhang, J. A Review of Electrode Materials for Electrochemical Supercapacitors. *Chem. Soc. Rev.* **2012**, *41* (2), 797–828.

(25) Zhi, M.; Xiang, C.; Li, J.; Li, M.; Wu, N. Nanostructured Carbon-Metal Oxide Composite Electrodes for Supercapacitors: Review. *Nanoscale* **2012**, *5* (1), 72–88.

(26) Shi, F.; Li, L.; Wang, X.; Gu, C.; Tu, J. Metal Oxide/hydroxide-Based Materials for Supercapacitors. *RSC Adv.* **2014**, *4* (79), 41910–41921.

(27) Boukhalfa, S.; Evanoff, K.; Yushin, G. Atomic Layer Deposition of Vanadium Oxide

on Carbon Nanotubes for High-Power Supercapacitor Electrodes. *Energy Environ. Sci.* **2012**, *5* (5), 6872–6879.

(28) Wang, G.; Shen, X.; Yao, J.; Wexler, D.; Ahn, J. H. Hydrothermal Synthesis of Carbon Nanotube/cobalt Oxide Core-Shell One-Dimensional Nanocomposite and Application as an Anode Material for Lithium-Ion Batteries. *Electrochem. commun.* **2009**, *11* (3), 546–549.

(29) George, S. M. Atomic Layer Deposition: An Overview. *Chem. Rev.* **2010**, *110* (1), 111–131.

(30) Johnson, R. W.; Hultqvist, A.; Bent, S. F. A Brief Review of Atomic Layer Deposition: From Fundamentals to Applications. *Mater. Today* **2014**, *17* (5), 236–246.

(31) Muñoz-Rojas, D.; Macmanus-Driscoll, J. Spatial Atmospheric Atomic Layer Deposition: A New Laboratory and Industrial Tool for Low-Cost Photovoltaics. *Mater. Horizons* **2014**, *1* (3), 314–320.

(32) van den Bruele, F. J.; Smets, M.; Illiberi, A.; Creyghton, Y.; Buskens, P.; Roozeboom, F.; Poodt, P. Atmospheric Pressure Plasma Enhanced Spatial ALD of Silver. *J. Vac. Sci. Technol. A Vacuum, Surfaces, Film.* **2015**, *33* (1), 01A131.

(33) George, S.; Fitzpatrick, P.; Gibbs, Z. Atomic Layer Deposition for Continuous Roll-to-Roll Processing. *54th Annu. Tech. Conf. Proceedings, Soc. Vac. Coaters* **2011**, No. 2, 76.

(34) Wang, Y.; Cao, G. Developments in Nanostructured Cathode Materials for High-Performance Lithium-Ion Batteries. *Adv. Mater.* **2008**, *20* (12), 2251–2269.

(35) Nathan, M.; Golodnitsky, D.; Yufit, V.; Strauss, E.; Ripenbein, T.; Shechtman, I.; Menkin, S.; Peled, E. Three-Dimensional Thin-Film Li-Ion Microbatteries for Autonomous MEMS. *J. Microelectromechanical Syst.* **2005**, *14* (5), 879–885.

(36) Jiang, H.; Ma, J.; Li, C. Mesoporous Carbon Incorporated Metal Oxide Nanomaterials as Supercapacitor Electrodes. *Adv. Mater.* **2012**, *24* (30), 4197–4202.

(37) George, S. M. Atomic Layer Deposition: An Overview. *Chem. Rev.* **2010**, *110* (1), 111–131.

(38) Puurunen, R. L. A Short History of Atomic Layer Deposition: Tuomo Suntola's Atomic Layer Epitaxy. *Chem. Vap. Depos.* **2014**, *20* (10–12), 1–13.

(39) Puurunen, R. L. Surface Chemistry of Atomic Layer Deposition: A Case Study for the Trimethylaluminum/water Process. *J. Appl. Phys.* **2005**, *97* (12), 121301 1-52.

(40) George, S. M. Atomic Layer Deposition: An Overview. *Chem. Rev.* **2010**, *110* (1), 111–131.

(41) Carcia, P. F.; McLean, R. S.; Reilly, M. H.; Groner, M. D.; George, S. M. Ca Test of Al2O3gas Diffusion Barriers Grown by Atomic Layer Deposition on Polymers. *Appl. Phys. Lett.* **2006**, *89* (3), 23–26.

(42) Jones, A. C.; Aspinall, H. C.; Chalker, P. R. *Chemical Vapour Deposition of Metal Oxides for Microelectronics Applications*; 2009; Vol. Chapter 8.

(43) Argile, C.; Rhead, G. E. Adsorbed Layer and Thin Film Growth Modes Monitored by Auger Electron Spectroscopy. *Surf. Sci. Rep.* **1989**, *10* (6–7), 277–356.

(44) Farmer, D. B.; Gordon, R. G. ALD of High-κ Dielectrics on Suspended Functionalized SWNTs. *Electrochem. Solid-State Lett.* **2005**, *8* (4), G89-91.

(45) Xuan, Y.; Wu, Y. Q.; Shen, T.; Qi, M.; Capano, M. A.; Cooper, J. A.; Ye, P. D. Atomic-Layer-Deposited Nanostructures for Graphene-Based Nanoelectronics. *Appl. Phys. Lett.* **2008**, *92* (1), 013101 1-3.

(46) Klaus, J. W.; George, S. M. Atomic Layer Deposition of SiO_2 at Room Temperature Using NH3-Catalyzed Sequential Surface Reactions. *Surf. Sci.* **2000**, *447* (1), 81–90.

(47) Du, Y.; Du, X.; George, S. M. SiO_2 Film Growth at Low Temperatures by Catalyzed Atomic Layer Deposition in a Viscous Flow Reactor. *Thin Solid Films* **2005**, *491* (1–2), 43–53.

(48) Rossnagel, S. M.; Sherman, A.; Turner, F. Plasma-Enhanced Atomic Layer Deposition of Ta and Ti for Interconnect Diffusion Barriers. *J. Vac. Sci. Technol. B Microelectron. Nanom. Struct.* **2000**, *18* (4), 2016.

(49) Kim, H.; Cabral, C.; Lavoie, C.; Rossnagel, S. M. Diffusion Barrier Properties of Transition Metal Thin Films Grown by Plasma-Enhanced Atomic-Layer Deposition. *J. Vac. Sci. Technol. B Microelectron. Nanom. Struct.* **2002**, *20* (4), 1321–1326.

(50) Leskelä, M.; Ritala, M. Atomic Layer Deposition (ALD): From Precursors to Thin Film Structures. *Thin Solid Films* **2002**, *409* (1), 138–146.

(51) Ma, Z.; Brown, S.; Howe, J. Y.; Overbury, S. H.; Dai, S. Surface Modification of Au/TiO2catalysts by SiO_2 via Atomic Layer Deposition. *J. Phys. Chem. C* **2008**, *112* (25), 9448–9457.

(52) Ott, A. W.; McCarley, K. C.; Klaus, J. W.; Way, J. D.; George, S. M. Atomic Layer Controlled Deposition of SiO2 and Al_2O_3 films Using Binary Reaction Sequence

Chemistry. *Appl. Surf. Sci.* **1994**, *82* (83), 460–467.

(53) Bachmann, J.; Zierold, R.; Chong, Y. T.; Hauert, R.; Sturm, C.; Schmidt-Grund, R.; Rheinländer, B.; Grundmann, M.; Gösele, U.; Nielsch, K. A Practical, Self-Catalytic, Atomic Layer Deposition of Silicon Dioxide. *Angew. Chemie - Int. Ed.* **2008**, *47* (33), 6177–6179.

(54) Kang, S.-W.; Rhee, S.-W.; George, S. M. Infrared Spectroscopic Study of Atomic Layer Deposition Mechanism for Hafnium Silicate Thin Films Using $HfCl_2[N(SiMe_3)_2]_2$ and H_2O. *J. Vac. Sci. Technol. A Vacuum, Surfaces, Film.* **2004**, *22* (6), 2392–2397.

(55) Kukli, K.; Ritala, M.; Sajavaara, T.; Keinonen, J.; Leskelä, M. Comparison of Hafnium Oxide Films Grown by Atomic Layer Deposition from Iodide and Chloride Precursors. *Thin Solid Films* **2002**, *416* (1–2), 72–79.

(56) Dezelah IV, C. L.; Niinistö, J.; Kukli, K.; Munnik, F.; Lu, J.; Ritala, M.; Leskelä, M.; Niinistö, L. The Atomic Layer Deposition of HfO_2 and ZrO_2 using Advanced Metallocene Precursors and H_2O as the Oxygen Source. *Chem. Vap. Depos.* **2008**, *14* (11–12), 358–365.

(57) Putkonen, M.; Niinistö, L. Zirconia Thin Films by Atomic Layer Epitaxy. A Comparative Study on the Use of Novel Precursors with Ozone. *J. Mater. Chem.* **2001**, *11* (12), 3141–3147.

(58) Cassir, M.; Goubin, F.; Bernay, C.; Vernoux, P.; Lincot, D. Synthesis of ZrO_2 thin Films by Atomic Layer Deposition: Growth Kinetics, Structural and Electrical Properties. *Appl. Surf. Sci.* **2002**, *193* (4), 120–128.

(59) Shin, H.; Jeong, D. K.; Lee, J.; Sung, M. M.; Kim, J. Formation of TiO_2 and ZrO_2 Nanotubes Using Atomic Layer Deposition with Ultraprecise Control of the Wall Thickness. *Adv. Mater.* **2004**, *16* (14), 1197–1200.

(60) Elliott, S. D.; Scarel, G.; Wiemer, C.; Fanciulli, M.; Pavia, G. Ozone-Based Atomic Layer Deposition of Alumina from TMA: Growth, Morphology, and Reaction Mechanism. *Chem. Mater.* **2006**, *18* (16), 3764–3773.

(61) Dueñas, S.; Castán, H.; García, H.; De Castro, A.; Bailón, L.; Kukli, K.; Aidla, A.; Aarik, J.; Mändar, H.; Uustare, T.; et al. Influence of Single and Double Deposition Temperatures on the Interface Quality of Atomic Layer Deposited Al_2O_3 dielectric Thin Films on Silicon. *J. Appl. Phys.* **2006**, *99* (5), 54902.

(62) An, K. S.; Cho, W.; Sung, K.; Lee, S. S.; Kim, Y. Preparation of Al_2O_3 Thin Films by Atomic Layer Deposition Using Dimethylaluminum Isopropoxide and Water and Their Reaction Mechanisms. *Bull. Korean Chem. Soc.* **2003**, *24* (11), 1659–1663.

(63) Guziewicz, E.; Godlewski, M.; Krajewski, T.; Wachnicki; Szczepanik, A.; Kopalko, K.; Wójcik-Godowska, A.; Przeździecka, E.; Paszkowicz, W.; Łusakowska, E.; et al. ZnO Grown by Atomic Layer Deposition: A Material for Transparent Electronics and Organic Heterojunctions. *J. Appl. Phys.* **2009**, *105* (12), 122413 1-5.

(64) Wójcik, A.; Kopalko, K.; Godlewski, M.; Łusakowska, E.; Guziewicz, E.; Minikayev, R.; Paszkowicz, W.; Świątek, K.; Klepka, M.; Jakieła, R.; et al. Thin Films of ZnO and ZnMnO by Atomic Layer Epitaxy. *Phys. Status Solidi* **2005**, *2* (3), 1125–1130.

(65) Cameron, M. A.; Gartland, I. P.; Smith, J. A.; Diaz, S. F.; George, S. M. Atomic Layer Deposition of SiO_2 and TiO_2 in Alumina Tubular Membranes: Pore Reduction and Effect of Surface Species on Gas Transport. *Langmuir* **2000**, *16* (19), 7435–7444.

(66) Chen, Z.; Qin, Y.; Amine, K.; Sun, Y. K. Role of Surface Coating on Cathode Materials for Lithium-Ion Batteries. *J. Mater. Chem.* **2010**, *20* (36), 7606–7612.

(67) Zhao, T.; Li, L.; Chen, R.; Wu, H.; Zhang, X.; Chen, S.; Xie, M.; Wu, F.; Lu, J.; Amine, K. Design of Surface Protective Layer of LiF/FeF_3 Nanoparticles in Li-Rich Cathode for High-Capacity Li-Ion Batteries. *Nano Energy* **2015**, *15* (1), 164–176.

(68) Wang, B.; Al Abdulla, W.; Wang, D.; Zhao, X. S. A Three-Dimensional Porous LiFePO4 Cathode Material Modified with a Nitrogen-Doped Graphene Aerogel for High-Power Lithium Ion Batteries. *Energy Environ. Sci.* **2015**, *8* (3), 869–875.

(69) Jung, Y. S.; Cavanagh, A. S.; Dillon, A. C.; Groner, M. D.; George, S. M.; Lee, S. H. Enhanced Stability of $LiCoO_2$ Cathodes in Lithium-Ion Batteries Using Surface Modification by Atomic Layer Deposition. *J. Korean Ceram. Soc.* **2010**, *157* (1), A75–A81.

(70) Kim, J. W.; Kim, D. H.; Oh, D. Y.; Lee, H.; Kim, J. H.; Lee, J. H.; Jung, Y. S. Surface Chemistry of $LiNi_{0.5}Mn_{1.5}O_4$ particles Coated by Al2O3using Atomic Layer Deposition for Lithium-Ion Batteries. *J. Power Sources* **2015**, *274*, 1254–1262.

(71) Scott, I. D.; Jung, Y. S.; Cavanagh, A. S.; Yan, Y.; Dillon, A. C.; George, S. M.; Lee, S. H. Ultrathin Coatings on Nano-$LiCoO_2$ for Li-Ion Vehicular Applications. *Nano Lett.* **2011**, *11* (2), 414–418.

(72) Fang, X.; Ge, M.; Rong, J.; Che, Y.; Aroonyadet, N.; Wang, X.; Liu, Y.; Zhang, A.;

Zhou, C. Ultrathin Surface Modification by Atomic Layer Deposition on High Voltage Cathode $LiNi_{0.5}Mn_{1.5}O_4$ for Lithium Ion Batteries. *Energy Technol.* **2014**, *2* (2), 159–165.

(73) Kim, J. W.; Travis, J. J.; Hu, E.; Nam, K. W.; Kim, S. C.; Kang, C. S.; Woo, J. H.; Yang, X. Q.; George, S. M.; Oh, K. H.; et al. Unexpected High Power Performance of Atomic Layer Deposition Coated $Li[Ni_{1/3}Mn_{1/3}Co_{1/3}]O_2$ cathodes. *J. Power Sources* **2014**, *254*, 190–197.

(74) Zhang, X.; Belharouak, I.; Li, L.; Lei, Y.; Elam, J. W.; Nie, A.; Chen, X.; Yassar, R. S.; Axelbaum, R. L. Structural and Electrochemical Study of Al_2O_3 and TiO_2 Coated Li1.2Ni0.13Mn0.54Co 0.13O2 Cathode Material Using ALD. *Adv. Energy Mater.* **2013**, *3* (10), 1299–1307.

(75) Guan, D.; Wang, Y. Ultrathin Surface Coatings to Enhance Cycling Stability of LiMn2O4cathode in Lithium-Ion Batteries. *Ionics (Kiel).* **2013**, *19* (1), 1–8.

(76) Park, J. S.; Meng, X.; Elam, J. W.; Hao, S.; Wolverton, C.; Kim, C.; Cabana, J. Ultrathin Lithium-Ion Conducting Coatings for Increased Interfacial Stability in High Voltage Lithium-Ion Batteries. *Chem. Mater.* **2014**, *26* (10), 3128–3134.

(77) Guan, D.; Jeevarajan, J. A.; Wang, Y. Enhanced Cycleability of $LiMn_2O_4$ Cathodes by Atomic Layer Deposition of Nanosized-Thin Al_2O_3 Coatings. *Nanoscale* **2011**, *3* (4), 1465–1469.

(78) Cheng, H. M.; Wang, F. M.; Chu, J. P.; Santhanam, R.; Rick, J.; Lo, S. C. Enhanced Cycleabity in Lithium Ion Batteries: Resulting from Atomic Layer Depostion of Al 2O 3 or TiO 2 on LiCoO 2 Electrodes. *J. Phys. Chem. C* **2012**, *116* (14), 7629–7637.

(79) Zhao, J.; Wang, Y. Atomic Layer Deposition of Epitaxial ZrO2 coating on LiMn2O4nanoparticles for High-Rate Lithium Ion Batteries at Elevated Temperature. *Nano Energy* **2013**, *2* (5), 882–889.

(80) Kong, J. Z.; Ren, C.; Tai, G. A.; Zhang, X.; Li, A. D.; Wu, D.; Li, H.; Zhou, F. Ultrathin ZnO Coating for Improved Electrochemical Performance of $LiNi_{0.5}Co_{0.2}Mn_{0.3}O_2$ cathode Material. *J. Power Sources* **2014**, *266* (29), 433–439.

(81) Xiao, B.; Liu, J.; Sun, Q.; Wang, B.; Banis, M. N.; Zhao, D.; Wang, Z.; Li, R.; Cui, X.; Sham, T. K.; et al. Unravelling the Role of Electrochemically Active $FePO_4$ Coating by Atomic Layer Deposition for Increased High-Voltage Stability of $LiNi_{0.5}Mn_{1.5}O_4$ Cathode Material. *Adv. Sci.* **2015**, *2* (5), 4–9.

(82) Li, X.; Liu, J.; Meng, X.; Tang, Y.; Banis, M. N.; Yang, J.; Hu, Y.; Li, R.; Cai, M.; Sun, X. Significant Impact on Cathode Performance of Lithium-Ion Batteries by Precisely Controlled Metal Oxide Nanocoatings via Atomic Layer Deposition. *J. Power Sources* **2014**, *247*, 57–69.

(83) Patel, R. L.; Xie, H.; Park, J.; Asl, H. Y.; Choudhury, A.; Liang, X. Significant Capacity and Cycle-Life Improvement of Lithium-Ion Batteries through Ultrathin Conductive Film Stabilized Cathode Particles. *Adv. Mater. Interfaces* **2015**, *2* (8), 1–9.

(84) Parellada, J. A.; Dunn, M. M.; Wayland, A.; Cousins, J.; Shaw de Paredes, E. Patient Tracking and Follow-up after Percutaneous Breast Biopsy. *Appl. Radiol.* **1997**, *26* (2), 7–10.

(85) Jung, Y. S.; Cavanagh, A. S.; Riley, L. A.; Kang, S. H.; Dillon, A. C.; Groner, M. D.; George, S. M.; Lee, S. H. Ultrathin Direct Atomic Layer Deposition on Composite Electrodes for Highly Durable and Safe Li-Ion Batteries. *Adv. Mater.* **2010**, *22* (19), 2172–2176.

(86) Wang, H. Y.; Wang, F. M. Electrochemical Investigation of an Artificial Solid Electrolyte Interface for Improving the Cycle-Ability of Lithium Ion Batteries Using an Atomic Layer Deposition on a Graphite Electrode. *J. Power Sources* **2013**, *233*, 1–5.

(87) Wang, B.; Luo, B.; Li, X.; Zhi, L. The Dimensionality of Sn Anodes in Li-Ion Batteries. *Mater. Today* **2012**, *15* (12), 544–552.

(88) Huang, J. Y.; Zhong, L.; Wang, C. M.; Sullivan, J. P.; Xu, W.; Zhang, L. Q.; Mao, S. X.; Hudak, N. S.; Liu, X. H.; Subramanian, A.; et al. In Situ Observation of the Electrochemical Lithiation of a Single SnO_2 nanowire Electrode. *Science (80-.).* **2010**, *330* (6010), 1515–1520.

(89) He, Y.; Yu, X.; Wang, Y.; Li, H.; Huang, X. Alumina-Coated Patterned Amorphous Silicon as the Anode for a Lithium-Ion Battery with High Coulombic Efficiency. *Adv. Mater.* **2011**, *23* (42), 4938–4941.

(90) Memarzadeh Lotfabad, E.; Kalisvaart, P.; Cui, K.; Kohandehghan, A.; Kupsta, M.; Olsen, B.; Mitlin, D. ALD TiO_2 coated Silicon Nanowires for Lithium Ion Battery Anodes with Enhanced Cycling Stability and Coulombic Efficiency. *Phys. Chem. Chem. Phys.* **2013**, *15* (32), 13646–13657.

(91) Li, J.; Xiao, X.; Cheng, Y. T.; Verbrugge, M. W. Atomic Layered Coating Enabling Ultrafast Surface Kinetics at Silicon Electrodes in Lithium Ion Batteries. *J. Phys.*

Chem. Lett. **2013**, *4* (20), 3387–3391.

(92) Kang, E.; Jung, Y. S.; Cavanagh, A. S.; Kim, G. H.; George, S. M.; Dillon, A. C.; Kim, J. K.; Lee, J. Fe_3O_4 nanoparticles Confined in Mesocellular Carbon Foam for High Performance Anode Materials for Lithium-Ion Batteries. *Adv. Funct. Mater.* **2011**, *21* (13), 2430–2438.

(93) Riley, L. a.; Cavanagh, A. S.; George, S. M.; Jung, Y. S.; Yan, Y.; Lee, S. H.; Dillon, A. C. Conformal Surface Coatings to Enable High Volume Expansion Li-Ion Anode Materials. *ChemPhysChem* **2010**, *11* (10), 2124–2130.

(94) Liu, J.; Li, X.; Cai, M.; Li, R.; Sun, X. Ultrathin Atomic Layer Deposited ZrO2coating to Enhance the Electrochemical Performance of Li4Ti5O12as an Anode Material. *Electrochim. Acta* **2013**, *93*, 195–201.

(95) Bose, S.; Kuila, T.; Mishra, A. K.; Rajasekar, R.; Kim, N. H.; Lee, J. H. Carbon-Based Nanostructured Materials and Their Composites as Supercapacitor Electrodes. *J. Mater. Chem.* **2012**, *22* (3), 767–784.

(96) Boukhalfa, S.; Evanoff, K.; Yushin, G. Atomic Layer Deposition of Vanadium Oxide on Carbon Nanotubes for High-Power Supercapacitor Electrodes. *Energy Environ. Sci.* **2012**, *5* (5), 6872–6879.

(97) Guan, C.; Liu, J.; Wang, Y.; Mao, L.; Fan, Z.; Shen, Z.; Zhang, H.; Wang, J. Iron Oxide-Decorated Carbon for Supercapacitor Anodes with Ultrahigh Energy Density and Outstanding Cycling Stability. *ACS Nano* **2015**, *9* (5), 5198–5207.

(98) Zhi, M.; Xiang, C.; Li, J.; Li, M.; Wu, N. Nanostructured Carbon-Metal Oxide Composite Electrodes for Supercapacitors: A Review. *Nanoscale* **2013**, *5* (1), 72–88.

(99) Xie, M.; Sun, X.; Zhou, C.; Cavanagh, A. S.; Sun, H.; Hu, T.; Wang, G.; Lian, J.; George, S. M. Amorphous Ultrathin TiO_2 Atomic Layer Deposition Films on Carbon Nanotubes as Anodes for Lithium Ion Batteries. *J. Electrochem. Soc.* **2015**, *162* (6), A974–A981.

(100) Aravindan, V.; Jinesh, K. B.; Prabhakar, R. R.; Kale, V. S.; Madhavi, S. Atomic Layer Deposited (ALD) SnO_2 anodes with Exceptional Cycleability for Li-Ion Batteries. *Nano Energy* **2013**, *2* (5), 720–725.

(101) Gregorczyk, K. E.; Kozen, A. C.; Chen, X.; Schroeder, M. A.; Noked, M.; Cao, A.; Hu, L.; Rubloff, G. W. Fabrication of 3D Core À Shell Lithium-Ion Battery Electrodes through a RuO 2 Atomic Layer Deposition Process. *ACS Nano* **2015**, *9* (1), 464–473.

(102) Donders, M. E.; Knoops, H. C. M.; Kessels, W. M. M.; Notten, P. H. L. Co 3O 4 as Anode Material for Thin Film Micro-Batteries Prepared by Remote Plasma Atomic Layer Deposition. *J. Power Sources* **2012**, *203* (1), 72–77.

(103) Rauda, I. E.; Augustyn, V.; Saldarriaga-Lopez, L. C.; Chen, X.; Schelhas, L. T.; Rubloff, G. W.; Dunn, B.; Tolbert, S. H. Nanostructured Pseudocapacitors Based on Atomic Layer Deposition of V_2O_5 onto Conductive Nanocrystal-Based Mesoporous ITO Scaffolds. *Adv. Funct. Mater.* **2014**, *24* (42), 6717–6728.

(104) Donders, M. E.; Arnoldbik, W. M.; Knoops, H. C. M.; Kessels, W. M. M.; Notten, P. H. L. Atomic Layer Deposition of $LiCoO_2$ Thin-Film Electrodes for All-Solid-State Li-Ion Micro-Batteries. *J. Electrochem. Soc.* **2013**, *160* (5), A3066–A3071.

(105) Miikkulainen, V.; Ruud, A.; Østreng, E.; Nilsen, O.; Laitinen, M.; Sajavaara, T.; Fjellvaìšg, H. Atomic Layer Deposition of Spinel Lithium Manganese Oxide by Film-Body-Controlled Lithium Incorporation for Thin-Film Lithium-Ion Batteries. *J. Phys. Chem. C* **2014**, *118* (2), 1258–1268.

(106) Gandrud, K. B.; Pettersen, A.; Nilsen, O.; Fjellvåg, H. High-Performing Iron Phosphate for Enhanced Lithium Ion Solid State Batteries as Grown by Atomic Layer Deposition. *J. Mater. Chem. A* **2013**, *1* (32), 9054–9059.

(107) Dasgupta, N. P.; Meng, X.; Elam, J. W.; Martinson, A. B. F. Atomic Layer Deposition of Metal Sulfide Materials. *Acc. Chem. Res.* **2015**, *48* (2), 341–348.

(108) Meng, X.; Riha, S. C.; Libera, J. A.; Wu, Q.; Wang, H. H.; Martinson, A. B. F.; Elam, J. W. Tunable Core-Shell Single-Walled Carbon Nanotube-Cu_2S Networked Nanocomposites as High-Performance Cathodes for Lithium-Ion Batteries. *J. Power Sources* **2015**, *280* (1), 621–629.

(109) Meng, X.; He, K.; Su, D.; Zhang, X.; Sun, C.; Ren, Y.; Wang, H. H.; Weng, W.; Trahey, L.; Canlas, C. P.; et al. Gallium Sulfide-Single-Walled Carbon Nanotube Composites: High-Performance Anodes for Lithium-Ion Batteries. *Adv. Funct. Mater.* **2014**, *24* (34), 5435–5442.

(110) Nandi, D. K.; Sen, U. K.; Choudhury, D.; Mitra, S.; Sarkar, S. K. Atomic Layer Deposited Molybdenum Nitride Thin Film: A Promising Anode Material for Li Ion Batteries. *ACS Appl Mater Inter* **2014**, *6* (9), 6606–6615.

(111) Ye, J.; Baumgaertel, A. C.; Wang, Y. M.; Biener, J.; Biener, M. M. Structural Optimization of 3D Porous Electrodes for High-Rate Performance Lithium Ion

Batteries. *ACS Nano* **2015**, *9* (2), 2194–2202.

(112) Haag, J. M.; Pattanaik, G.; Durstock, M. F. Nanostructured 3D Electrode Architectures for High-Rate Li-Ion Batteries. *Adv. Mater.* **2013**, *25* (23), 3238–3243.

(113) Liu, J.; Banis, M. N.; Sun, Q.; Lushington, A.; Li, R.; Sham, T. K.; Sun, X. Rational Design of Atomic-Layer-Deposited $LiFePO_4$as a High-Performance Cathode for Lithium-Ion Batteries. *Adv. Mater.* **2014**, *26* (37), 6472–6477.

(114) Wang, X. H.; Guan, C.; Sun, L. M.; Rahmat Agung Susantyoko, H. J. F.; Zhang, Q. Highly Stable and Flexible Li-Ion Battery Anodes Based on TiO_2 Coated 3D Carbon Nanostructures. *J. Mater. Chem. A* **2015**, *3* (22), 15394–15398.

(115) Chen, X.; Pomerantseva, E.; Banerjee, P.; Gregorczyk, K.; Ghodssi, R.; Rubloff, G. Ozone-Based Atomic Layer Deposition of Crystalline V_2O_5 Films for High Performance Electrochemical Energy Storage. *Chem. Mater.* **2012**, *24* (7), 1255–1261.

(116) Warren, R.; Sammoura, F.; Tounsi, F.; Sanghadasa, M.; Lin, L. Highly Active Ruthenium Oxide Coating via ALD and Electrochemical Activation in Supercapacitor Applications. *J. Mater. Chem. A* **2015**, *3* (30), 15568–15575.

(117) Yu, M.; Wang, A.; Wang, Y.; Li, C.; Shi, G. An Alumina Stabilized ZnO-Graphene Anode for Lithium Ion Batteries via Atomic Layer Deposition. *Nanoscale* **2014**, *6* (19), 11419–11424.

(118) Chen, C.; Chen, C.; Huang, P.; Duan, F.; Zhao, S.; Li, P.; Fan, J.; Song, W.; Qin, Y. NiO/nanoporous Graphene Composites with Excellent Supercapacitive Performance Produced by Atomic Layer Deposition. *Nanotechnology* **2014**, *25* (50), 504001.

(119) He, P.; Yu, H.; Li, D.; Zhou, H. Layered Lithium Transition Metal Oxide Cathodes towards High Energy Lithium-Ion Batteries. *J. Mater. Chem.* **2012**, *22* (9), 3680–3695.

(120) Hassan, M. F.; Guo, Z. P.; Chen, Z.; Liu, H. K. Carbon-Coated MoO3 Nanobelts as Anode Materials for Lithium-Ion Batteries. *J. Power Sources* **2010**, *195* (8), 2372–2376.

(121) Yu, X.; Wang, L.; Liu, J.; Sun, X. Porous MoO_3 Film as a High-Performance Anode Material for Lithium-Ion Batteries. *ChemElectroChem* **2014**, *1* (9), 1476–1479.

(122) Martinez-Garcia, A.; Thapa, A. K.; Dharmadasa, R.; Nguyen, T. Q.; Jasinski, J.; Druffel, T. L.; Sunkara, M. K. High Rate and Durable, Binder Free Anode Based on Silicon Loaded MoO_3 Nanoplatelets. *Sci. Rep.* **2015**, *5* (April), 10530 1-5.

(123) Leroux, F.; Nazar, L. F. Uptake of Lithium by Layered Molybdenum Oxide and Its Tin

Exchanged Derivatives: High Volumetric Capacity Materials. *Solid State Ionics* **2000**, *133* (1), 37–50.

(124) Jung, Y. S.; Lee, S.; Ahn, D.; Dillon, A. C.; Lee, S. H. Electrochemical Reactivity of Ball-Milled MoO_{3-Y} as Anode Materials for Lithium-Ion Batteries. *J. Power Sources* **2009**, *188* (1), 286–291.

(125) Ni, J.; Wang, G.; Yang, J.; Gao, D.; Chen, J.; Gao, L.; Li, Y. Carbon Nanotube-Wired and Oxygen-Deficient MoO_3 Nanobelts with Enhanced Lithium-Storage Capability. *J. Power Sources* **2014**, *247* (1), 90–94.

(126) Liu, C.-L.; Wang, Y.; Zhang, C.; Li, X.-S.; Dong, W.-S. In Situ Synthesis of α-MoO_3/graphene Composites as Anode Materials for Lithium Ion Battery. *Mater. Chem. Phys.* **2014**, *143* (3), 1111–1118.

(127) Riley, L. a.; Lee, S. H.; Gedvilias, L.; Dillon, A. C. Optimization of MoO_3 Nanoparticles as Negative-Electrode Material in High-Energy Lithium Ion Batteries. *J. Power Sources* **2010**, *195* (2), 588–592.

(128) Ren, J.; Yang, J.; Abouimrane, A.; Wang, D.; Amine, K. SnO_2 Nanocrystals Deposited on Multiwalled Carbon Nanotubes with Superior Stability as Anode Material for Li-Ion Batteries. *J. Power Sources* **2011**, *196* (20), 8701–8705.

(129) Li, X.; Wang, C. Engineering Nanostructured Anodes via Electrostatic Spray Deposition for High Performance Lithium Ion Battery Application. *J. Mater. Chem. A* **2013**, *1* (2), 162–182.

(130) Kim, I.-H.; Kim, J.-H.; Cho, B.-W.; Lee, Y.-H.; Kim, K.-B. Synthesis and Electrochemical Characterization of Vanadium Oxide on Carbon Nanotube Film Substrate for Pseudocapacitor Applications. *J. Electrochem. Soc.* **2006**, *153* (6), A989–A996.

(131) Knez, M.; Kadri, A.; Wege, C.; Gösele, U.; Jeske, H.; Nielsch, K. Atomic Layer Deposition on Biological Macromolecules: Metal Oxide Coating of Tobacco Mosaic Virus and Ferritin. *Nano Lett.* **2006**, *6* (6), 1172–1177.

(132) Wang, W.; Tian, M.; Abdulagatov, A.; George, S. M.; Lee, Y. C.; Yang, R. Three-Dimensional Ni/TiO_2 Nanowire Network for High Areal Capacity Lithium Ion Microbattery Applications. *Nano Lett.* **2012**, *12* (2), 655–660.

(133) Gregorczyk, K. E.; Kozen, A. C.; Chen, X.; Schroeder, M. A.; Noked, M.; Cao, A.; Hu, L.; Rubloff, G. W. Fabrication of 3D Core À Shell Lithium-Ion Battery Electrodes

through a RuO 2 Atomic Layer Deposition Process. *ACS Nano* **2015**, *9* (1), 464–473.

(134) Li, X.; Meng, X.; Liu, J.; Geng, D.; Zhang, Y.; Cai, M.; Verbrugge, M. W. Tin Oxide with Controlled Morphology and Crystallinity by Atomic Layer Deposition onto Graphene Nanosheets for Enhanced Lithium Storage. *Adv. Funct. Mater.* **2012**, *22* (8), 1647–1654.

(135) Diskus, M.; Nilsen, O.; Fjellvåg, H. Growth of Thin Films of Molybdenum Oxide by Atomic Layer Deposition. *J. Mater. Chem.* **2011**, *21* (3), 705–710.

(136) Bertuch, A.; Sundaram, G.; Saly, M.; Moser, D.; Kanjolia, R. Atomic Layer Deposition of Molybdenum Oxide Using Bis(tert-Butylimido)bis(dimethylamido) Molybdenum. *J. Vac. Sci. Technol. A Vacuum, Surfaces, Film.* **2014**, *32* (1), 01A119 1-6.

(137) Nandi, D. K.; Sarkar, S. K. Atomic Layer Deposition of Molybdenum Oxide for Solar Cell Application. *Appl. Mech. Mater.* **2014**, *492*, 375–379.

(138) Gandrud, K. B.; Pettersen, A.; Nilsen, O.; Fjellvåg, H. High-Performing Iron Phosphate for Enhanced Lithium Ion Solid State Batteries as Grown by Atomic Layer Deposition. *J. Mater. Chem. A* **2013**, *1* (32), 9054–9059.

(139) Kang, B.; Ceder, G. Battery Materials for Ultrafast Charging and Discharging. *Nature* **2009**, *458* (7235), 190–193.

(140) Xie, R. J.; Hintzen, H. T. Optical Properties of (Oxy)nitride Materials: A Review. *J. Am. Ceram. Soc.* **2013**, *96* (3), 665–687.

(141) Bugaris, D. E.; Ibers, J. a. Synthesis and Properties of Functional Oxynitrides – from Photocatalysts to CMR Materials. *Dalton Trans.* **2010**, *39* (26), 5942–5948.

(142) Lerch, M.; Janek, J.; Becker, K. D.; Berendts, S.; Boysen, H.; Bredow, T.; Dronskowski, R.; Ebbinghaus, S. G.; Kilo, M.; Lumey, M. W.; et al. Oxide Nitrides: From Oxides to Solids with Mobile Nitrogen Ions. *Prog. Solid State Chem.* **2009**, *37* (2–3), 81–131.

(143) Zhou, D.; Wu, H.; Wei, Z.; Han, B.-H. Graphene-Molybdenum Oxynitride Porous Material with Improved Cyclic Stability and Rate Capability for Rechargeable Lithium Ion Batteries. *Phys. Chem. Chem. Phys.* **2013**, *15* (39), 16898–16906.

(144) Ji, W.; Shen, R.; Yang, R.; Yu, G.; Guo, X.; Peng, L.; Ding, W. Partially Nitrided Molybdenum Trioxide with Promoted Performance as an Anode Material for Lithium-Ion Batteries. *J. Mater. Chem. A* **2014**, *2* (3), 699–704.

(145) Wang, X.-J.; Krumeich, F.; Wörle, M.; Nesper, R.; Jantsky, L.; Fjellvåg, H.

Niobium(V) Oxynitride: Synthesis, Characterization, and Feasibility as Anode Material for Rechargeable Lithium-Ion Batteries. *Chemistry* **2012**, *18* (19), 5970–5978.

(146) Chen, T.-T.; Liu, H.-P.; Wei, Y.-J.; Chang, I.-C.; Yang, M.-H.; Lin, Y.-S.; Chan, K.-L.; Chiu, H.-T.; Lee, C.-Y. Porous Titanium Oxynitride Sheets as Electrochemical Electrodes for Energy Storage. *Nanoscale* **2014**, *6* (10), 5106–5109.

(147) Wu, Y.; Liu, X.; Yang, Z.; Gu, L.; Yu, Y. Nitrogen-Doped Ordered Mesoporous Anatase TiO_2 Nanofibers as Anode Materials for High Performance Sodium-Ion Batteries. *Small* **2016**, *12* (26), 3522–3529.

(148) Lu, P.-J.; Lei, M.; Liu, J. Graphene Nanosheets Encapsulated α-MoO_3 Nanoribbons with Ultrahigh Lithium Ion Storage Properties. *CrystEngComm* **2014**, *16* (29), 6745–6755.

(149) Choi, S. H.; Lee, J.-K.; Kang, Y. C. Three-Dimensional Porous Graphene-Metal Oxide Composite Microspheres: Preparation and Application in Li-Ion Batteries. *Nano Res.* **2015**, *8* (5), 1584–1594.

(150) Kühn, S.; Schmidt-Zhang, P.; Hahn, A. H.; Huber, M.; Lerch, M.; Ressler, T. Structure and Properties of Molybdenum Oxide Nitrides as Model Systems for Selective Oxidation Catalysts. *Chem. Cent. J.* **2011**, *5* (1), 42 1-10.

(151) Wang, X. J.; Nesper, R.; Villevieille, C.; Novák, P. Ammonolyzed MoO_3 Nanobelts as Novel Cathode Material of Rechargeable Li-Ion Batteries. *Adv. Energy Mater.* **2013**, *3* (5), 606–614.

Chapter 2

Experimental Techniques and Characterizations

The first section of this chapter aims at describing the details of the ALD reactor and the reaction conditions used to prepare the materials are followed by different in-situ and ex-situ characterization techniques adapted to characterize the ALD grown materials. The whole electrochemical cell fabrication process and different electrochemical techniques are discussed in the later part of this chapter.

2.1 Material Synthesis

All the depositions mentioned in this thesis are carried out in a custom-built hot-wall viscous type flow ALD reactor. The reactor is connected to a rotary vane pump of capacity 250 L/min to maintain the constant vacuum and a capacitance manometer (Baratron) is used to monitor pressure. A schematic diagram of the reactor is represented in Figure 2.1. ALD processes are known to be highly temperature sensitive during the reaction, as discussed earlier. Thus the main reaction chamber is heated with the help of a co-axial tube heater controlled by a PID (proportional, integral, differential) controller for precise control and uniform temperature throughout the chamber. Being the resistive heater, these heaters only heat the outer wall of the chamber, that's why the term 'hot wall' is used. Heat from the wall transferred through convection and radiation processes. After a few minutes, the temperature inside the chamber comes in equilibrium with the wall and produces a uniform temperature profile throughout. Hot walls also help to prevent any condensation on the wall during the reaction. All the components used in the reactor are made of stainless steel (SS 316) along with the substrate holder to prevent any unwanted reactions on the surface.[1]

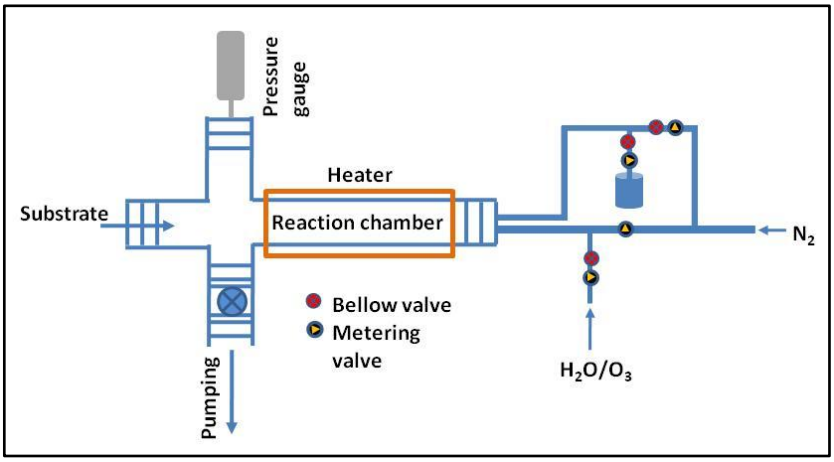


Figure 2.1 Block diagram of custom-built ALD reactor setup used for film deposition.

In the ALD process, the reactants are dosed separately into the reactor else the mixing of reactants would give an uncontrollable and non-conformal deposition. If the molecular flow under high vacuum is considered for separating the reactors, then the whole process will become too slow. However, molecular flow separations give a better understanding of ALD processes when the reactor is attached with a characterization tool like low energy electron diffraction, X-ray photoelectron spectroscopy, Auger electron spectroscopy and Laser-

induced thermal desorption *etc.* Another option of separating the precursors is a flow of inert gas through the reactor after each dose. The flow of inert gas can act as a carrier gas as well as it removes extra by-products after each half reaction. The flow of inert gas is viscus if the operating pressure is sufficiently high (≥ 100 mTorr). This separation also allows the precursor exposures to be closely spaced which also minimize the ALD process time. Therefore, viscous flow ALD reactors are much more popular than molecular flow for rapid production. A constant base pressure of approximately 1 Torr is maintained to create viscous flow by flowing high purity (99.999%) nitrogen gas during the reaction. The N_2 stream ensured the laminar flow of the reactants over the substrate surface.

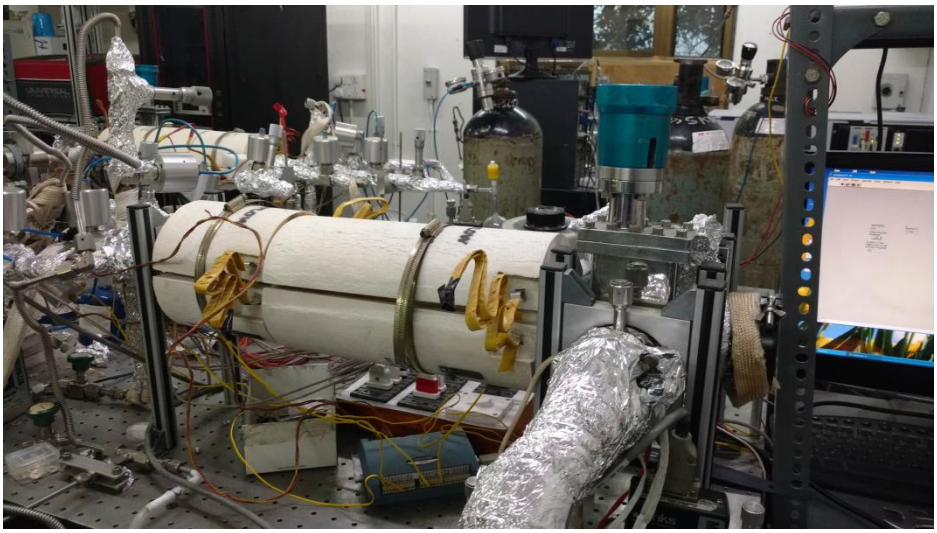


Figure 2.2 photograph of the custom build ALD reactor used for this work

Precursors are injected into the chamber with the help of a series combination of metered valves and computer controlled pneumatic valves. This arrangement ensured controlled dosage of the reactants into the reactor. Most of the precursors were kept at room temperature unless otherwise mentioned and fed to the reaction chamber through differentially heated SS pipes. Overhead arrangements are done for the precursors with very low vapor pressure using N_2 flow as a carrier gas. During the reaction, a minimum of 10s purging time was maintained between two consecutive doses. Figure 2.2 shows the photograph of the custom-built hot wall viscous flow ALD reactor used to deposit all the films during this work. All the films were deposited mostly on glass and Si substrates. To avoid the substrate effect, glass substrates were used to deposit the films to characterize the structural, optical and electrical properties.

On the other hand, Si substrates were used mainly for the thickness measurement due to the smooth substrate surface and few specific characterizations (to be discussed later).

***Precursors used*:** Most of the metal precursors used here for depositions are mainly metal-organic compounds because of their high vapor pressure at room temperature and low deposition temperature. Mo[$(CO)_6$] is used as Mo source, Trimethylaluminum (TMA) as Al source, [$Co_2(CO)_8$] for Co, HPLC grade water (H_2O), ozone gas are used as O-source and NH_3 gas is used as N-source. All the precursors used are with high purity and used as received.

2.2 MWCNT pre-treatment and deposition

Pristine CNTs have initial nucleation problem to deposit any material on it because of their chemically inert side walls. They don't have any defect site or any unsaturated bonds to initiate the nucleation. Therefore, it is essential to functionalize nanotube sidewalls so that it can interact to the ALD precursors.[2] Commercially available MWCNTs (30-50 nm diameter and 10-20 micron length) were pre-treated with the concentrated acid mixture of HNO_3 and H_2SO_4 (1:3) for 12 hours at room temperature to functionalize MWCNT surface. To remove catalyst particles, amorphous carbons and other unwanted species. Acid treatment helps to create carboxyl groups at the nanotube sidewalls. Pre-treated CNTs were then filtered through the Whatman filter paper and washed several times with DI water followed by drying for around 12 hours at 60 ^{0}C. A certain amount of pre-treated MWCNTs was then added in isopropanol to make a stable colloidal solution. Uniform MWCNT layers were deposited on hot stainless steel (SS) substrates by simple drop casting of colloid MWCNT solution.

2.3 Material characterizations

Growth characteristic of the materials is studied by *in-situ* quartz crystal microbalance (QCM) during the deposition process where the mass gain is measured after each reactants exposure.[3] The total mass gain and growth rate per ALD cycle is calculated by converting a corresponding change in frequency to mass using Saurerbrey equation. *In-situ* residual gas analysis (RGA) has been also performed to understand the reaction mechanism during each half cycle. RGA study gives information about the by-products obtained during the reaction. Thus, the information acquired from *in-situ* QCM and RGA study give an idea about the ALD reaction mechanism and growth characteristic of the deposited materials.

Growth rate per ALD cycle calculated from the *in-situ* QCM measurement is again cross-checked by *ex-situ* X-ray Reflectivity (XRR) measurements. Other *ex-situ* measurements are done to study the chemical, physical and optical properties of the deposited films.

2.3.1 *In-situ* characterization

2.3.1.1 QCM study

Different *in-situ* characterizations are mainly carried out to understand the growth behavior and reaction mechanism of the deposited films. The custom built ALD reactor is designed in a manner to be compatible with the QCM setup. Here, the change in resonance frequency resulted from each half-cycle reaction onto the quartz crystal is measured and converted to the mass which is related to the amount of material deposited during the growth process. Mass gain obtained from this gives a precise measurement of the growth rate per cycle of the deposited ALD films. This study also offers to understand the nucleation period and steady-state growth regime differently and accurately.

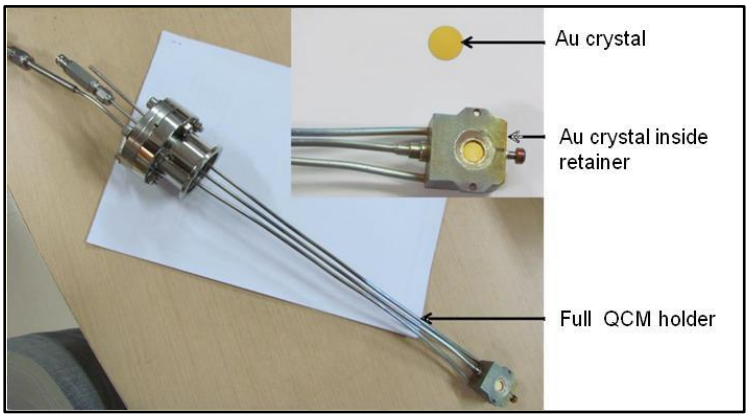


Figure 2.3 Photograph of QCM holder arrangement used for *in-situ* studies

The change in frequency occurs on the crystal (AT-cut gold-coated quartz with 6MHz resonance frequency) due to film deposition is monitored with an SQM-160 Rate/Thickness monitor (Inficon). To minimize the effect of surface roughness during deposition, polished gold-coated quartz crystals are used. Figure 2.3 showing the picture of the QCM holder used for the measurements. Quartz crystals are mounted, assembled and sealed well inside the holder with non-conducting epoxy paste to prevent any unwanted deposition on the backside of the crystal. Then, the whole assembly is placed inside the reaction chamber horizontally with crystal facing upward. In addition to that, a backflow of N_2 pressure of approximately

0.1 Torr is maintained through a pipe internally connected from the back end of the QCM holder to make sure any unwanted deposition does not occur on the back side of the crystal. Sauerbrey equation is used for the conversion of change in resonance frequency (Δf) to corresponding mass gain (Δm).[4] The equation is represented as follows-

$$\Delta f = \frac{-2f_0}{\mathrm{A}\sqrt{\rho_q \mu_q}} \Delta m$$

Where, f_0, Δf, Δm, A, ρ_q and μ_q are resonant frequency (Hz), frequency change (Hz), mass change (gm), active crystal area (cm^2), the density of quartz (gm/cm^3) and shear modulus quartz for AT-cut crystal ($gm.cm^{-1}s^{-2}$) respectively. The thickness of the corresponding ALD grown films is obtained using the mass gain calculated from QCM and the densities obtained from X-ray reflectivity (XRR) measurements.

2.3.1.2 Residual gas analysis (RGA)

Analysis of residual products obtained from a reaction gives information about the mechanism and kinetics of that reaction. During an ALD reaction, the obtained by-products tells about the kind of reactions occurs between the surface species and incoming gaseous reactants. Combining *in-situ* QCM and RGA study often complemented by FTIR measurement (though not used here) provides a complete understanding of any ALD reaction.[5]

During the measurement, an RGA chamber is connected in between the mouth of the reactor and pump connection. The analysis chamber consists of an ion source, a measurement section, and a mass spectrometer. After each dose, the precursors react with the existing surface and form by-products, leaving behind some un-reacted molecules. In the purging step, a fraction of these excess and by-product molecules are collected in the ionizer followed by analysis chamber through a quadrupole mass filter. Ionizer helps to ionize the neutral molecules and accelerate them onto the mass spectrometer. In the mass analyzer region, chosen mass to charge ratio (M/e) passes through to the measurement section. Full spectrum is obtained by sweeping the whole range of M/e ratios during the purging step just after precursor dosage.

In this work, *in-situ* RGA of the two half ALD reactions is performed with an INFICON CPM transceptor gas analyzer consisting of a quadrupole mass filter and anion detector. By-

products of each half cycle were measured in between 1-100 amu scale with 512 ms of gas dwell time. For this study, Ar was used as the carrier gas instead of N_2 because of the same molecular weight of CO and N_2 (both 28 amu). However, during the measurements, Ar was kept off because of a giant peak corresponds to Ar was observed suppressing all other peaks. The resulted spectrum gives a clear idea of the by-products formed and allows a complete understanding of the reaction pathways of two ALD half-reactions.

2.3.2 *Ex-situ* characterizations

Various *ex-situ* characterizations are carried out to investigate the chemical, physical, electrical and optical properties of the deposited materials.

X-ray reflectivity (XRR) measurement is a surface sensitive non-destructive analytical technique used for measuring the thickness, density and roughness of the deposited thin films simultaneously. In this measurement, reflections of incident X-ray beams at a grazing angle are measured. At the interface where the electron densities alter, a part of the beam is reflected and the interference creates an oscillation pattern with respect to the incident angle in reflectance measurements. The obtained interference pattern gives a measure about the thickness of the film. The observed pattern can then be modeled and will obtain the exact thickness, density, and roughness of the understudying film.[6]

In course of this work, measurements are performed in the Rigaku Smartlab diffractometer, equipped with Cu Kα cathode emitting at 1.54Å. Commercially available GlobalFit software is used to model the experimental data. Films are deposited on polished silicon substrates with native SiO_2 for all XRR measurements because of the standard known roughness and also to minimize the interfacial effect on the deposited films.

X-ray diffraction **(XRD)** is another analytical method which gives information about the crystal structure, crystal orientation, lattice parameters and chemical composition of a material. This method is based on detecting the scattered intensity of an X-ray beam falling on a sample as a function of incident and reflected angle. In this work, the crystallographic information of the films was obtained by the XRD measurements using Rigaku Smartlab X-ray diffractometer equipped with Cu-Kα radiation source (1.54 Å). All the films are deposited on a glass substrate to eliminate the effects from the substrate for XRD measurements.

used for the analysis of elemental composition, chemical and electronic states present in the material is measured with the ***X-ray photoelectron spectroscopy (XPS)*** technique. A typical XPS spectrum is obtained by plotting the number of electrons detected per unit volume and unit time vs. the corresponding binding or kinetic energy. Each element has characteristic binding energy values corresponding to their electrons at different levels, *e.g.*, 1*s*, 2*s*, 2*p*, 3*s*, *etc*. Energy values can be shifted depending on the nature of the associated chemical environment. As an example, if an atom is bonded with a highly electronegative atom then the characteristic binding energy value increases with respect to the neutral atom because of the decrease in the electron cloud density on that atom. Intensities of detected electrons obtained at particular binding energy are directly related to the amount of elemental presence in the sampling volume.

Here, all elemental and compositional analyses were performed on a Thermo VG Scientific X-ray photoelectron spectrometer (MultiLab) equipped with Al Kα source (1486.6eV). All the peaks were calculated and adjusted with the standard C 1s peak (at 284.6 eV).

Secondary Ion-Mass spectroscopy (SIMS) measurements were carried out to inspect relative concentration of elements present along the depth of the film. This is also a surface sensitive measurement tool which detects the elemental presence in a film with detection limit ranging from parts per million to parts per billion. In this method, a high energy pulsed ion beam is used to remove the outermost surface of a sample and creates secondary ions. Then the secondary ions are accelerated by an electron accelerator towards the detector through a "flight tube. Mass/charge ratio of the secondary ions are then measured with a mass spectrometer. Mass of a secondary ion is attained by measuring at the time of flight to reach the detector. Usually, the SIMS method is considered as a qualitative characterization technique but quantitative measurement can be done using the standards.[7]

In this work, the instrument used for measurement is a PHI TRIFT V nanoTOF (ΦULVAC-Physical Electronics, MN, USA) in the positive SIMS mode. 30 keV Au^+ ion source is used as a primary beam to bombard the samples as used for high mass resolution spectroscopy. Cs ions were scanned in a raster size of 400 μm × 400 μm in a dual beam mode for sputtering. Alternately the Au/Ga and Cs ions were used to acquire data and sputter the top layer respectively. All the samples acquisition was done in positive SIMS while the depth was measured by Dektak XT from Bruker.

Scanning electron microscope (**SEM**) is used to produce surface images of the samples by scanning the surface with a focused beam of electrons produced from a field emission electron gun. Images enclose information about the surface topography and composition with a resolution of ~1 nm. SEM images were taken with a ZEISS FESEM using a secondary electron detector for this work.

Transmission Electron Microscopy (TEM) is used to investigate the microstructural information of different materials. For TEM measurements the films were scraped from the substrate with a blade and dispersed in water, then put on a grid and dried. TEM imaging was carried out with a JEOL 2100F transmission electron microscope operating at 200kV.

Along with the different characterization techniques discussed so far, few other characterizations are also performed to obtain additional information regarding other properties of the deposited materials.

Different vibrational modes of as-deposited materials are characterized using a **Raman** spectrometer (JobinYvon HR800) equipped with a 514.5 nm laser at 10 mW power. **Ultraviolet photoelectron spectra (UPS)** are recorded using He-I emission under 10^{-8} vacuum. Resistivity and temperature dependent **Hall measurements** are carried out with a LakeShore Model 8404 AC/DC using van der Pauw geometry. The films were deposited on microscopic glass substrates with dimensions of approximately 1 cm × 1 cm for the Hall measurements. **Fourier Transform Infra Red (FTIR)** spectroscopy measurements were performed with a Bruker Vertex 70 in transmission mode. Samples were scraped from the film, heated where needed, and mixed well with KBr powder to form pellets.

2.3.3 Li-ion cell fabrication and electrochemical characterization

All the electrochemical characterizations were done in 2032 coin cells in a half cell assembly i.e. against lithium metal. Half-cell configurations of Li/Electrolyte/ALD deposited films are assembled inside an argon-filled glove box (Lab Star, Mbraun, Germany) with moisture and oxygen concentrations level of ~ 1 ppm.

All the ALD films are directly deposited under self-saturated conditions on bare stainless steel (SS) or CNT coated SS substrate and prepared for electrochemical characterizations. Li foil was used as a counter as well as a reference electrode and 1 M $LiPF_6$ solution in EC/DMC

(1:1 wt/wt) (LP-30, Merck, Germany) was used as an electrolyte. Borosilicate glass microfiber filters (Whatman) soaked in the electrolyte served as a separator in between the two electrodes. All the electrochemical measurements were taken at a constant temperature of 20 ^{0}C with ± 1 ^{0}C accuracy.

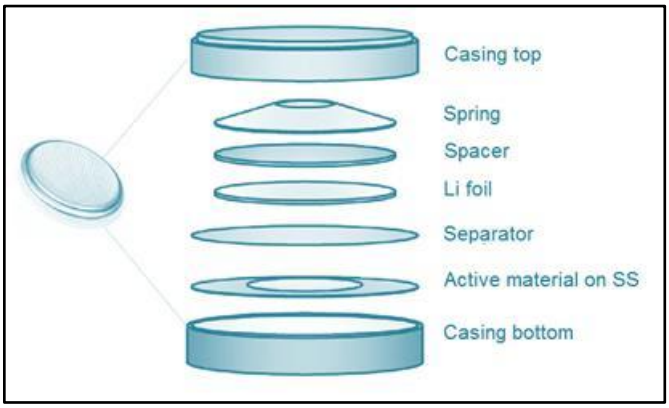


Figure 2.4 Schematic representation of different parts of a 2032 coin cell

Cyclic voltammetry (CV) is a potentiodynamic and cyclic electrochemical characterization generally used to study the redox processes take place in the working electrode with respect to a reference electrode. In this method, the potential of a working electrode is varied linearly with respect to time. The observed current is recorded here with respect to the reference potential. CV measurements were carried out with Bio-logic VMP-3, France.

Galvanostatic charge-discharge cycling is another important characterization tool for any rechargeable battery system. A positive current is applied to the electrode during the discharging process whereas a negative current is applied during charging process respectively inside a potential window. One charge and subsequent discharge process together called as one charge-discharge cycle. These charge-discharge cycles are repeated for number of times to see the electrochemical stability of the electrode. These measurements are performed in BT-2000 test station, Arbin Instruments, USA.

2.4 References

(1) Elam, J. W.; Groner, M. D.; George, S. M. Viscous Flow Reactor with Quartz Crystal Microbalance for Thin Film Growth by Atomic Layer Deposition. *Rev. Sci. Instrum.* **2002**, *73* (8), 2981–2987.

(2) Jin, S. H.; Jun, G. H.; Hong, S. H.; Jeon, S. Conformal Coating of Titanium Suboxide on Carbon Nanotube Networks by Atomic Layer Deposition for Inverted Organic Photovoltaic Cells. *Carbon N. Y.* **2012**, *50* (12), 4483–4488.

(3) Puurunen, R. L. Surface Chemistry of Atomic Layer Deposition: A Case Study for the Trimethylaluminum/water Process. *J. Appl. Phys.* **2005**, *97* (12), 121301 1-52.

(4) Kankare, J. Sauerbrey Equation of Quartz Crystal Microbalance in Liquid Medium. *Notes* **2002**, No. 5, 7092–7094.

(5) Lemonds, A. M.; White, J. M.; Ekerdt, J. G. Surface Science Investigations of Atomic Layer Deposition Half-Reactions Using $TaF_5$and Si_2H_6. *Surf. Sci.* **2003**, *538* (3), 191–203.

(6) Filies, O.; Böling, O.; Grewer, K.; Lekki, J.; Lekka, M.; Stachura, Z.; Cleff, B. Surface Roughness of Thin Layers - A Comparison of XRR and SFM Measurements. *Appl. Surf. Sci.* **1999**, *141* (3), 357–365.

(7) Akin, N.; Ozen, Y.; Efkere, H. I.; Cakmak, M.; Ozcelik, S. Surface Structure and Photoluminescence Properties of AZO Thin Films on Polymer Substrates. *Surf. Interface Anal.* **2015**, *47* (1), 93–98.

Chapter 3

Controlled 3D Carbon Nanotube Architecture Coated with MoO_x Material by ALD technique: A High Energy Density Lithium-ion Battery Electrode

This chapter describes the fabrication of 3D MoO_x/CNT core-shell structure and their application as an anode in Li-ion battery. Material fabrication and characterization followed by their electrochemical performance are discussed here.

In this chapter, we report the growth and electrochemical behavior of ALD grown MoO_x film on planar substrates as well as on MWCNTs layer. *In-situ* QCM measurements are done to understand the self-saturation and ALD temperature window. Residual gas analysis is carried out to prove the two half-reactions during ALD. The as-deposited films are characterized by XPS and Raman spectra. SEM and TEM images showed the conformal coating of MoO_x throughout the CNT surface. MoO_x thickness is varied to see the effect on capacity and rate performance that enabled to optimize the number of ALD cycles required for the composite. Electrodes are further characterized after 50 cycles of charge-discharge.

3.1 Experimental

3.1.1 ALD of MoO_x

Amorphous molybdenum oxide is deposited from molybdenum hexacarbonyl [$Mo(CO)_6$] and ozone (O_3) at 170 ^{0}C in a flow type custom build reactor using N_2 (99.995%) as a carrier and purging gas. Base pressure of the reactor is kept at around 1 Torr for all the experiments. Metal precursor is kept at room temperature and because of its low vapor pressure, an N_2 overhead assembly is used to carry the precursor into the reactor. Dose time of each precursor is kept 1 sec and the purge time in between the two consecutive doses is kept at 15 sec. A number of metal precursor doses are varied to see the self-limiting growth of the films keeping the ozone dose constant. Cleaned silicon wafers and soda lime glasses are used as a substrate for all the film characterizations. Whereas, plain SS and MWCNT coated SS substrates are used for the electrochemical characterization. Figure 3.1 shows the schematic of the development of MoO_x coated MWCNT core-shell nanostructure.

3.1.2 MWCNT pre-treatment and deposition

Since the as-synthesized CNTs have an inert surface, deposition of any material on CNTs is difficult. Therefore, it is essential to functionalize CNT sidewalls so that it can interact to the ALD precursors. The detail of the functionalization and deposition process is discussed in chapter 2.

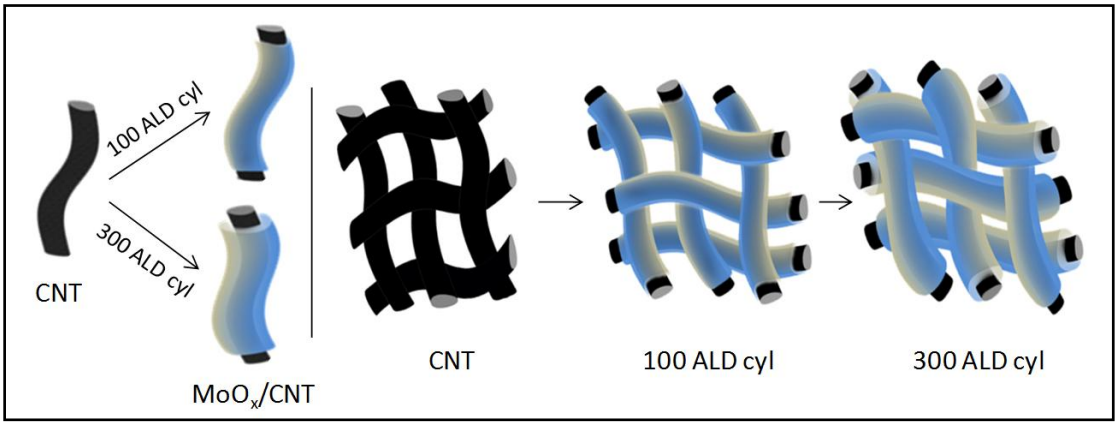


Figure 3.1 Schematic representation of different thickness MoOx coating on porous CNT layer. ALD helps to form a uniform and conformal MoO_x layers without disturbing the interconnected CNT mesh structure. With increasing the number of ALD cycles the thickness of the MoOx layer gets increases and the porosity of the layer decreases.

3.1.3 Electrochemical cell fabrication

All the electrochemical characterizations are done in 2032 coin cells in half-cell assembly i.e. against lithium. A cell configuration of Li/Electrolyte/MoO_x(or MoO_x/CNT) is assembled inside an argon-filled glove box with moisture and oxygen concentrations level of ~ 1 ppm. Four sets of samples are prepared with 100, 300, 500 and 1000 ALD cycles of MoOx on bare SS substrate and CNT coated SS substrate. As deposited MoO_x samples are directly used as an active electrode without adding any binder or any further treatment. Li foil is used as a counter as well as a reference electrode and 1 M $LiPF_6$ solution in EC/DMC (1:1 wt/wt) (LP-30, Merck, Germany) is used as an electrolyte.

CV measurements are performed within the voltage range of 0.1 - 3.0 V vs. Li/Li^+ at a scan rate of 0.2 mV s^{-1} while the charge-discharge performance is scanned from 0.1 V to 2.5 V vs. Li/Li^+ at a current density of 50 µA cm^{-2}. Electrochemical impedance spectroscopy (EIS) experiments are carried out at open circuit voltage (OCV), within a frequency range from 1 MHz to 0.01 Hz using Bio-logic VMP-3. All the electrochemical measurements are taken at a constant temperature of 20^{o}C.

3.2 Results and Discussions

3.2.1 Growth study by *in-situ* QCM

The ALD reaction of molybdenum oxide deposition using [$Mo(CO)_6$] and ozone (O_3) can be split into two separate half-reactions-

$\Vert$-$Mo(CO)_x$* + O_3 → $\Vert$-Mo-O* + xCO (A)

$\Vert$-Mo-O* + $Mo(CO)_6$ → $\Vert$-Mo-O-$Mo(CO)^*_x$ + (6-x) CO (B)

Where, * denotes the surface species.

Surface functional groups present on the substrate react with the incoming precursors that are dosed into the reactor. Reactions will continue till the entire surface species gets reacted and the unreacted reactants along with the byproducts will be purged away from the chamber. The newer surface species formed after the first half cycle then expect to react with the next precursor and the cycle continue to form a film. This self-limiting reaction facilitates the layer-by-layer growth.

As earlier stated, repeating those two half cycles sequentially ensures molybdenum oxide deposition. During the reactions, $Mo(CO)_6$ and O_3 dosing and purging time is followed by time sequence (n)t1-t2-(m)t3-t4, where t1 and t3 depict the dose times for reactant-1 and 2 respectively (kept constant at 1 sec) while t2 and t4 portray the purge times in between consecutive reactant doses (kept constant at 15 sec). Here, n and m represents the respective number of reactant exposure. Figure 3.2a illustrate the mass gain during the deposition of molybdenum oxide for the first few cycles in 1-15-1-15 pulse sequence at 170 ^{0}C.

The growth characteristic is observed to be linear with an average mass gain of 60 ng cm^{-2} per ALD cycle as shown in Figure 3.2b. Individual mass gain of $Mo(CO)_6$ and O_3 is found to be 38.5 and 21.3 ng cm^{-2}. Interestingly, absence of nonlinear nucleation during the initial stage of the growth indicates almost zero incubation periods. Beside this, to validate the nature of self-saturating growth, mass gain per cycle is measured with increase in the number of reactant doses. Figure 3.2c represents the growth rate per cycle versus the number of $Mo(CO)_6$ reactant doses. It is observed that the reaction tends to saturate after three doses of metal precursor with a growth rate of approximately 2.5 Å per cycle. However, a single ozone dose is found to be sufficient for saturation (not shown here). Additionally, the study is extended to understand the temperature dependence of the deposition process with *in-situ* QCM. A relatively narrow ALD temperature window was found within the temperature range of 155-170 ^{0}C, as shown in Figure 3.2d. Obtained ALD temperature window for molybdenum oxide deposition is found to be comparable with the earlier result obtained by Discus et al. using same $Mo(CO)_6$ precursor.[1]

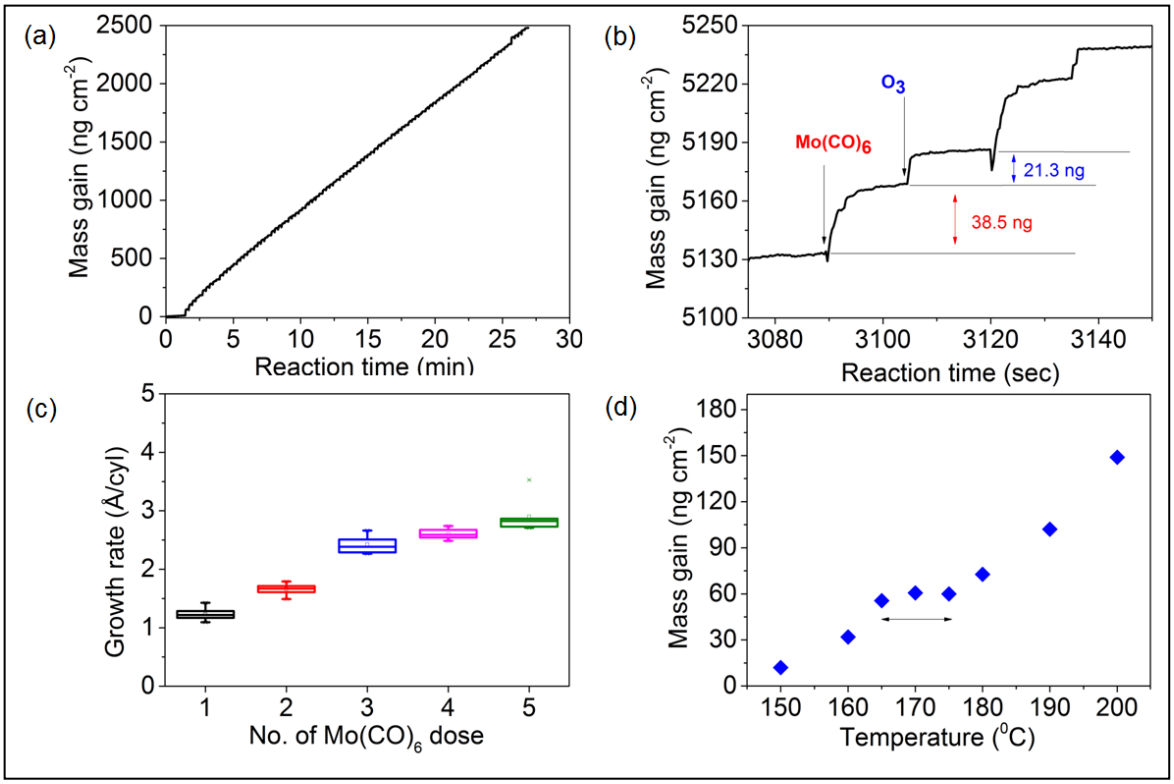


Figure 3.2 (a) Mass gain with ALD cycles monitored by *in-situ* QCM at a substrate temperature of 170 ^{0}C, (b) mass change during $Mo(CO)_6$ and O_3 precursors dose at 170 ^{0}C, (c) growth rate *vs.* no. of $Mo(CO)_6$ dose and (b) mass change with substrate temperature variation.

3.2.2 Residual gas analysis (RGA)

The self-limiting nature of the ALD MoO_x using $Mo(CO)_6$ and O_3 as two precursors have been reported earlier with the help of *in-situ* quartz crystal microbalance (QCM). In this work, we go one step further to explore the two-step mechanism of the ALD reactions. We performed *in-situ* residual gas analysis (RGA) of the two half-reactions with INFICON CPM transceptor gas analyzer consisting of a quadrupole mass filter and anion detector. By-products of each half cycle are measured in between 1-100 amu scale with 512 ms of gas dwell time. For the RGA study, Ar is used as the carrier gas instead of N_2 because of the same molecular weight of CO and N_2 (both 28 amu). However, during the measurements, Ar is kept off because of a huge peak corresponds to Ar is observed suppressing all other peaks.

The expected by-products of both the half reaction are carbon monoxide along with the un-reacted species. Figure 3.3 shows the spectra taken immediately after $Mo(CO)_6$ dosing. A single peak at 28 amu represents the emission of CO as the only by-products. We did not find any peak after purging for few second which indicates the completion of the first half reaction. Similarly, for the other half-reaction, the spectrum is taken immediately after dosing

ozone into the reactor. As expected, peak at 28 amu came from the CO molecule which got replaced with O-atom to form one layer of MoO_x film. Other peaks coming at 16 and 32 amu are due to the un-reacted atomic oxygen and oxygen molecules respectively. A blank spectrum again is found after purging for few seconds. So the two half-reactions during ALD of MoO_x can be written as follows-

$\Vert$-$Mo(CO)_x$* + O_3 → $\Vert$-Mo-O* + xCO

$\Vert$-Mo-O* + $Mo(CO)_6$ → $\Vert$-Mo-O-$Mo(CO)^*_x$ + (6-x) CO

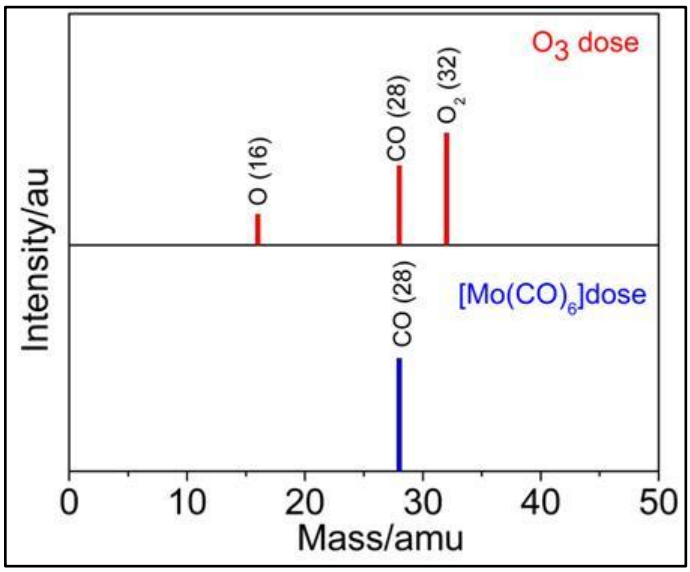


Figure 3.3 RGA spectra recorded right after $Mo(CO)_6$ and ozone dosing

3.2.3 Film characterization

For *ex-situ* characterizations, the films are grown at 170 °C and under the self-saturating condition as discussed in our earlier work.[2] It is found that the as-deposited material is X-ray amorphous in nature. X-ray photoelectron spectroscopy (XPS) of the as-deposited film is studied to understand the chemical nature and electronic state of the material. Figure 3.4(a) shows the complete XPS survey of the as-grown film in the binding energy (BE) range of 0-1000 eV. It is well known that the molybdenum has several oxidation states but the peaks at 232.3 and 235.6 eV (in figure Figure 3.4(b))correspond to the BE of Mo $3d_{5/2}$ and $3d_{3/2}$ electrons of the Mo^{+6} valency state that agreed well with the literature values.[3,1] The calculated atomic ratio of Mo with respect to O is approximately 1:2.95, which suggest the material is slightly oxygen deficient. No other impurities are seen in the survey except a very negligible amount of C (<0.1 atomic %).

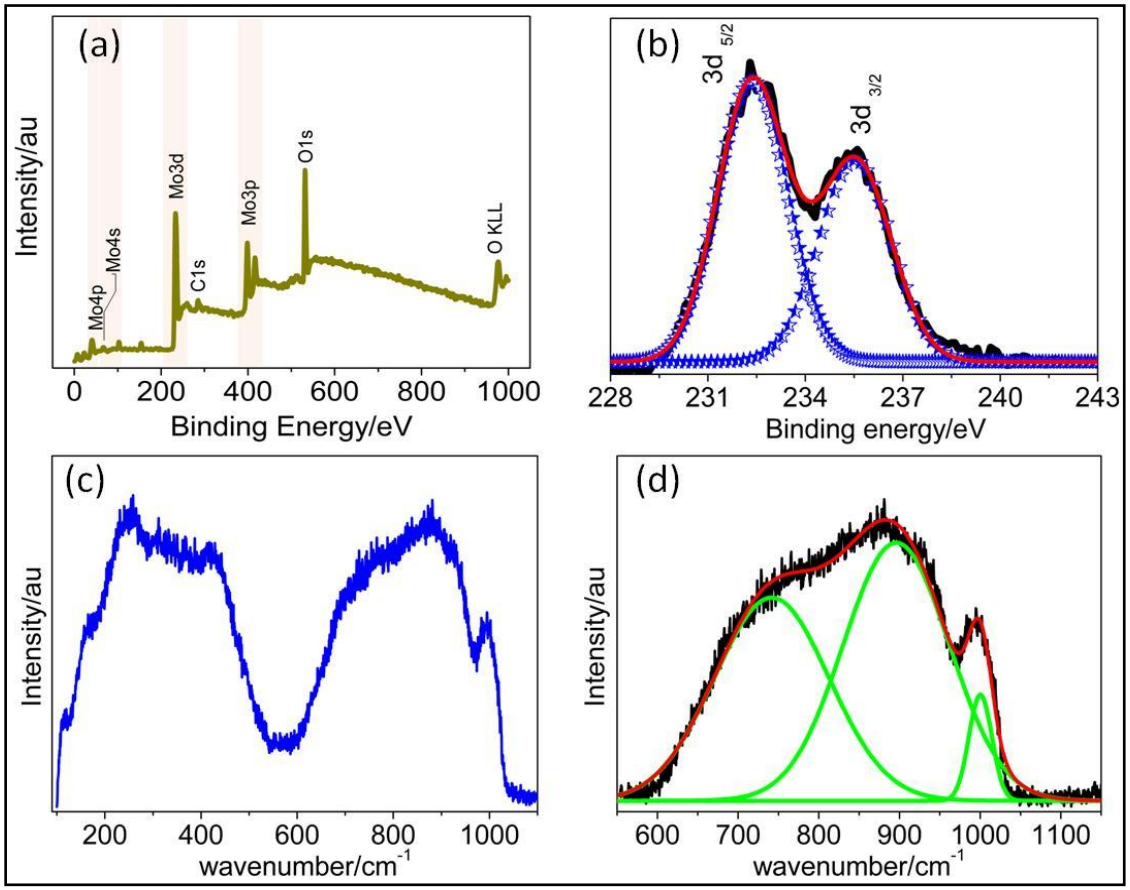


Figure 3.4 (a) XPS survey of as ALD MoO_x film on Si substrate, (b) high-resolution Mo 3d core level XPS scan, (c) Raman spectrum of as-deposited MoO_x film and (d) de-convoluted Raman peaks in the range of 600-1100 cm^{-1}.

Raman spectra of the as-deposited MoO_x film are presented in Figure 3.4(c). Because of the amorphous nature, as deposited MoO_x showed two broad Raman peaks instead of multiple sharp peaks, which is usually found in highly crystalline materials. Major vibration peaks are observed at 115, 160, 250, 316, 336, 367, 422, 880 and 994 cm^{-1}. Peaks in the region of 100-600 cm^{-1} and 600-1000 cm^{-1} can be assigned to the deformation (wagging and scissoring vibrations) and stretching vibration modes respectively.[4] Three distinct peaks can be observed if we deconvolute (Figure 3.4 (d)) the broad region from 600 to 1000 cm^{-1}. The peak at 994 cm^{-1} is the signature vibration of terminal Mo=O bond for MoO_6 building block of layered MoO_3 structure. So, this is an indication that the amorphous film possesses a similar kind of edge-shared MoO_6 building block structure. Peaks at 880 and 740 cm^{-1} are the vibrations of Mo-O_2 (doubly co-ordinate O-atom) and Mo-O_3 (triply coordinated O-atom) bonds respectively. Similar kind of study can also be found for amorphous MoO_3 in the literature.[5,6] Raman study by Discus et al. also illustrated that the amorphous MoO_3 film bear a resemblance to the orthorhombic type edge shared MoO_6 octahedral structure.[7]

3.2.4 Electrochemical Characterization

3.2.4.1 Lithiation/deliathiation reactions in commercial MoO_3 powder

There are few literatures which tried to explain the intercalation and de-intercalation of Li^+ ion in α-MoO_3 crystals. In the case of conversion electrode, lithium insertion-extraction mechanism is still not well established. Here, the mechanism of lithium insertion and extraction of commercial MoO_3 is tried to elucidate in two voltage ranges, one is in between 3-0 V and another is 3-0.6 V. In the second case material is not allowed to go conversion reaction, only Li intercalation/de-intercalation takes place whereas other did. *Ex-situ* XRD, XPS is done at different potential along with CV to get specific information about lithiation/de-lithiation mechanism in commercial α-MoO_3.

Figure 3.5(a,b) showing the CV of commercial α-MoO_3 in the range of 3-0.01 and 3-0.6 V. In first discharge the peaks coming above 1V are due to the intercalation of Li+ ions into the crystal of MoO_3. The peak at 2.7 V is ascribed as the irreversible phase transition from MoO_3 to Li_xMoO_3(where, $x<0.25$).[8]Highly reversible Li+ ion interlayer intercalation into the layer structure occurs at 2.3 V. A strong cathodic peak at a lower potential (0.3 V) is due to the full conversion reaction. In the anodic sweep it is shown that multistep delithiation occurred at 1.4 and 1.8 V. A small peak at 2.5 V assumed to be the de-intercalation peak from unconverted Li_xMoO_3. In the second cycle, two intercalation peaks are found at 1.3 and 1.6 V and rest of the peaks remain the same. Solid electrolyte interface (SEI) is formed at 0.8 V in the first delithiation which is absent from 2nd cycle onwards. On the other hand, reversible oxidation/reduction pair is observed at 2.55/2.26 V respectively when the voltage range restricted in 3-0.6 V range.[9,10,11]

Ex-situ XRD of α-MoO_3 electrodes at a different potential (Figure 3.5c) is taken to understand the phase transformation throughout the charge/discharge process. After first intercalation *i.e.* when the cell is discharged to 2.5 V three phases are observed Li_xMoO_3 (where $x<0.25$), Li_yMoO_3 (where $0.3<y\geq0.5$) and unreacted MoO_3. Similar kind of observation found by Tsumura et al. and Iriyama et al.[9,12] Formation of Li_xMoO_3 ($0.5<x\geq1.5$) is prominent and the pristine phase almost got vanished when the reaction proceeds to the second intercalation. Interestingly the electrodes become almost amorphous after conversion process where electrodes convert to Mo metal and Li_2O. This is well known that nanograins of metal which

formed inside the Li_2O matrix after conversion reaction and they are usually not detectable under XRD.

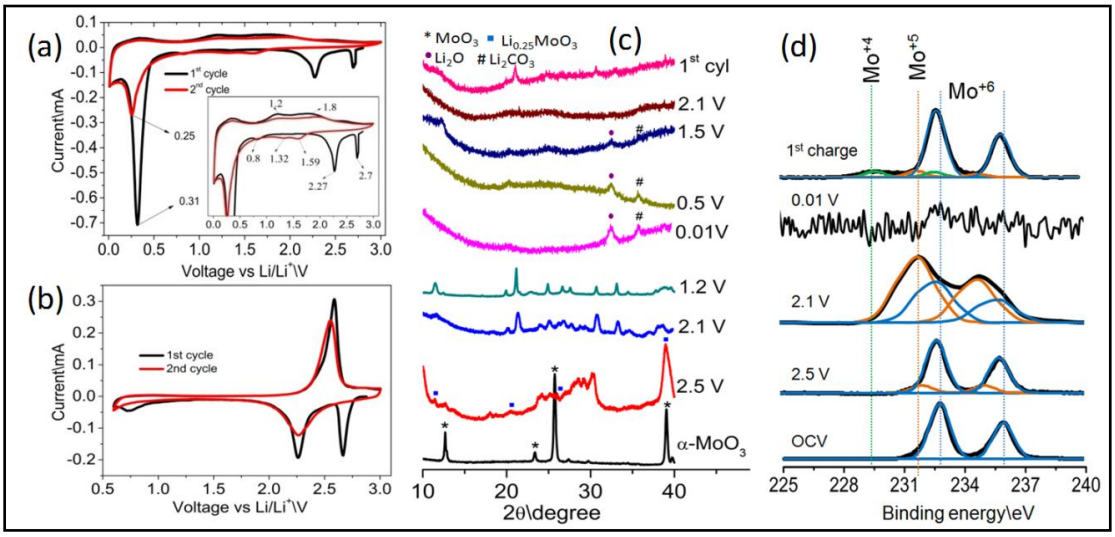


Figure 3.5 Cyclic voltammetry of commercial MoO_3 powder at a scan rate of 10 µV/S in the range of (a) 3-0 V and (b) 3-0.6 V vs Li/Li^+. (c) ex-situ XRD study of MoO_3 electrodes at a different potential and (d) ex-situ XPS Mo-3d profile of MoO_3 electrodes at different potentials.

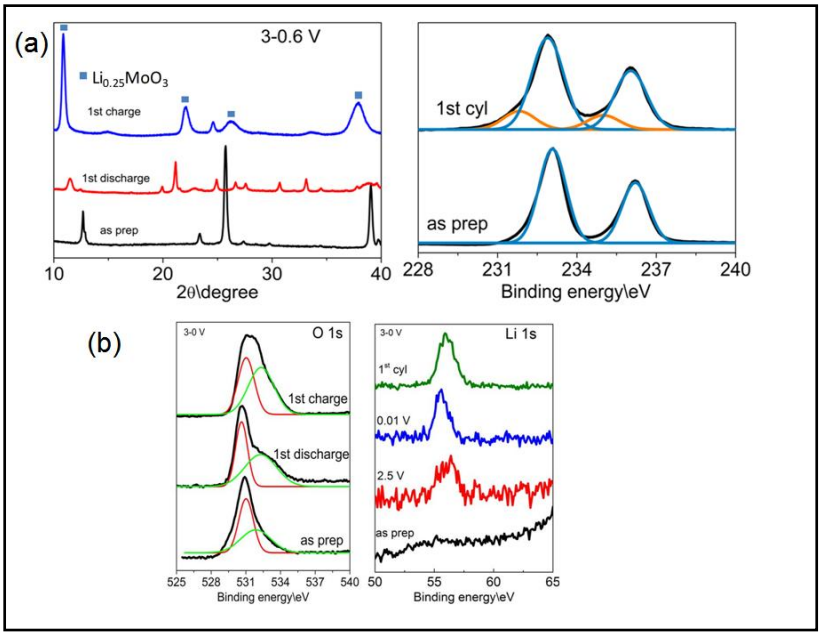


Figure 3.6 (a) XRD and XPS spectra of commercial MoO_3 powder (3-0.6 V range) at a different potential (b) XPS peaks of O-1S and Li-1S at a different stage of lithiation and delithiation.

In the charging process, electrodes remain almost amorphous except the Li_2O phase (peaks at 32.4 and 35.7). XRD after the first charge showed that the electrodes didn't go to its initial MoO_3 phase and formation of lithiated MoO_3 phase is noticed.[13] on the other hand, when the

electrode is restricted in 3-0.6 V range, the crystalline nature is retained after the first cycle. Evolution of Li_xMoO_3 (where, $x \geq 0.25$) after 1st charge process is observed in the case of 3-0.6 V cyclic range also which is shown in Figure 3.6a. Some lithium ions are still trapped inside the crystal which can't be revert back.[11]

XPS study is carried out to understand the valence state of molybdenum at a different stage of the lithiation-delithiation process. As prepared electrode showed only Mo^{+6} valency present in the sample (Figure 3.5d). After the first lithiation till 2.6 V the XPS peak of Mo^{+6} shifted towards lower binding energy and also the formation of Mo^{+5} is also observed. The second intercalation causes further reduction and a huge peak corresponding to Mo^{+5} appears along with Mo^{+6}. XPS peaks in a fully lithiated state highly attenuated due to the formation of thick SEI layer as well as Li_2O formation. This kind of phenomena already reported for other anode materials in the fully lithiated state.[14] It is found that the electrodes didn't go to its initial stage after a 1st cycle which is already proved by the XRD and CV. The appearance of Mo^{+4} along with slightly shifted Mo^{+6} peaks tells that probably the oxidation of Mo metal occurred in two steps. First, it converted from Mo to $Li_2MoO_3$and then further oxidized to Li_xMoO_3 after full delithiation. Hence the presence of two intercalation peaks at 1.59 and 1.32 V in 2nd discharge also could be due to the formation of two different phases formed after the 1st charge. In another case *i.e.* 3-0.6 V range also electrode didn't come to the initial phase after the 1st cycle. XPS peaks of oxygen and lithium at different stages are also shown in Figure 3.6b. Presence of two kinds of Li in the electrode is observed which can be found while discharging. One would be the Li which is intercalated into the crystal and other would be originated from the Li_2O species after conversion reaction.

3.2.4.2 Cyclic Voltammetry of ALD MoO_x electrodes

Figure 3.7(a,b) represents the cyclic voltammetry (CV) of the bare MoO_x and MoO_x coated MWCNT electrodes on stainless steel (SS) substrate. As it is observed, three peaks are obtained at 2.3, 0.33 and 0.15 V vs. Li/Li^+during the first cathodic sweep when MoO_x electrode is cycled within 3.0 V to 0.01 V against Li/Li^+. The broad peak at 2.3 V is ascribed for the irreversible Li^+ insertion into the interlayer of MoO_3.[15,16] The other two peaks at 0.33 V and 0.15 V can be assigned to the conversion reaction between MoO_x and Li^+ ion to form Mo metal and Li_2O ($MoO_x + xe^- + xLi^+ \rightarrow Mo + Li_2O$).[17] During the anodic sweep, four peaks at 0.45, 1.26, 1.8 and 2.5 V vs Li/Li^+ are observed. The peak at 2.5 V can be assigned

for the delithiation reaction from unreacted Li_xMoO_x (where $0.3<x\leq0.5$). It is further seen that the intensity of the peak at 2.5 V diminishes upon cycling. The peaks at 0.45, 1.26 and 1.8 are originated due to multi-step oxidation of Mo to form MoO_x. In the consecutive cycles, a new peak at 1.6 V is observed during the discharge process which is ascribed for the intercalation of Li^+ ion into MoO_x matrix. Similar observations are also found in previous reports.[10,17–20]

The CV performance of MoO_x/MWCNT electrode is shown in Figure 3.7(b) which is quite identical to the bare MoO_x. However, little shift in the peak positions is observed from the bare MoO_x electrode. The cathodic peaks at 1.26 V and 1.8 V are shifted to 1.4 V and 1.89 V in case of MoO_x/MWCNT electrode, whereas the anodic peak at 1.6 V is also shifted to low potential i.e, at 1.42 V. Peaks at around 0.01V during discharge and 0.13 V during charge are the characteristic lithium intercalation-deintercalation with MWCNTs (see sec. 3.2.4.4). Shifting of cathodic peaks to the lower potential and anodic peaks to higher potential could be due to the different polarization potential arise at the interface of CNT and MoO_x.[21] CV results revealed that the ALD MoO_x closely follows the electrochemical behavior of commercial α-MoO_3.

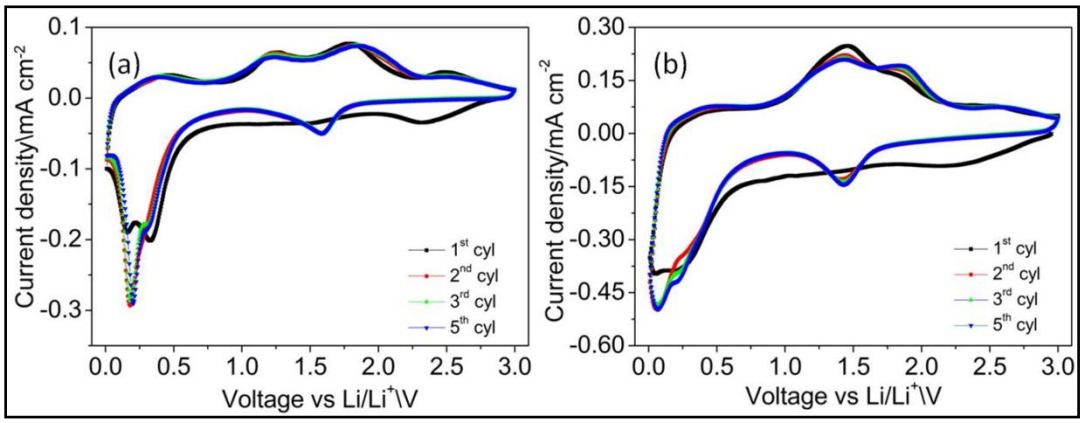


Figure 3.7 cyclic voltammograms of (a) an as-deposited bare MoO_x electrode and (b) a MoO_x/MWCNT electrode at a scan rate of 0.2 mVs^{-1} within a potential window of 3-0.1 V against Li/Li^+.

3.2.4.3 Charge-discharge cycling of ALD MoO_x electrodes

For 2D bare MoO_x electrode: Charge-discharge performance is studied in a potential range of 3-0 V vs. Li/Li^+ at a constant current rate of 50 µA cm^{-2}. Figure 3.8(a) compares the areal capacity of four different planer samples of bare MoO_x (100, 300, 500 and 1000 ALD cycles) deposited on the SS substrate. The areal capacity of 30, 37, 43 and 90 $\mu A.cm^{-2}$ are obtained at the end of the first discharge process from the 100, 300, 500 and 1000 ALD cycles bare MoO_x on SS plate respectively. More capacity for more number of ALD cycles is expected, as with

more ALD cycles, more materials will be deposited on the SS plate which leads to more capacity addition. However, capacity retention depends upon various factors such as lithium diffusion length, porosity, and material loss. In all the parameter higher loading of material expected to perform badly. As a reason, severe capacity fading is observed in the case of an electrode made with 1000 ALD cycle. While the other three electrodes exhibit comparatively stable electrochemical performance. Figure 3.8(b) is showing the galvanostatic charge-discharge profile (voltage vs. areal capacity) for all the four samples at the 1st cycle. Plateaus obtained during charge-discharge processes are in good agreement with the cyclic voltammetry. Figure 3.8(c) and (d) showed the SEM images of 1000 ALD cycle MoO_x film before and after 100 cycles of charge/discharge. Large structural and volumetric changes during the charge-discharge processes cause to lots of crack formation in the films and Coulombic efficiency of all the electrodes are falling down as cycling go on except 100 ALD cycle electrode.

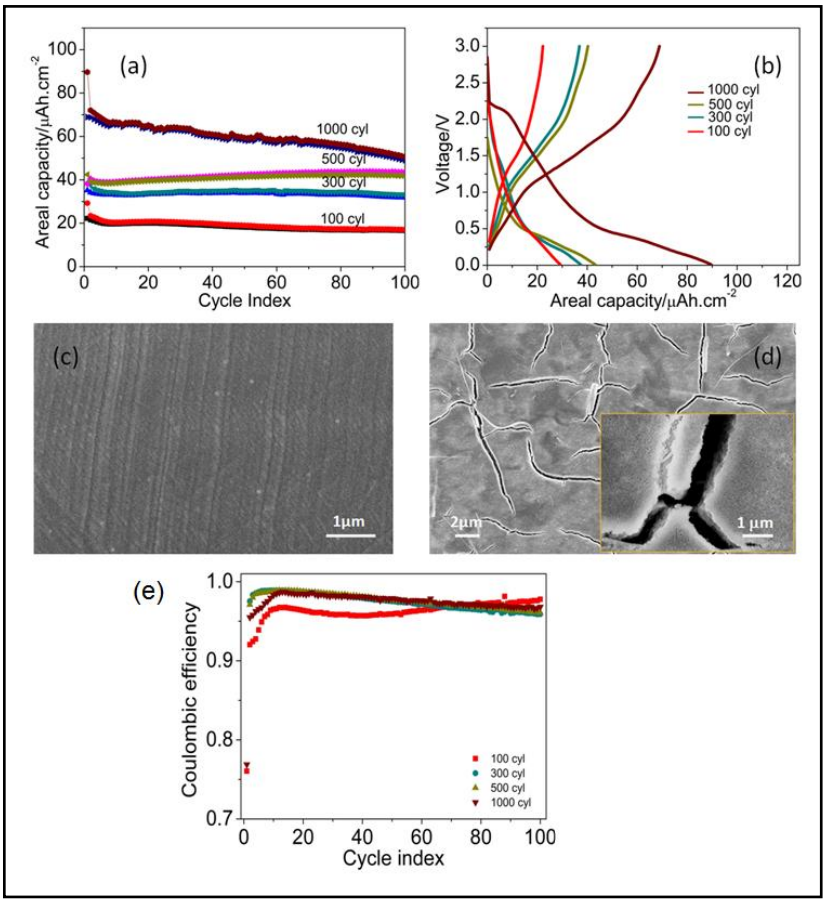


Figure 3.8 electrochemical characterization of as-deposited MoO_x grown on SS substrate. (a) Areal discharge capacity and (b) 1st cycle charge-discharge profiles of 100, 300, 500 and 1000 cycle MoOx electrodes, (c-d) show the SEM images of a 1000 ALD cycle before and after cycling and (e) Coulombic efficiency of all four samples.

For MoO_x/CNT 3D structure: The use of CNT as a template layer or anchoring layer for the metal oxide has multiple advantages. The porous scaffold of CNTs will give a high surface for the oxide layer. The high conductivity of CNTs will give room for a high rate of charging-discharging with high Coulombic efficiency. It can also tolerate the stress and strain of the high structural and volumetric changes of active material during charge-discharge cycling. Last but not least; CNTs also actively participate in the electrochemical process with Li to contribute in the overall capacity of the cell. Because of the thin layer of oxide material deposited by ALD, it allows lithium-ions to diffuse easily and interact with CNTs.

Figure 3.9 shows the surface SEM images of bare CNTs and CNTs coated with MoO_x for different ALD cycles (100, 300, 500, and 1000). As deposited CNT films formed an interconnected network, where the points of contacts are not disturbed after coating. Highly uniform, conformal and full coverage of each CNT sidewall can be observed throughout the electrode after the ALD coating. The outer diameter of the MoO_x coated CNTs increases with increasing cycle number. The thickness of the MoO_x layer on CNTs is approximately 12 nm, 25 nm, 56 nm and 115 nm obtained from 100, 300, 500 and 1000 ALD cycles respectively. Pores are almost disappeared from and beyond 500 cycles of ALD coating which confines the films to be grown two-dimensionally.

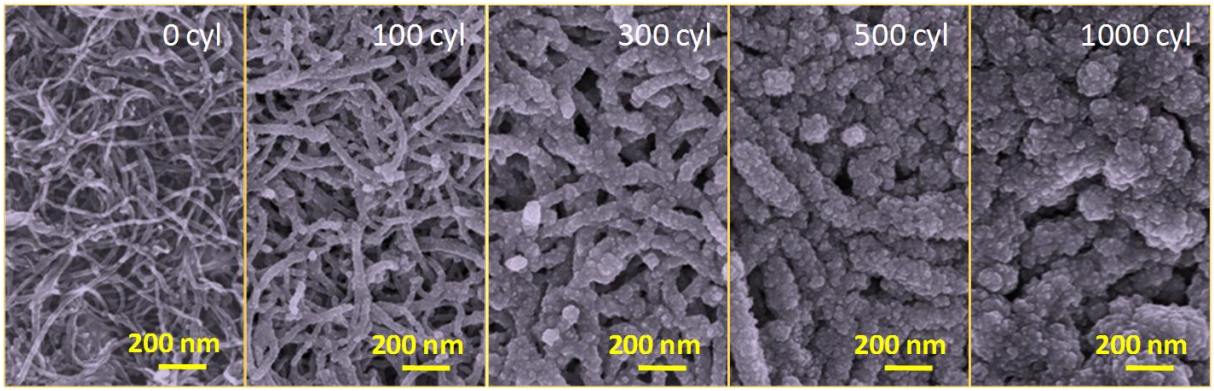


Figure 3.9 SEM images of MWCNTs after different ALD cycles (0, 100, 300, 500 and 1000) of MoO_x coating.

Amount of MoO_x deposited with different ALD cycles on CNTs is measured before and after deposition with microbalance with microgram precision. A total mass of 0.4037, 0.704, 0.85 and 1.148 mg cm^{-2} is measured from the 100, 300, 500 and 1000 cycle CNT/MoO_x electrodes. The ratios of active mass to the total composite mass vary from 33 to 76 %. A mass increase of up to 45 times is observed using the CNT scaffold than the planar counterpart. Charge-

discharge characteristics of all four different MoO_x coated MWCNT electrodes are carried out from 3 V to 0 V vs. Li/Li^+ are shown in Figure 3.10.

Areal capacities of 265, 789, 1169, 1330 μAh cm^{-2} and 176, 620, 930, 1030 μAh cm^{-2} are obtained from the 100, 300, 500 and 1000 cycle ALD MoO_x coated CNT electrodes in their first discharge and first charge cycles respectively (Figure 3.10a). Bare CNT electrodes give approximately 20 μAh cm^{-2} average stable capacity (Figure 3.11). 3D MoO_x/MWCNT structure showed much more improved areal capacity over their planar counterparts (max ~27x) and bare MWCNTs (max ~66x). Specific discharge capacities of 649, 1118, 1164, 1374 mAh g^{-1} at first cycle and capacities of 475, 915, 721, 582 mAh g^{-1} after 50 cycles are obtained from the 100, 300, 500 and 1000 ALD cycle electrodes respectively (Figure 3.10b). Lithiation-delithiation profiles of all the electrodes in their first cycle are shown in Figure 3.10c. This is interesting to note that, while 100 and 300 cycle electrodes showed excellently stable capacity, continuous decay of capacity is observed for 500 and 1000 ALD cycle electrodes. The reason of such kind of behavior due to the limited accessibility of electrolyte to the active layer and also the increase in the thickness of the insulating active layer prevents the electron transfer at electrode-electrolyte interfaces.[22] All of the electrodes showed (showed in Figure 3.10d) Coulombic efficiency above 97% after few cycles and among them 300 ALD cycle electrode shown highest efficiency of approximately 99%.

Figure 3.10e shows the rate capabilities of different electrodes with different current densities of 50, 100, 200, 500 μA cm^{-2} respectively. Five charge-discharge cycle sequences are carried out at each current density to ensure the stability of the electrodes. A total of approximately 42%, 70%, 73% and 76% of initial capacity is retained in case of 100, 300, 500 and 1000 ALD cycle electrodes respectively while ten times increase in the current densities from 50 to 500 μA cm^{-2}. We believe such good rate capability of the electrodes comes from the MoO_x/MWCNT core-shell structure, which provides high electronic and ionic conduction through the MoO_x layer. The detail comparisons of capacity retention with different charging rates (‘C’ rate) are given in Table 3-1.

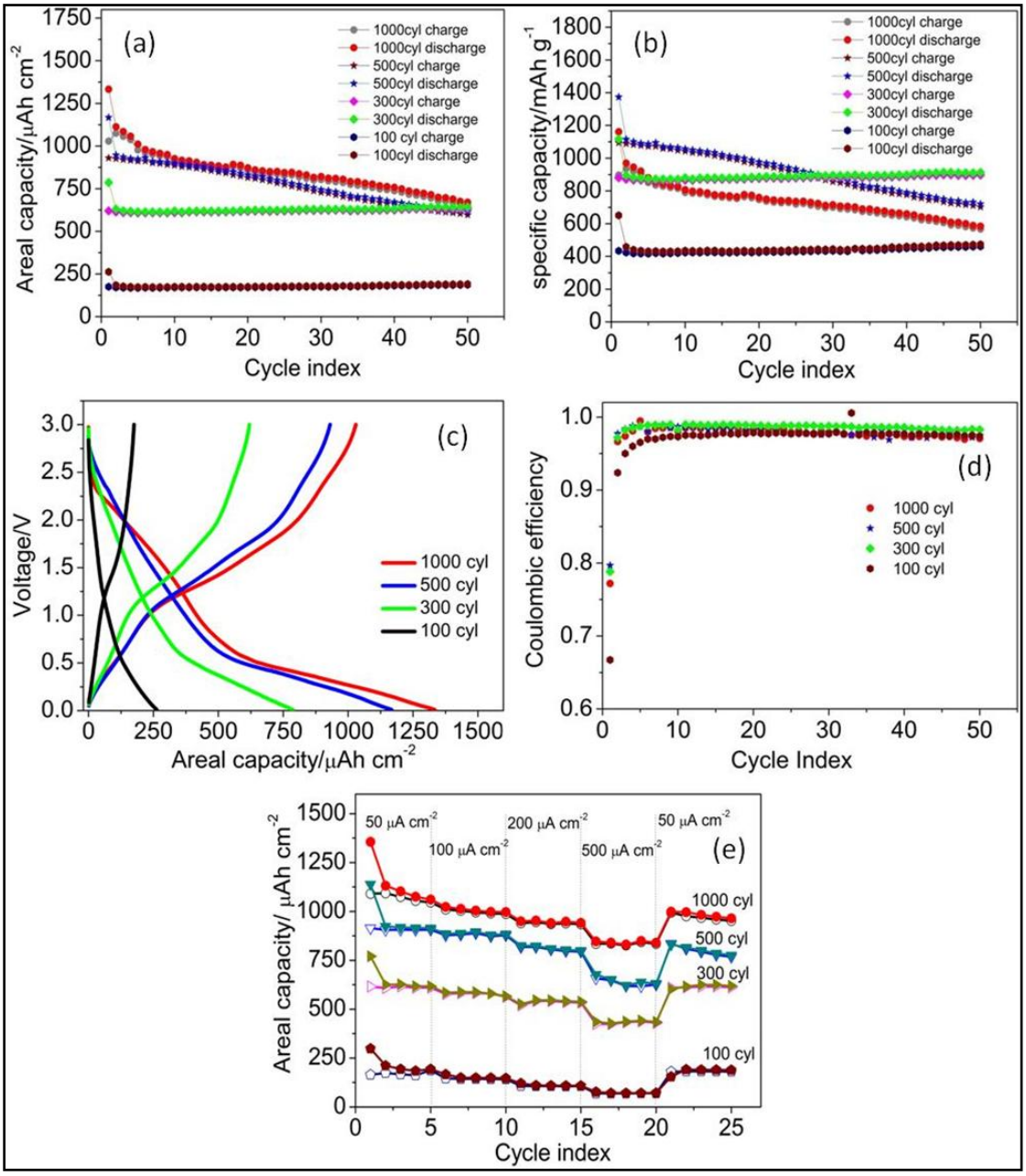


Figure 3.10 Electrochemical comparison of different MoOx/MWCNT electrodes. (a,b) areal and specific capacity comparison, (c) 1st cycle charge-discharge profiles, (d) Coulumbic efficiency and (e) rate performance of 100, 300, 500 and 1000 cycle MoOx/MWCNT

Table 3-1 comparison of C-rate and areal capacity for all the electrodes

Current density (μA cm^{-2})	100 cycle electrode		300 cycle electrode		500 cycle electrode		1000 cycle electrode	
	'C' rate	Areal capacity (μAh cm^{-2})	'C' rate	Areal capacity (μAh cm^{-2})	'C' rate	Areal capacity (μAh cm^{-2})	'C' rate	Areal Capacity (μAh cm^{-2})
50	0.3	161	0.16	606	0.12	925	0.1	1068
100	0.6	144	0.32	560	0.24	874	0.2	980
200	1.2	106	0.64	532	0.48	791	0.4	928
500	3	67	1.6	427	1.2	676	1	826

3.2.4.4 Electrochemical characterization of bare CNTs

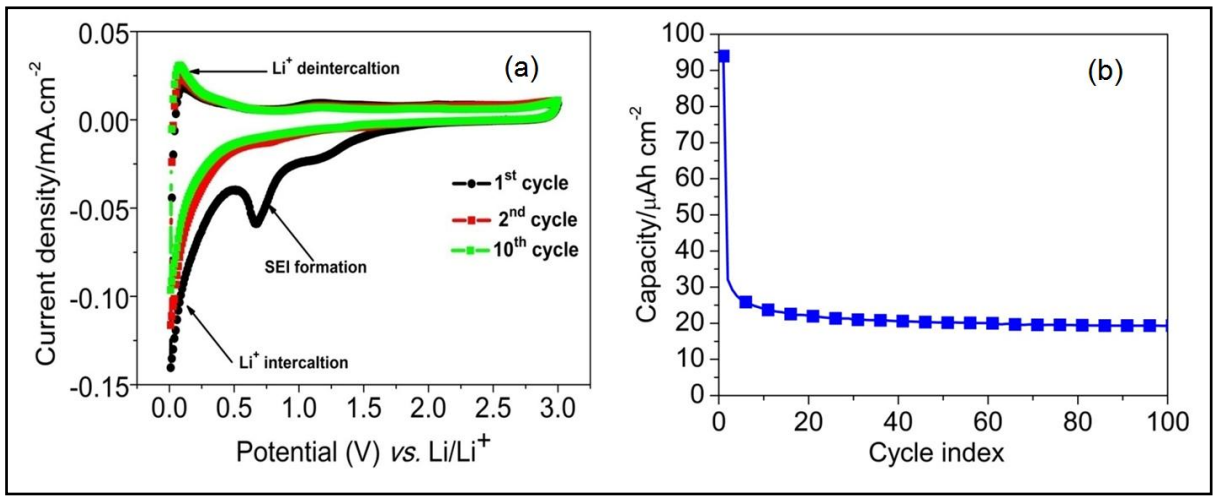


Figure 3.11 (a) cyclic voltammogram and (b) charge-discharge characteristics of bare CNT electrodes.

Figure 3.11 shows the electrochemical behavior of bare MWCNT electrodes with respect to Li/Li^+. Li^+ intercalation occurred at 0.01 V and extraction of Li^+ ions from CNTs is observed at around 0.13 V. The peak at around 0.7 V is assumed to be because of the formation of (SEI layer) at the first cycle which is vanished from 2nd cycle onwards. Charge-discharge characteristic showed a constant and stable capacity of 20 $\mu Ah/cm^2$ is obtained after a few cycles.

3.2.4.5 After cycling characterization

The electrodes are further characterized to see the changes occurred after charge-discharge cycles. The SEM images in Figure 3.12a showed the morphology of all the four MoO_x/MWCNT electrodes after 50 cycles of charge-discharge. No uncoated CNTs can be found after cycling. Oxide layers become rougher and little thicker than that of the as-deposited ones after cycling which is obvious because of the volume changes associated with the Li^+ insertion and removal into/from the metal oxide structures. For 100 and 300 cycle electrodes, the 3D core-shell structure and porous nature are retained even after 50 charge-discharge cycles. However, for 500 and 1000 cycle electrodes, SEM images showed a drastic change in the electrode morphology after cycling which might be the main reason of capacity fading with cycling.

To investigate the electrode structure and morphology change a post-mortem analysis using high-resolution TEM is performed. Figure 3.12b showed the TEM images of 100

cycle MoO_x/MWCNT electrode before and after cycling. A conformal and uniform coating of the MoO_x film on MWCNT is evident from the HRTEM images which remain almost intact after the charge-discharge cycling only the roughness of the coating layer increased complimenting the earlier SEM images. Hence both these SEM and TEM analysis prominently assure the use of the MoO_x/MWCNT 3D core-shell structure as a promising anode for LIBs.

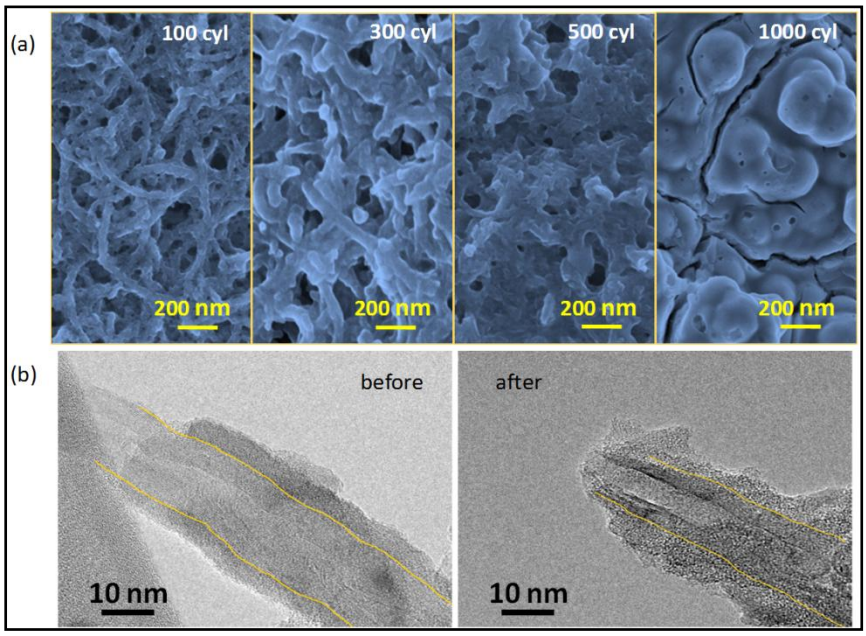


Figure 3.12 (a) Scanning electron microscope images of 100, 300, 500 and 1000 cycle MoO_x/MWCNT electrodes after 50th charge-discharge cycle and (b) TEM images of 100 ALD cycle MoO_x/MWCNT electrode before and after 50 charge-discharge cycles.

3.3 Conclusion

This work shows the electrochemical activity of ALD deposited as-grown amorphous 2D MoO_x film and 3D core-shell MoO_x/MWCNT structure. Precise control of ALD helps to fabricate well controlled different thicknesses of highly robust composite electrodes used for the LIB anode. A maximum areal capacity of 1325 μAh cm^{-2} and specific capacity of 1375 mAh g^{-1} are obtained from the MoO_x/MWCNT electrodes. Among all the four different electrodes 300 cycles ALD coated MoO_x/MWCNT electrode possesses an optimized thickness of MoO_x layer in terms of cycling stability and has the moderate areal and specific capacity (645 μAh cm^{-2} and 915 mAh g^{-1} respectively). Also, this particular electrode showed high capacity retention after 50 cycles (97.5 % with respect to 2nd cycle). Table 3.1 exhibits the stability comparison of

different MoO_3 anodes reported in recent times. This kind of state-of-the-art 3D core-shell nanostructure helps to deposit more amount of active material with the same number of ALD cycles and MWCNT lends a hand to ease the electron transfer during lithiation and deliathiation. Increasing the amount of CNT may further enhance the performance of the electrodes and which is required for all kind of high-performance devices.

Table 3-2 Electrochemical performance comparison of MoO_3 anodes used recent times in Li-ion batteries

Materials	Synthesis Method	Stable Capacity (mAh g^{-1})	Current rate	Capacity retention wrt to 2^{nd} cyl (after '50^{th}' cyl)	Year	Ref.
Carbon coated MoO_3	Hydrothermal	~1064	0.1 C	~85.8 %	2010	[23]
CVD MoO_3	Hot wire CVD	~1050	0.1 C	~90 %	2010	[24]
MoO_3-graphite	Ball milling	~700	0.2 C	~82.5 %	2011	[25]
Ultra long α-MoO_3 nanobelt	Hydrothermal	~900-800	0.2 C	~72.6 %	2012	[26]
α-MoO_3 nanobelt thin film	Hydrothermal	~865	100 mA cm^{-2}	~88.4 %	2013	[15]
α-MoO_3 nanowires	Vacuum topotactic transformation	~955	200 mA cm^{-2}	~77 %	2014	[27]
yolk-shell MoO_3-C microspheres	Spray pyrolysis	~875	1000 mA cm^{-2}	~82.8 %	2014	[28]
Porous-MoO_3 film	Hydrothermal	~750	1C	~86.6 %	2014	[29]
MoO_3 nanorod	Hydrothermal	~657	1000 mA cm^{-2}	~89.6 %	2015	[10]
Assembled MoO_3 sheets	solvothermal	~889	0.1	~89.7 %	2016	[30]
MoO_3-MWCNT	ALD	~915	0.16 C	~97.5 %		This work

3.4 References

(1) Diskus, M.; Nilsen, O.; Fjellvåg, H. Growth of Thin Films of Molybdenum Oxide by Atomic Layer Deposition. *J. Mater. Chem.* **2011**, *21* (3), 705–710.

(2) Nandi, D. K.; Sarkar, S. K. Atomic Layer Deposition of Molybdenum Oxide for Solar Cell Application. *Appl. Mech. Mater.* **2014**, *492*, 375–379.

(3) Bertuch, A.; Sundaram, G.; Saly, M.; Moser, D.; Kanjolia, R. Atomic Layer Deposition of Molybdenum Oxide Using Bis(tert-Butylimido)bis(dimethylamido) Molybdenum. *J. Vac. Sci. Technol. A Vacuum, Surfaces, Film.* **2014**, *32* (1), 01A119 1-6.

(4) Chen, D.; Liu, M.; Yin, L.; Li, T.; Yang, Z.; Li, X.; Fan, B.; Wang, H.; Zhang, R.; Li, Z.; et al. Single-Crystalline MoO3 Nanoplates: Topochemical Synthesis and Enhanced Ethanol-Sensing Performance. *J. Mater. Chem.* **2011**, *21* (25), 9332–9342.

(5) Yang, Y.; Cao, Y.; Loo, B.; Yao, J. Microstructures of Electrochromic MoO_3 Thin Films Colored by Injection of Different Cations. *J. Phys. Chem. B* **1998**, *102* (47), 9392–9396.

(6) Ajito, K.; Nagahara, L. a.; Tryk, D. a.; Hashimoto, K.; Fujishima, a. Study of the Photochromic Properties of Amorphous MoO_3 Films Using Raman Microscopy. *J. Phys. Chem.* **1995**, *99* (44), 16383–16388.

(7) Diskus, M.; Nilsen, O.; Fjellvåg, H.; Diplas, S.; Beato, P.; Harvey, C.; van Schrojenstein Lantman, E.; Weckhuysen, B. M. Combination of Characterization Techniques for Atomic Layer Deposition MoO_3 Coatings: From the Amorphous to the Orthorhombic Alpha-MoO_3 Crystalline Phase. *J. Vac. Sci. Technol. A* **2012**, *30* (1), 01A107.

(8) Hashem, A. M.; Askar, M. H.; Winter, M.; Albering, J. H.; Besenhard, J. O. Two-Phase Reaction Mechanism during Chemical Lithium Insertion into a-MoO_3. *Ionics.* **2007**, *13* (1), 3–8.

(9) Tsumura, T.; Inagaki, M. Lithium Insertion / Extraction Reaction on Crystalline MoO_3. *Solid State Ionics* **1997**, *104* (February), 183–189.

(10) Ahmed, B.; Shahid, M.; Nagaraju, D. H.; Anjum, D. H.; Hedhili, M. N.; Alshareef, H. N. Surface Passivation of MoO_3 Nanorods by Atomic Layer Deposition toward High Rate Durable Li Ion Battery Anodes. *ACS Appl. Mater. Interfaces* **2015**, *7* (24), 13154–13163.

(11) Bullard, J. W.; Smith, R. L. Structural Evolution of the MoO_3(010) Surface during

Lithium Intercalation. *Solid State Ionics* **2003**, *160* (3–4), 335–349.

(12) Iriyama, Y.; Abe, T.; Inaba, M.; Ogumi, Z. Transmission Electron Microscopy (TEM) Analysis of Two-Phase Reaction in Electrochemical Lithium Insertion within α-MoO_3. *Solid State Ionics* **2000**, *135* (4), 95–100.

(13) Jung, Y. S.; Lee, S.; Ahn, D.; Dillon, A. C.; Lee, S. H. Electrochemical Reactivity of Ball-Milled MoO3-Y as Anode Materials for Lithium-Ion Batteries. *J. Power Sources* **2009**, *188* (1), 286–291.

(14) Li, J. T.; Maurice, V.; Swiatowska-Mrowiecka, J.; Seyeux, A.; Zanna, S.; Klein, L.; Sun, S. G.; Marcus, P. XPS, Time-of-Flight-SIMS and Polarization Modulation IRRAS Study of Cr2O3 Thin Film Materials as Anode for Lithium Ion Battery. *Electrochim. Acta* **2009**, *54* (14), 3700–3707.

(15) Sun, Y.; Wang, J.; Zhao, B.; Cai, R.; Ran, R.; Shao, Z. Binder-Free α-MoO_3 Nanobelt Electrode for Lithium-Ion Batteries Utilizing van Der Waals Forces for Film Formation and Connection with Current Collector. *J. Mater. Chem. A* **2013**, *1* (15), 4736–4746.

(16) Zhou, L.; Yang, L.; Yuan, P.; Zou, J.; Wu, Y.; Yu, C. α-MoO_3 Nanobelts: A High Performance Cathode Material for Lithium Ion Batteries. *J. Phys. Chem. C* **2010**, *114* (49), 21868–21872.

(17) Lu, P.-J.; Lei, M.; Liu, J. Graphene Nanosheets Encapsulated α-MoO_3 Nanoribbons with Ultrahigh Lithium Ion Storage Properties. *CrystEngComm* **2014**, *16* (29), 6745–6755.

(18) Liu, C.-L.; Wang, Y.; Zhang, C.; Li, X.-S.; Dong, W.-S. In Situ Synthesis of α-MoO3/graphene Composites as Anode Materials for Lithium Ion Battery. *Mater. Chem. Phys.* **2014**, *143* (3), 1111–1118.

(19) Ma, F.; Yuan, A.; Xu, J.; Hu, P. Porous α-MoO_3 /MWCNT Nanocomposite Synthesized via a Surfactant-Assisted Solvothermal Route as a Lithium-Ion-Battery High-Capacity Anode Material with Excellent Rate Capability and Cyclability. *ACS Appl. Mater. Interfaces* **2015**, *7* (28), 15531–15541.

(20) Martinez-Garcia, A.; Thapa, A. K.; Dharmadasa, R.; Nguyen, T. Q.; Jasinski, J.; Druffel, T. L.; Sunkara, M. K. High Rate and Durable, Binder Free Anode Based on Silicon Loaded MoO_3 Nanoplatelets. *Sci. Rep.* **2015**, *5* (April), 10530 1-5.

(21) Liu, C.; Neale, Z. G.; Cao, G. Understanding Electrochemical Potentials of Cathode Materials in Rechargeable Batteries. *Mater. Today* **2016**, *19* (2), 109–123.

(22) Boukhalfa, S.; Evanoff, K.; Yushin, G. Atomic Layer Deposition of Vanadium Oxide on Carbon Nanotubes for High-Power Supercapacitor Electrodes. *Energy Environ. Sci.* **2012**, *5* (5), 6872–6879.

(23) Hassan, M. F.; Guo, Z. P.; Chen, Z.; Liu, H. K. Carbon-Coated MoO_3 Nanobelts as Anode Materials for Lithium-Ion Batteries. *J. Power Sources* **2010**, *195* (8), 2372–2376.

(24) Riley, L. a.; Lee, S. H.; Gedvilias, L.; Dillon, A. C. Optimization of MoO_3 Nanoparticles as Negative-Electrode Material in High-Energy Lithium Ion Batteries. *J. Power Sources* **2010**, *195* (2), 588–592.

(25) Tao, T.; Glushenkov, A. M.; Zhang, C.; Zhang, H.; Zhou, D.; Guo, Z.; Liu, H. K.; Chen, Q.; Hu, H.; Chen, Y. MoO_3 Nanoparticles Dispersed Uniformly in Carbon Matrix: A High Capacity Composite Anode for Li-Ion Batteries. *J. Mater. Chem.* **2011**, *21* (25), 9350–9355.

(26) Wang, Z. Y.; Madhavi, S.; Lou, X. W. Ultralong Alpha-MoO_3 Nanobelts: Synthesis and Effect of Binder Choice on Their Lithium Storage Properties. *J. Phys. Chem. C* **2012**, *116* (23), 12508–12513.

(27) Yuan, Z.; Si, L.; Wei, D.; Hu, L.; Zhu, Y.; Li, X.; Qian, Y. Vacuum Topotactic Conversion Route to Mesoporous Orthorhombic MoO_3 Nanowire Bundles with Enhanced Electrochemical Performance. *J. Phys. Chem. C* **2014**, *118* (10), 5091–5101.

(28) Ko, Y. N.; Park, S. Bin; Kang, Y. C. Excellent Electrochemical Properties of Yolk-Shell MoO3 Microspheres Formed by Combustion of Molybdenum Oxide-Carbon Composite Microspheres. *Chem. - An Asian J.* **2014**, *9* (4), 1011–1015.

(29) Yu, X.; Wang, L.; Liu, J.; Sun, X. Porous MoO_3 Film as a High-Performance Anode Material for Lithium-Ion Batteries. *ChemElectroChem* **2014**, *1* (9), 1476–1479.

(30) Huang, J.; Yan, J.; Li, J.; Cao, L.; Xu, Z.; Wu, J.; Zhou, L.; Luo, Y. Assembled-Sheets-like MoO3 Anodes with Excellent Electrochemical Performance in Li-Ion Battery. *J. Alloys Compd.* **2016**, *688*, 588–595.

Chapter 4

Development of Nitrogen Incorporated Molybdenum Oxide by Atomic Layer Deposition and Its Enhanced Electrochemical Activity

This chapter discusses the development of nitrogen-incorporated MoO_x films and their characterizations. How a better electrochemical performance is achieved by incorporating nitrogen is also discussed here.

Oxide materials are highly resistive in nature and that affect the performance of the device. It is previously observed that metal oxynitrides have shown better conductivity than their pure oxide form. For this reason, we tried to increase the conductivity of the MoO_x layer by incorporating nitrogen by the ALD method. Nitrogen incorporation is estimated and monitored by *in-situ* quartz crystal microbalance (QCM). A tunable electrical characteristic that varies monotonously with nitrogen incorporation is noticed. Enhanced conductivity in the nitrogen-incorporated films shows improved electrochemical performances when used as anode material in LIB.

4.1 Experimental

A modified ALD method is used to incorporate the host material. First, 'n' layers of the host material (here MoO_x) are deposited onto the substrate. This is followed by one layer of the guest material (here MoN_x) and additional n layers of the host material. The schematic of this process is given in Figure 4.1a. This cycle, called the 'supercycle', is iterated until the desired film thickness is achieved. After deposition, the guest elements diffuse throughout the film, and the host is thus doped. In this study, four types of doped samples are prepared using MoO_x and MoN_x where n= 9, 19, 39, and 59. Clean silicon wafers and soda lime glass are used as the substrate for all the film characterizations. In contrast, plain stainless steel (SS) and MWCNT-coated SS substrates are used for electrochemical characterization. Resistivity and temperature-dependent Hall measurements are performed with using van der Pauw geometry. The films are deposited on microscopic glass substrates measuring approximately 1 cm × 1 cm for Hall measurements.

4.2 Results and discussions

4.2.1 *In-situ* QCM study

As mentioned earlier, MoO_x is obtained from $Mo(CO)_6$ and O_3, and MoN_x is obtained from $Mo(CO)_6$ and NH_3 precursors. Changes in mass corresponding to the different precursor doses used for depositing nitrogen-doped molybdenum oxide are investigated using an *in-situ* QCM at 170 °C (Figure 4.1b). The Sauerbrey equation is used to convert the change in frequency to change in mass. A mass gain of approximately 38.7 ng cm^{-2} is observed after one $Mo(CO)_6$ dose. Subsequently, a mass gain of approximately 21.3 ng cm^{-2} is observed after one O_3 dose. The mass gain after an NH_3 dose is approximately 6.7 ng cm^{-2}, indicating the

incorporation of nitrogen into the film. The lower mass gain with NH_3 addition can be explained by the higher charge of the nitrogen atom (N^{-3}) than the oxygen atom (O^{-2}). A higher number of surface sites probably interact per NH_3 molecule adsorbed, thus reducing the number of reaction sites for the next precursor. The mass gain on the addition of the metal precursor after one NH_3 dose tended to be lower than the previous amount. However, the mass gain after another cycle of MoO_x addition is comparable to the first cycle gain.

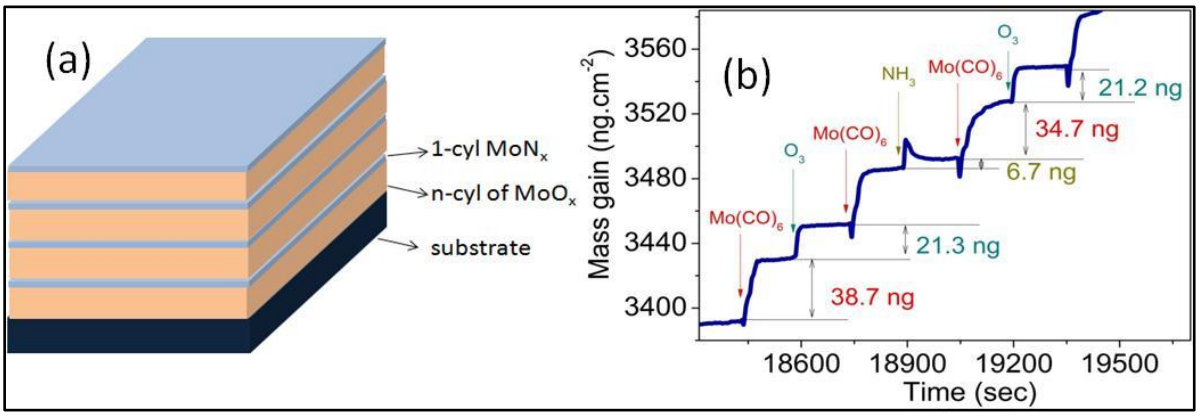


Figure 4.1 (a) A schematic of the film stack used for growing different compositions of nitrogen-doped MoO_x films by ALD. (b) In-situ QCM results showing mass gain after various doses of precursor deposition at 170 °C.

4.2.2 Secondary ion mass spectrometry (SIMS) and energy diffractive area X-ray (EDAX) elemental mapping

Figure 4.2a shows the SIMS spectra of the nitrogen-doped molybdenum oxide film (where one layer of MoN_x is sandwiched between nine MoO_x layers (i.e., 9:1), deposited over a silicon substrate. A silicon substrate is chosen as it allows the easy and clear location of the film and interface. Elemental profiles of Mo, O, N, and Si are obtained. The presence of nitrogen is confirmed throughout the film along with Mo and O, thereby indicating successful doping of nitrogen in the MoO_x. The relative concentration of O and Mo is much higher than that of N; the amount of the three elements sharply reduced at the film–substrate interface, beyond which the Si content increased. The presence of nitrogen is further verified by TEM EDAX elemental mapping (Figure 4.2b). For this analysis, the as-deposited film is scraped from the substrate using a sharp blade and the shavings are thoroughly dissolved in acetone. Subsequently, this solution is dropped over the TEM grid and dried.TEM analysis showed that although the N concentration is very low, it is present throughout the film along with Mo and O.

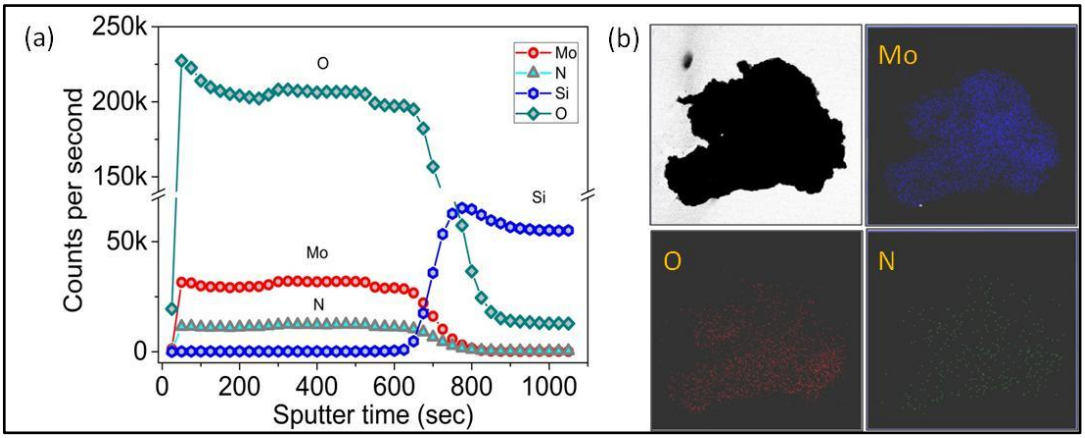


Figure 4.2 (a) TOF-SIMS spectra of MoOx:N (9:1) film deposited on Si substrate showing Mo, O, N, and Si elemental count profiles; (b) EDAX elemental mapping of Mo, O, and N atoms in the MoOx:N film

4.2.3 X-ray photoelectron spectroscopy (XPS)

XPS is performed to analyze the electronic states of the elements (especially Mo) in the films. Figure 4.3a shows the XPS spectra of Mo 3d region in the MoO_x, MoO_x:N and MoN_x films. The peaks at 232.2 and 235.34 eV correspond to the binding energy (BE) of Mo $3d_{5/2}$ and $3d_{3/2}$ electrons of the Mo^{+6} valency state in the undoped MoO_x film.[1,2] Interestingly, the Mo peaks shifted slightly to a lower BE when nitrogen is introduced in the MoO_x lattice. BE further decreases in MoN_x film (232.09/235.21 eV and 232.02/235.14 eV for MoO_x:N (9:1) and MoN_x samples). This is possibly due to the decrease in the ionic nature of Mo–O bond on account of nitrogen substitution, as the electronegativity of nitrogen is lower than that of oxygen. However, nitrogen incorporation did not result in a sharp reduction in Mo peaks. Most previous studies reported an unavoidable reduction of Mo atoms to Mo^{+4} during nitridation or ammonolization of MoO_3.[3,4] The oxygen 1s BE peak is observed at 530.9 eV. Although the presence of nitrogen in the film is confirmed, the exact percentage of atomic nitrogen could not be calculated because the N1s peak overlapped with the Mo3p peak.

4.2.4 Raman spectra

Raman spectroscopy confirmed the presence of both Mo–O and Mo–N bonds in the doped films (Figure 4.3b). All the spectra are measured using a 514.5nm laser with 10mW power. Major vibration peaks from the MoO_x film deposited on the silicon substrate are observed at 112, 125,147, 171,194, 211, 234, 280, 285, 334, 367, 375, 422, 447, 662, 783, 818, 894, 900, and 993 cm^{-1}. The MoN_x film produced vibration peaks at 103, 126,140, 175, 197, 223, 270, 301, 343, 372, 420, 443, 620, 789, 830, 906, 943, and 975 cm^{-1}. Peaks in the region of 100–

600 cm^{-1} may be attributable to deformation vibrations (such as rocking, wagging, and twisting), whereas peaks in the range of 600–1000 cm^{-1} may have resulted from symmetric and asymmetric stretching vibrations of Mo–X (where X= O or N). As observed in MoO_x, the nitride film also showed different types of Mo–N bonds (e.g., Mo=N, Mo–N, Mo–N2, Mo–N3).[5–7] The N-doped film showed all the stretching vibrations of Mo–O from MoO_x and Mo–N from MoN_x.

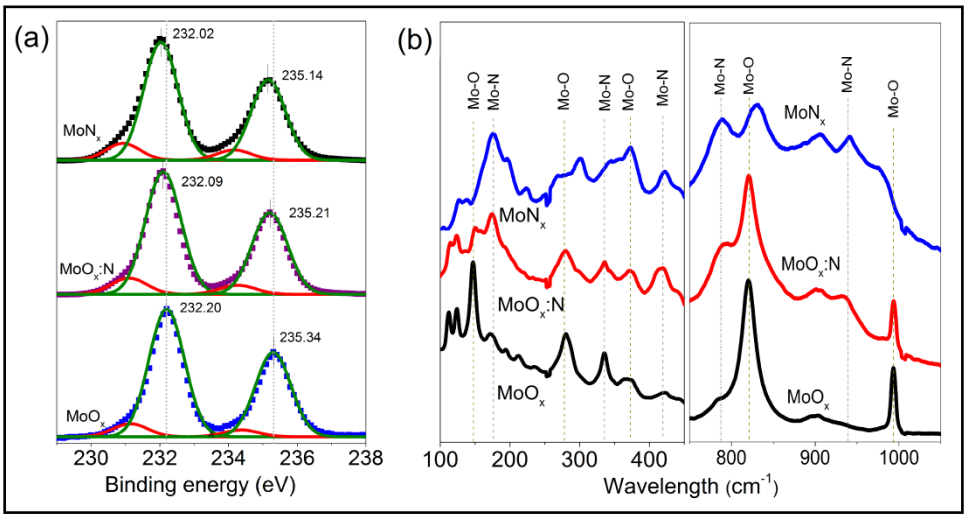


Figure 4.3 (a) XPS profile of Mo 3d in and (b) Raman spectra of MoO_x, N-incorporated MoO_x and MoN_x films

4.2.5 Ultraviolet photoelectron spectroscopy (UPS)

UPS spectra of different nitrogen incorporated MoO_x films are done to understand the change in band positions and Fermi level (E_f) position due to nitrogen addition. In UPS measurement, E_f of all the samples is normalized to zero, because the detector and samples are electrically grounded during the measurements. Figure 4.4b demonstrated the full survey and Figure 4.4 (a & c) spectra attributed the closer look of the secondary electron cut-off at higher energy region from where the work function (WF) of materials can be calculated. WF of material defines by the energy difference between vacuum level and E_f. MoO_x film showed lowest secondary electron cut-off value at 15.64 eV and highest WF value of 21.2-15.64 = 5.56 eV. MoO_3 is widely used as hole scavenger or charge transfer buffer layer in photovoltaics because of its high WF and the deep-lying conduction band. The value of WF continuously shifted to a lower value with increasing N-inclusion in the films. Thus, the addition of nitrogen led to an increase in the accumulation of the carrier at the bottom of the conduction band (CB). The lowest WF value is found to be 5.28 eV for MoN_x film. Figure 4.4a displayed the magnified view of the valence band (VB) onset for all the films. VB onset is calculated

from the intersection point of the tangent of VB leading edge and E_f. The position of the edge of VB maxima found to be 2.49 and 2.61 eV below of E_f for MoO_x and MoN_x films respectively. The schematic of the details band structure and alignment is given in Figure 4.4d. Interestingly, there are many deep level gap states can be found at the MoO_x VB onset which does not take part in the conduction process. Addition of nitrogen in the system reduced those states.

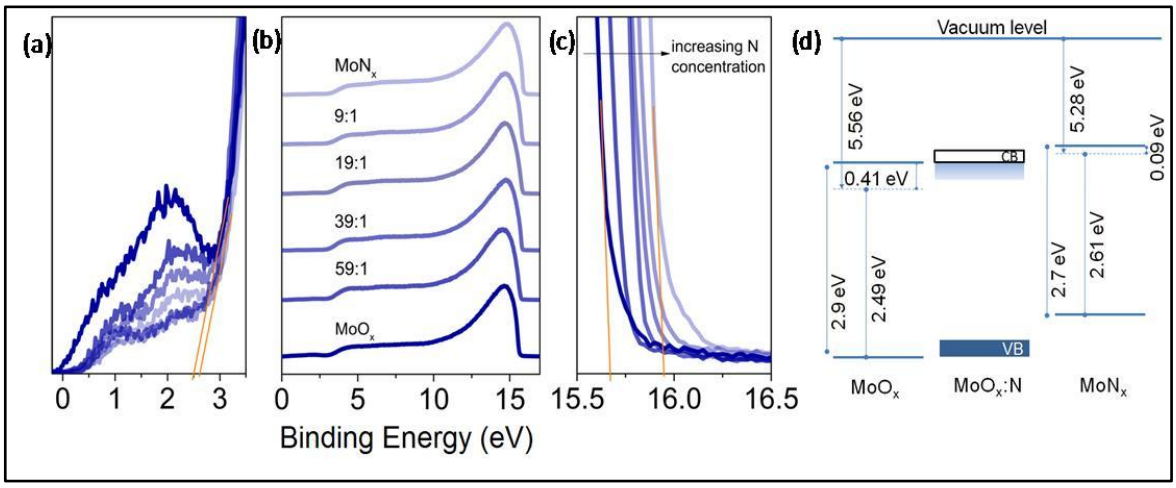


Figure 4.4 UPS spectra of different nitrogen incorporated MoOx films plotted with respect to Fermi level- (a) Magnified view of valence band onset, (b) full spectrum, (c) close view of secondary electron cut-off and (d) schematic of tentative energy level alignment diagram

4.3 Electrical Characterization

The mechanism underlying electron doping in the N-incorporated MoO_x films is believed to be the formation of oxygen vacancies, which serve as shallow donors. The role of oxygen vacancies in the ionic transport of MoO_x:N films have been investigated by several works through high-temperature transport measurement, which also takes into account oxygen vacancy migration. Figure 4.5 shows the variation in room-temperature electrical resistivity and carrier concentration of as-deposited MoOx:N films as a function of the NH_3 cycle percentage, given by $R_{NH3}\,(\%) = 1/(1+n) \times 100\ \%$. The as-deposited MoO_x films show high resistivity at ~374 Ω-cm. The N-doped films have markedly lower resistivity, with the minimum value in the range of 2.3 Ω-cm for 50% R_{NH3}. Films with R_{NH3} ranging 0–2.5% did not exhibit reproducible Hall voltage, probably because of the extremely low carrier mobility, which renders the films highly resistive. Therefore, the carrier concentration values of these films are not included in Figure 4.5.

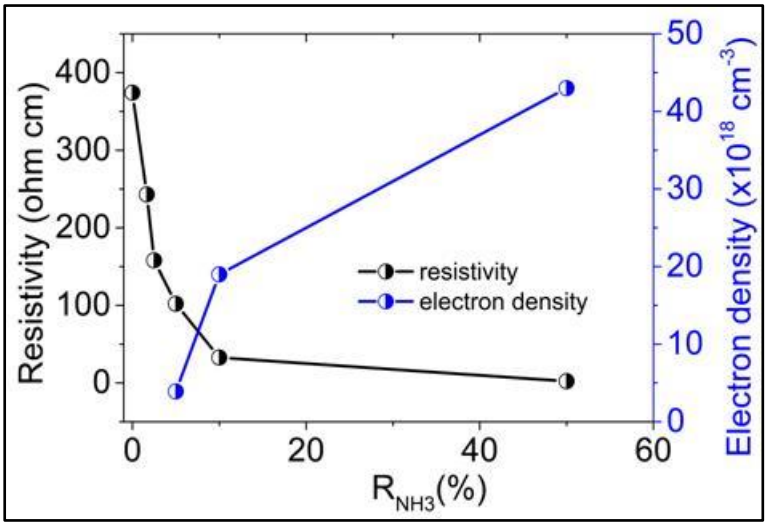


Figure 4.5 Room-temperature resistivity and electron density as a function of R_{NH3}

Films with R_{NH3}rangingfrom 5% to 50% showed low resistivity because of the increase in the carrier density from 4.0×10^{18} to 4.3×10^{19} cm^{-3}. The Hall mobility values for these films rangedbetween0.01 and 0.06 $cm^2\ V^{-1}\ s^{-1}$. This comparatively poor carrier mobility is probably due to the structurally disordered nature of the amorphous films. To confirm the carrier type in such highly disordered semiconductors, Seebeck effect measurements are determined. The Seebeck coefficient ($S=dV/dT$) thus obtained is negative, which implied an n-type nature of the as-grown MoO_x:N films (Figure 4.6).

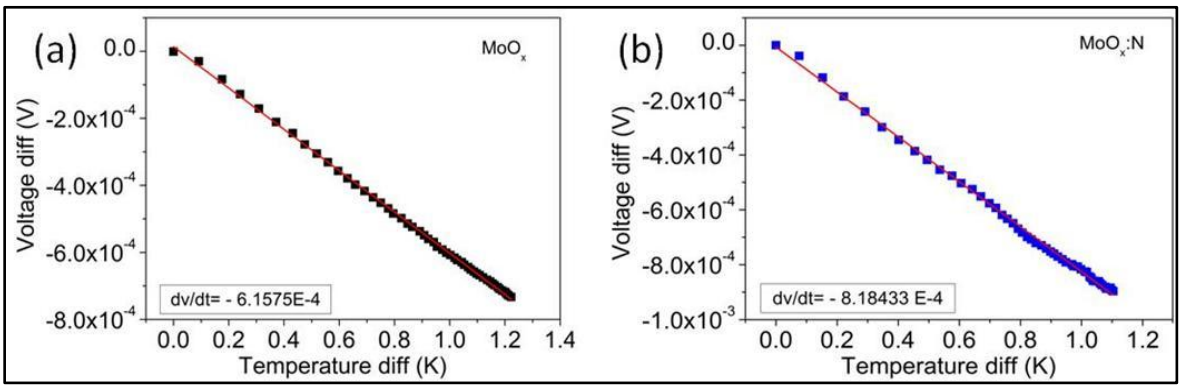


Figure 4.6 Variation in thermal emf (dV in Volts) with temperature difference (dT in K) between hot and cold probes for (a) a pristine and (b) N-incorporated films.

To explore the underlying electronic transport processes in the N-incorporated films grown by ALD, electrical resistivity measurements are performed at a temperature range of 10–300 K. The results are shown in Figure 4.7a.

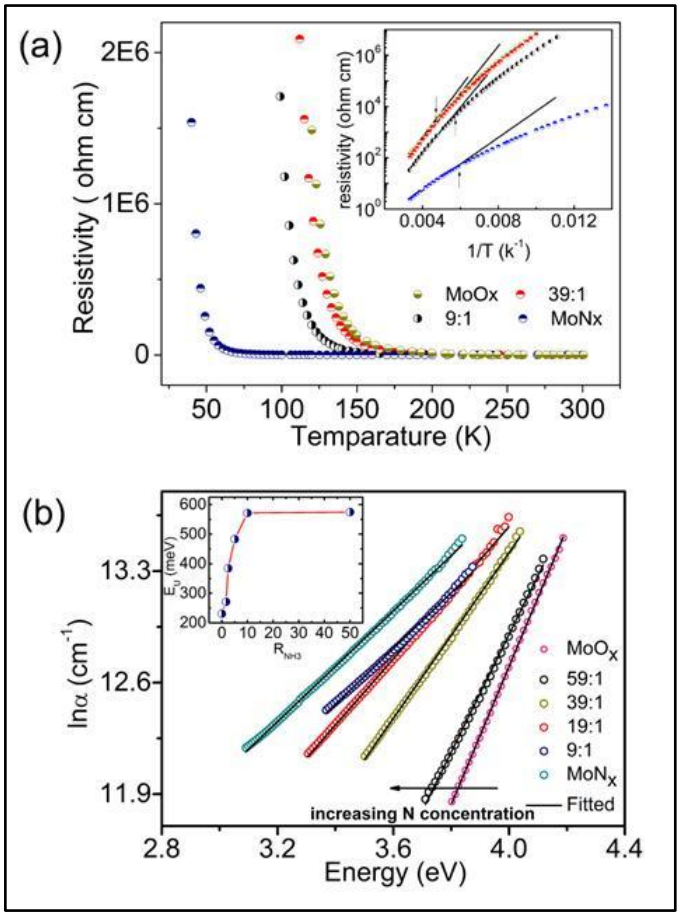


Figure 4.7 (a) Temperature-dependent resistivity curves for different MoO_x:N samples. The inset shows resistivity plots to extract the activation energy in a high-temperature regime. Vertical arrows indicate the temperature at which the $\rho(T)$ curve deviates from the activation behavior, (b) Variation in sub-bandgap absorption ($h\nu<E_g$) for different N-incorporated samples. The solid line indicates the measured data fitted according to the Urbach equation. The inset shows the extracted Urbach energy values as a function of R_{NH3}.

The resistivity values for all the films, including the highest conducting MoN_x, exhibited strong temperature dependence. The relative resistivity ratio [$\rho_r = \rho(T_{min}/ 300)$] varied from 4×10^3 to 6.6×10^5, where T_{min} is the minimum temperature up to which resistivity is measured. Moreover, all the films showed diverging resistivity behavior on extrapolation to T $\rightarrow$ 0 K, implying that all films are in the insulating regime of the metal-to-insulator transition.

Spatial fluctuation in the potential of these amorphous semiconductors is the result of a pronounced static disorder caused by the combined effect of positional and energetic disorders in the films. The positional disorder originates from the statistical distribution of nitrogen impurities of equal potential strength. In contrast, the energetic disorder in the films is due to the randomness of the potential energy levels at different lattice sites. Such disorders

in the films result in the distribution of localized electronic states within the band gap, thereby forming band tails, which are also known as Urbach tails. Hence, even below the fundamental bandgap, these semiconductors exhibit significant optical absorption in the sub-bandgap regime (Figure 4.8).

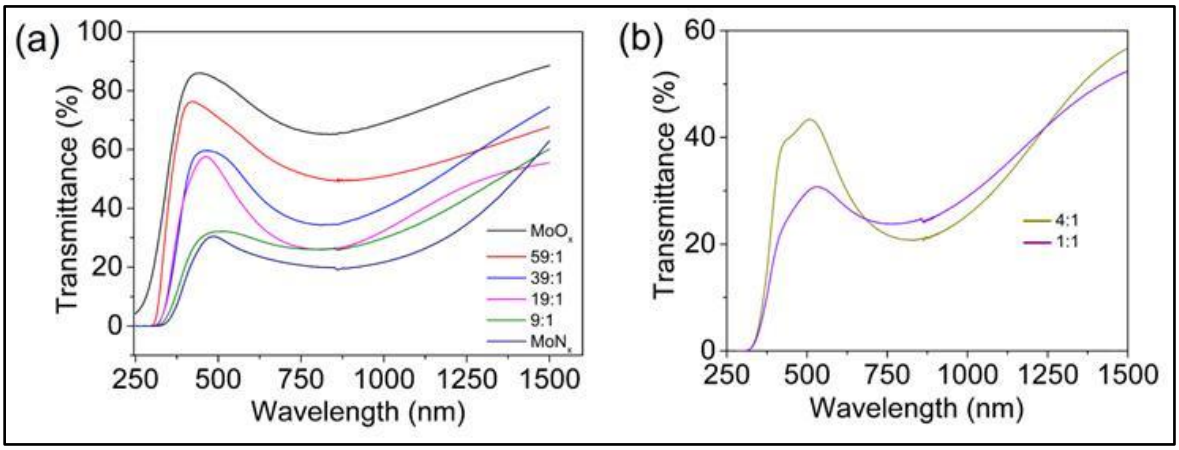


Figure 4.8 Optical transmittance spectra of all N-incorporated films grown on quartz substrates

For incident photon energy $h\nu<E_g$, the optical absorption can be mathematically represented as $\alpha = \alpha_0 \exp(h\nu - E_1/E_U)$, where α_0 and E_1 are constants and E_U is the Urbach energy (Figure 4.7b). Here, with the incorporation of 'N' in the MoOx lattice (see inset), E_U increases from 230 meV (MoO_x) to 574 meV (MoN_x). This increase indicates the increasing strength of the static disorder in the films.

The high degree of disorder is also evident from the poor Hall mobility (0.01–0.04 cm^2/Vs) and the extremely short electron mean free path values (0.001–0.04 Å), given by $= h/\rho n e^2 \lambda_F$, where ρ is the room-temperature resistivity, n is the electron density, and $\lambda_F = 2\pi/(3\pi^2 n)^{1/3}$ is the Fermi wavelength. These values are considerably smaller than the inter-atomic separation. Therefore, it is likely that charge carriers are strongly localized or self-trapped within the impurity potentials, resulting in the Anderson localized insulating state. Thus, the charge transport at relatively higher temperatures may occur through activated carriers in the extended states. This mechanism for electronic conduction influences the temperature dependence of the resistivity, which can be represented as $\rho(T) = \rho_0 \exp(\Delta E/kT)$, where $\Delta E = E_c - E_F$ is the carrier activation energy. In case of n-type amorphous semiconductors, ΔE is represented by the separation of the Fermi level E_F from the mobility edge E_c. Activated electronic transport (see inset of Figure 4.7a) in the high-temperature range can be determined

by the $\rho(T)$ characteristics, *i.e.*, the activation energy varies in the range 100−206 meV. High ΔE values for the films with R_{NH3}ranging 0–2.5% might have resulted in sparse electron density above the mobility edge to produce a sizable Hall voltage. Consequently, the extraction of the carrier concentration in these films using Hall measurement is difficult. The $\rho(T)$ curves show a clear deviation from the above mentioned activated transport behavior in the low-temperature regime (see inset of Figure 4.7a). This can be attributed to the dominance of the hopping conduction process using localized states below the mobility edge. In the low-temperature regime, the resistivity curves can be explained by considering the hopping conduction process in the Mott variable range (Figure 4.9), which is mathematically represented as $\rho(T) = \rho_M \exp(T_{min}/T)^{1/4}$.

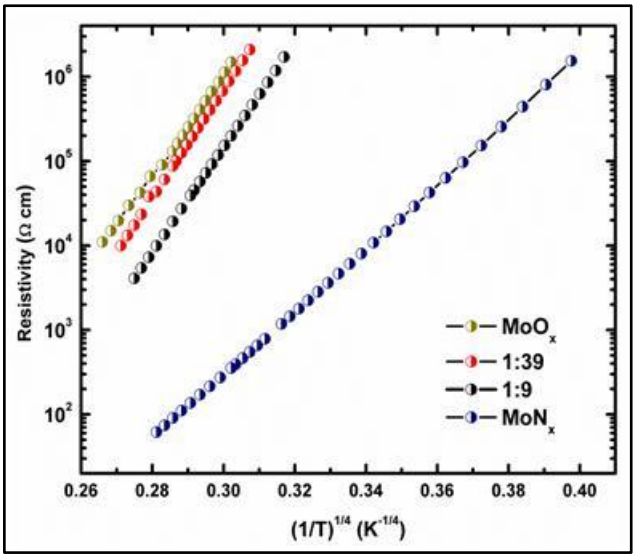


Figure 4.9 Variation of lnρ as a function of $(1/T)^{1/4}$. The linear behavior implies the dominance of Mott variable range hopping conduction in the low-temperature range.

4.4 Electrochemical characterization

Electrical measurements evidently showed that nitrogen incorporation results increase in conductivity, now the electrochemical performance of N-incorporated MoO_x samples is also being evaluated along with the pristine MoO_x and MoN_x against Li/Li^+ system. For comparison, nitrogen incorporated sample with R_{NH3}=10% (*i.e.* 9:1) is taken with other samples and approximately 100 nm thick films are grown directly on SS substrates for all the cases.

Cyclic voltammetry (CV) of bare MoO_x, MoN_x, and MoO_x:N electrodes in the first cycle are shown in Figure 4.10a. There are not many differences can be found in the plot among three

samples. Reduction peaks are obtained at 0.15 V, 0.33 V and above 2 V during the first cathodic sweep and four oxidation peaks at 0.45, 1.26, 1.8 and 2.5 V are observed during the first delithiation when cycled within 3.0 V to 0.01 V against Li/Li^+ in case of MoO_x:N film. Two distinguished peaks at lower potentials are seen for all the samples could be assigned to the conversion reaction between MoO_x and Li^+ ion to form Mo metal and Li_2O ($MoO_x + xe^- + xLi^+ \rightarrow Mo + Li_2O$).[8] The peak at 0.45 V represents the reaction initiation between Mo and Li_2O whereas peaks at 1.26 V and 1.8 V are originated probably due to multistep Li-extraction. The peak popped at 2.5 V during the anodic scan which weakens upon cycling, could be assigned as the delithiation reaction from unconverted Li_yMoO_x(N) phase. After the first cycle, electrode undergoes a sharp change in the chemical environment and as a result, a new and stable intercalation peak at 1.6 V is observed in the consecutive cycles during the discharge process. Similar observations are also found in previous reports.[9,8,10–12] Other than a little shift in peak positions bare MoO_x film showed almost similar kind of CV profile as that of MoO_x:N except in the conversion region where the peak intensity is comparatively higher than MoO_x but similar to MoN_x. Addition of N perhaps alleviates spirited charge dynamics in the system. Pure MoN_x also showed similar kind of CV with no extra peak appearing into the profile. During the first cathodic process, three distinct peaks are observed at 1.0, 0.39, and 0.15 V vs. Li/Li^+. The origin of the peak at 1.0 V could be Li^+ intercalation into the bulk of the material. A new peak appeared at 1.39 V after the first cycle (Figure 4.11b). Another very interesting fact that the peak positions remained almost same from second cycle onwards in case of MoO_x (Figure 4.11a) and MoO_x:N (Figure 4.10b) films but a continuous peak shift with cycling is observed in MoN_x sample. It means that the electrode experiences a continuous chemical change after every cycle of lithiation-delithiation. In the anodic scan, it is presumed that the delithiation process occurred via two-step reactions that are observed at 1.43 and 1.83 V.

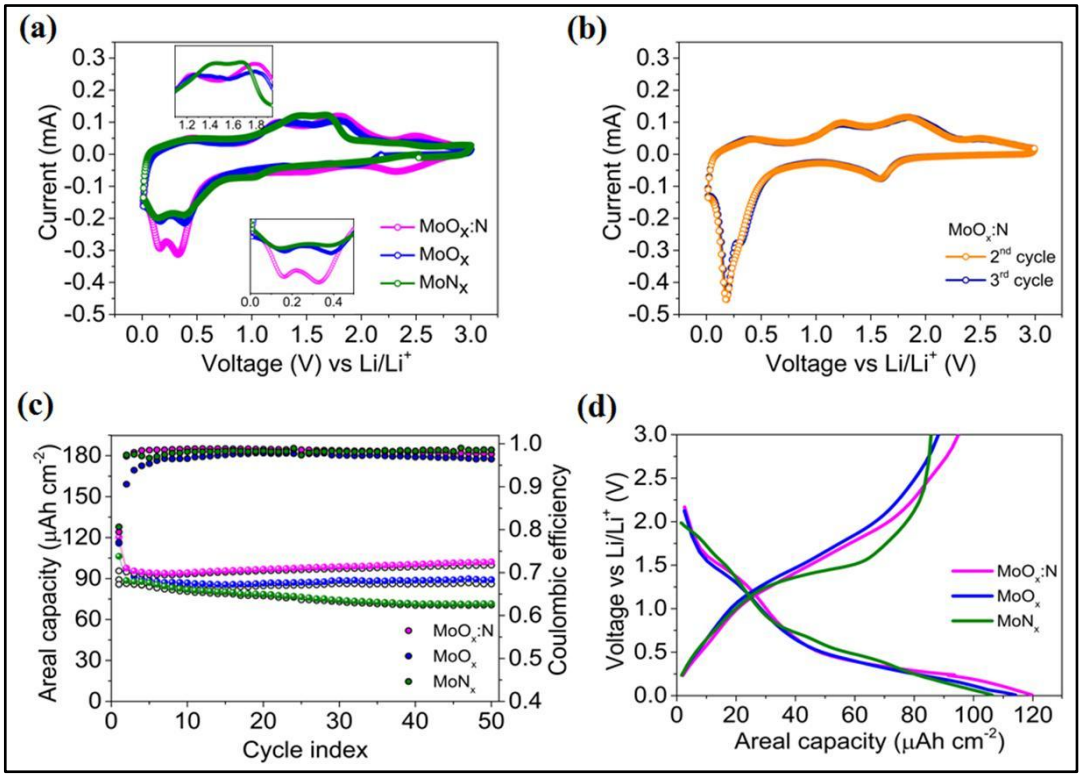


Figure 4.10 (a) CV of a N-incorporated MoOx, bare MoOx and MoNx films in the first cycle and (b) CV of a MoOx:N electrode in 2nd and 3rd cycle, (c) charge-discharge capacities, Coulombic efficiency and (d) 1st cycle lithiation-delithiation voltage profiles of different electrodes vs Li/Li+.

Charge-discharge performances of three different electrodes are studied in the range of 0-3 V vs Li/Li^+ at a constant current rate of 50 μA cm^{-2} (Figure 4.10c). MoN_x films showed better performance among all initially. Areal capacities of 120, 115, 131 μA cm^{-2} and 95, 89, 105 μA cm^{-2} are obtained at the end of the first discharge and charge process from the MoO_x:N, MoO_x and MoN_x films deposited on SS coin respectively. In the 50^{th} charge-discharge cycles, the capacity value found to be 102, 89, 88 and 99, 86, 87 μA cm^{-2} respectively for discharge and charge processes. Although MoO_x and MoO_x:N films showed stable capacity up to 50 cycles, a continuous capacity fading is noticed in case of MoN_x sample. It is expected that MoN_x would show better electrochemical activity towards Li/Li^+ because of its highest conductivity among three electrodes. But, as discussed earlier, a continuous change in the chemical environment after each charge-discharge cycle could be the main reason behind this capacity decay. Figure 4.10d is showing the galvanostatic lithiation-delithiation profile (voltage *vs* capacity) of all the three electrodes in the first cycle. Plateaus obtained during charge-discharge reactions are in good agreement with the CV profiles.

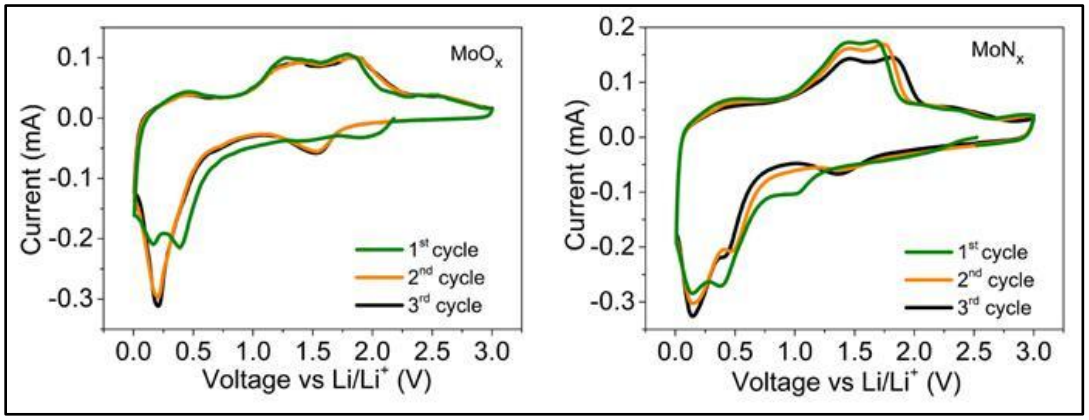


Figure 4.11: Cyclic voltammogram of (a) MoOx, and (b) MoNx in the 1st, 2nd and 3rd cycle

Next generation LIBs need high power density along with higher energy density. Nanostructured materials with high surface area remain a high hope for high-performance LIBs. 3D structures always have the added advantage in terms of withstanding volume changes, shorter Li diffusion path etc. to increase the performance of electrodes. To have the advantages, MoO_x (or MoO_x:N) coated MWCNT 3D core-shell nanostructures are prepared for the better charge-discharge performance and stability of both the electrodes. Pre-treated MWCNTs are uniformly deposited on SS substrates by simple drop cast method from an aqueous colloidal solution. High surface area and highly conducting MWCNTs served as template layer to anchor the active oxide layer. Then, MWCNT coated substrates are placed inside the reactor and deposited 300 saturated ALD cycles of MoO_x (or MoO_x:N). Figure 4.12a shows the schematic representation of the active layer coating on the CNT layer. Mass of the active materials deposited after the reaction is measured with a microbalance with microgram precision. Uniform and conformal coating of an active oxide layer on CNTs can be seen from the SEM images in Figure 4.12b. No uncoated area is found throughout the films. HRTEM images (Figure 4.12c) confronted that the thickness of the active layer found to be approximately 20 nm on MWCNT surface.

Now, Charge-discharge performances of 3D core-shell CNT/MoO_x (and MoO_x:N) electrodes are studied in a potential range of 3-0 V vs. Li/Li$^+$ at the different current rate. Figure 4.12d shows the rate capabilities of two different electrodes with different current densities. Five charge-discharge cycles are carried out at each current density to ensure the stability of the electrodes. It clearly showed the superior performance of nitrogen incorporated electrodes than its pristine counterpart. A total of approximately 91.78 %, 83.67 %, 75.15 % and 66.01 % of initial capacities are retained for the current densities of 200, 500, 1000, 2000 mA g^{-1}

respectively for nitrogen incorporated samples. Whereas, pristine samples showed the capacity retention of 91.63 %, 83.48 %, 72.28 %, 60.85 % respectively for the same current densities. Capacity values of both the electrodes at a different rate are given in table-1. Good stability and rate capability are observed from both the samples at lower current because of the conducting 3D core-shell structure but at higher current densities nitrogen incorporated sample outperform the pristine electrode. Nitrogen incorporation definitely helped better charge transport during lithiation-delithiation processes.[3,13,14] A detail performance comparison between CNT/MoO_x and CNT/MoO_x:N electrodes are given in Table 4-1.

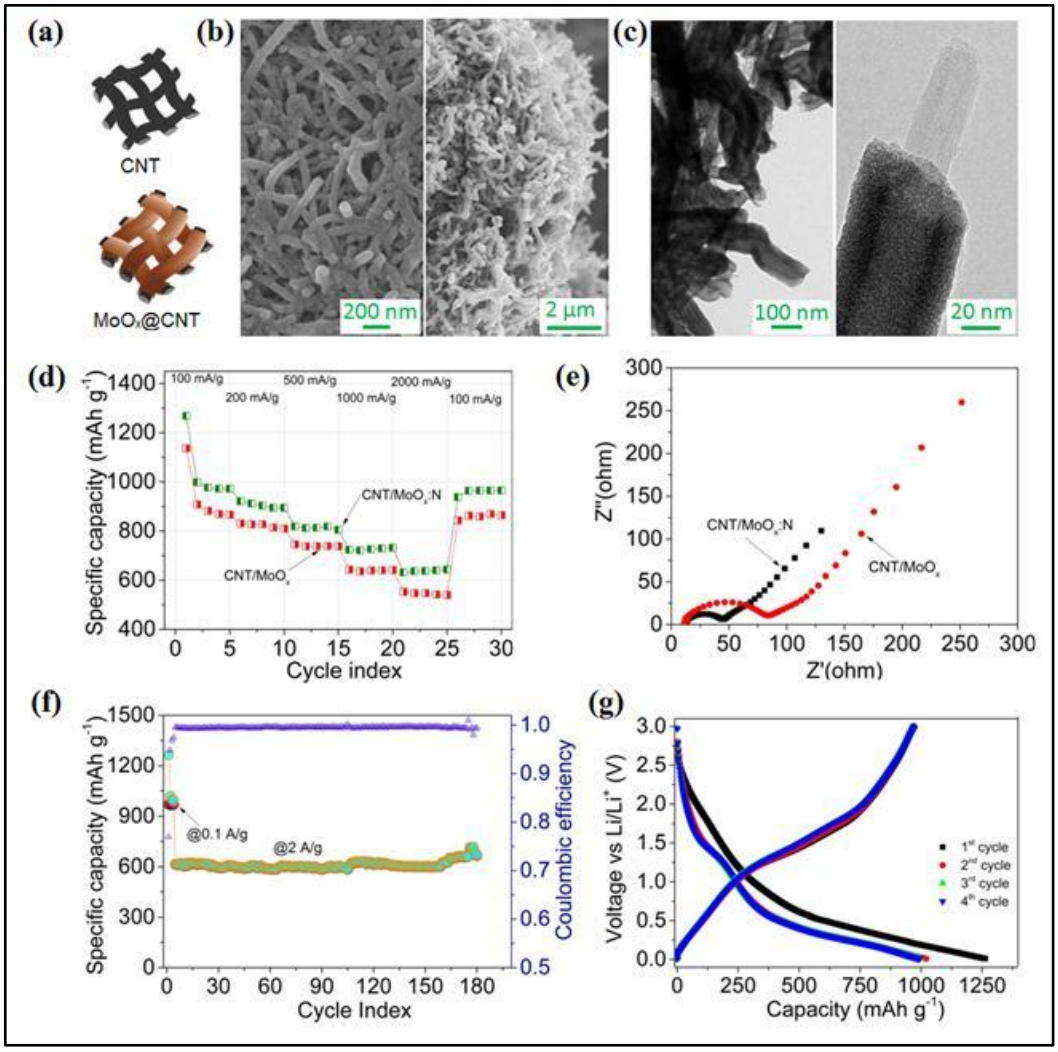


Figure 4.12 (a) Schematic representation of CNT and MoO_x@CNT structure, (b) SEM images of CNTs after MoOx (or MoOx:N) coating, (d) rate performance of CNT/MoOx and CNT/MoOx:N electrodes at different current rate and (e) electrochemical impedance spectra of CNT/MoOx and CNT/MoOx:N at OCP, (f) galvanostatic charge-discharge cycling and Coulombic efficiency of CNT/MoO_x:N electrode, (d) Charge-discharge profiles of CNT/MoOx:N electrodes for few initial cycles at 0.1 A g^{-1}.

In order to compare and understand the influence of nitrogen inclusion in MoO_x matrix profoundly, the electrochemical impedance spectra (EIS) measurements, which can accurately reflect the material's electrochemical characters, are carried out in the frequency range from 0.1Hz to 100 kHz in both electrodes at open circuit potential (OCP). The Nyquist plot of both the samples showed in Figure 4.12e. These EIS patterns consisted of a semicircle at a medium frequency which can be referred as the charge transfer resistance (R_{ct}) and then a suppressed semicircle which could be due to the solid electrolyte formation on electrode interface or because of any other interface formation probably with MWCNT. At low-frequency range the straight line in referred to the Li-ion diffusion in the film which can be denoted as Warburg impedance (W). The R_{ct} value for pristine MoO_x electrode is 73.71 ohm whereas the value is 33.19 ohm for N-incorporated electrode. Therefore, based on the R_{ct} values in it can be concluded that the MoO_x layer becomes more conducting after nitrogen addition, which is also reflected by the rate performances of both the electrodes.

Table 4-1 electrochemical performance comparison of CNT/ MoO_x:N amd CNT/MoO_x electrodes

Current density (mA g^{-1})	CNT/MoO_x:N electrode		CNT/MoO_x electrode	
	Capacity (mAh g^{-1})	Retention (%)	Capacity (mAh g^{-1})	Retention (%)
100	974	--	884	--
200	894	91.78	810	91.63
500	813	83.67	738	83.48
1000	732	75.15	639	72.28
2000	643	66.01	538	60.85
100	964	98.97	866	97.96

Figure 4.12f showing the galvanostatic charge-discharge stability of an MWCNT/MoO_x:N electrode. The cell is tested at a current density of 0.1 A g^{-1} for initial four cycles and then 2 A g^{-1} for the rest. The discharge capacity of 1287 mAh g^{-1} and 1026 mAh g^{-1} is observed in the first and second cycle. An average of 610 mAh/g stable discharge capacity at 2 A g^{-1} current density is obtained during charge-discharge cycling. High Coulombic efficiency of >98% is observed throughout the cycling. The plateaus and curves obtained from the charge-discharge profile showed in Figure 4.12g are in good agreement with the CV curves.

The increase in conductivity due to N-impurities thought to be due to the formation of oxygen vacancies which in turn increases the oxygen ion conductivity as well inside the lattice.[15] Wang et al. used a galvanostatic intermittent titration technique (GITT) to demonstrate the improved Li-ion conductivity when N-atoms are incorporated into the MoO_3 lattice.[14] In our case, the addition of N-atom creates random static disorder in the films which form band tails as a result act shallow donor level. As explained earlier, electron transfer in this kind of materials is facilitated by the activated carriers in the extended shallow states. Along with all this, the formation of conducting Li_3N species after conversion reaction should help to have good capability retention.

4.5 Conclusion

N-incorporated MoO_x films are obtained successfully by stacking of ALD MoO_x and MoN_x layers. Results obtained from SIMS, EDX mapping proved that the nitrogen atoms are diffused throughout the films and it formed a homogeneous doped material. The conductivity of the samples increases with nitrogen percentage. The highest carrier concentration of $4.3x10^{19}$ cm^{-3} is achieved from 100 nm thick films with R_{NH3}=10%. Temperature-dependent Hall measurements showed a highly static disorder system confirmed by poor hall mobility. Electrochemical characterizations are done for both pristine and N-incorporated samples. In comparison, higher conductivity of N-incorporated MoO_x samples helped in superior electrochemical performance. The highest discharge capacity of 1287 mAh g^{-1} is achieved in the first cycle at a current rate of 0.1 A g^{-1} and a stable capacity of 610 mAh g^{-1} when discharge at a high rate of 2 A g^{-1} from the CNT/MoO_x:N electrode. Table 4-2 shows the comparison of specific capacities and cyclic performance of different MoO_3 anode used recently in LIBs. In summary, this work showed how to incorporate nitrogen in oxides at relatively low temperature without reducing the materials and using them as high-performance 3D core-shell nanostructured LIB anode.

Table 4-2 Comparison of MoO_3 anodes used in Li-ion batteries by recent literature

Materials	Synthesis Method	Stable Capacity ($mAh\ g^{-1}$)	Current rate	Year	Ref.
Graphene–molybdenum oxynitride	Thermal decomposition	~960 ~385	100 mA g^{-1} 1600 mA g^{-1}	2013	13
α-MoO_3 nanowires	Vacuum topotactic transformation	~955	200 mA g^{-1}	2014	16
yolk-shell MoO_3-C microspheres	Spray pyrolysis	~896 ~534	500 mA g^{-1} 3000 mA g^{-1}	2014	17
Porous-MoO_3 film	Hydrothermal	~980 ~600	0.13C 2.7C	2014	18
$MoO_{2.31}N_{0.24}$	Partial nitridation	~980 ~180	50 mA g^{-1} 1000 mA g^{-1}	2014	3
HfO_2 coated MoO_3 nanorod	Hydrothermal	~740 ~630	1000 mA g^{-1} 1500 mA g^{-1}	2015	9
Assembled MoO_3 sheets	solvothermal	~889 ~567	0.1C 2C	2016	19
MoO_3 nanoflower	Sonochemical Synthesis	~1039 ~598	110 mA g^{-1} 2200 mA g^{-1}	2017	20
Carbon-coated MoO_3-NR	Grinding and heating	~897 ~542	100 mA g^{-1} 1000 mA g^{-1}	2017	21
Porous *h*-MoO_3@C nanofibers	Electrospinning	~946 ~271	100 mA g^{-1} 2000 mA g^{-1}	2017	22
N-incorporated MoO_x@MWCNT	ALD	~974 ~732 ~643	100 mA g^{-1} 1000 mA g^{-1} 2000 mA g^{-1}		This work

4.6 References

(1) Diskus, M.; Nilsen, O.; Fjellvåg, H. Growth of Thin Films of Molybdenum Oxide by Atomic Layer Deposition. *J. Mater. Chem.* **2011**, *21* (3), 705–710.

(2) Bertuch, A.; Sundaram, G.; Saly, M.; Moser, D.; Kanjolia, R. Atomic Layer Deposition of Molybdenum Oxide Using Bis(tert-Butylimido)bis(dimethylamido) Molybdenum. *J. Vac. Sci. Technol. A Vacuum, Surfaces, Film.* **2014**, *32* (1), 01A119 1-6.

(3) Ji, W.; Shen, R.; Yang, R.; Yu, G.; Guo, X.; Peng, L.; Ding, W. Partially Nitrided Molybdenum Trioxide with Promoted Performance as an Anode Material for Lithium-Ion Batteries. *J. Mater. Chem. A* **2014**, *2* (3), 699–704.

(4) Kühn, S.; Schmidt-Zhang, P.; Hahn, A. H.; Huber, M.; Lerch, M.; Ressler, T. Structure and Properties of Molybdenum Oxide Nitrides as Model Systems for Selective Oxidation Catalysts. *Chem. Cent. J.* **2011**, *5* (1), 42.

(5) Chen, D.; Liu, M.; Yin, L.; Li, T.; Yang, Z.; Li, X.; Fan, B.; Wang, H.; Zhang, R.; Li, Z.; et al. Single-Crystalline MoO_3 Nanoplates: Topochemical Synthesis and Enhanced Ethanol-Sensing Performance. *J. Mater. Chem.* **2011**, *21* (25), 9332–9342.

(6) Yang, Y.; Cao, Y.; Loo, B.; Yao, J. Microstructures of Electrochromic MoO_3 Thin Films Colored by Injection of Different Cations. *J. Phys. Chem. B* **1998**, *102* (47), 9392–9396.

(7) Ajito, K.; Nagahara, L. a.; Tryk, D. a.; Hashimoto, K.; Fujishima, a. Study of the Photochromic Properties of Amorphous MoO_3 Films Using Raman Microscopy. *J. Phys. Chem.* **1995**, *99* (44), 16383–16388.

(8) Lu, P.-J.; Lei, M.; Liu, J. Graphene Nanosheets Encapsulated α-MoO_3 Nanoribbons with Ultrahigh Lithium Ion Storage Properties. *CrystEngComm* **2014**, *16* (29), 6745–6755.

(9) Ahmed, B.; Shahid, M.; Nagaraju, D. H.; Anjum, D. H.; Hedhili, M. N.; Alshareef, H. N. Surface Passivation of MoO_3 Nanorods by Atomic Layer Deposition toward High Rate Durable Li Ion Battery Anodes. *ACS Appl. Mater. Interfaces* **2015**, *7* (24), 13154–13163.

(10) Liu, C.-L.; Wang, Y.; Zhang, C.; Li, X.-S.; Dong, W.-S. In Situ Synthesis of α-MoO_3/graphene Composites as Anode Materials for Lithium Ion Battery. *Mater. Chem. Phys.* **2014**, *143* (3), 1111–1118.

(11) Ma, F.; Yuan, A.; Xu, J.; Hu, P. Porous α-MoO_3/MWCNT Nanocomposite Synthesized

via a Surfactant-Assisted Solvothermal Route as a Lithium-Ion-Battery High-Capacity Anode Material with Excellent Rate Capability and Cyclability. *ACS Appl. Mater. Interfaces* **2015**, *7* (28), 15531–15541.

(12) Martinez-Garcia, A.; Thapa, A. K.; Dharmadasa, R.; Nguyen, T. Q.; Jasinski, J.; Druffel, T. L.; Sunkara, M. K. High Rate and Durable, Binder Free Anode Based on Silicon Loaded MoO_3 Nanoplatelets. *Sci. Rep.* **2015**, *5* (April), 10530 1-5.

(13) Zhou, D.; Wu, H.; Wei, Z.; Han, B.-H. Graphene-Molybdenum Oxynitride Porous Material with Improved Cyclic Stability and Rate Capability for Rechargeable Lithium Ion Batteries. *Phys. Chem. Chem. Phys.* **2013**, *15* (39), 16898–16906.

(14) Wang, X. J.; Nesper, R.; Villevieille, C.; Novák, P. Ammonolyzed MoO_3 Nanobelts as Novel Cathode Material of Rechargeable Li-Ion Batteries. *Adv. Energy Mater.* **2013**, *3* (5), 606–614.

(15) Yang, J. J.; Kobayashi, N. P.; Strachan, J. P.; Zhang, M. X.; Ohlberg, D. A. A.; Pickett, M. D.; Li, Z.; Medeiros-Ribeiro, G.; Williams, R. S. Dopant Control by Atomic Layer Deposition in Oxide Films for Memristive Switches. *Chem. Mater.* **2011**, *23* (2), 123–125.

(16) Yuan, Z.; Si, L.; Wei, D.; Hu, L.; Zhu, Y.; Li, X.; Qian, Y. Vacuum Topotactic Conversion Route to Mesoporous Orthorhombic MoO_3 Nanowire Bundles with Enhanced Electrochemical Performance. *J. Phys. Chem. C* **2014**, *118* (10), 5091–5101.

(17) Ko, Y. N.; Park, S. Bin; Kang, Y. C. Excellent Electrochemical Properties of Yolk-Shell MoO_3 Microspheres Formed by Combustion of Molybdenum Oxide-Carbon Composite Microspheres. *Chem. - An Asian J.* **2014**, *9* (4), 1011–1015.

(18) Yu, X.; Wang, L.; Liu, J.; Sun, X. Porous MoO3 Film as a High-Performance Anode Material for Lithium-Ion Batteries. *ChemElectroChem* **2014**, *1* (9), 1476–1479.

(19) Huang, J.; Yan, J.; Li, J.; Cao, L.; Xu, Z.; Wu, J.; Zhou, L.; Luo, Y. Assembled-Sheets-like MoO_3 Anodes with Excellent Electrochemical Performance in Li-Ion Battery. *J. Alloys Compd.* **2016**, *688*, 588–595.

(20) Yang, Q. D.; Xue, H. T.; Xia-Yang; Guan, Z.; Cheng, Y.; Tsang, S. W.; Lee, C. S. Low Temperature Sonochemical Synthesis of Morphology Variable MoO_3 Nanostructures for Performance Enhanced Lithium Ion Battery Applications. *Electrochim. Acta* **2015**, *185*, 83–89.

(21) Ding, J.; Abbas, S. A.; Hanmandlu, C.; Lin, L.; Lai, C. S.; Wang, P. C.; Li, L. J.; Chu,

C. W.; Chang, C. C. Facile Synthesis of carbon/MoO_3 nanocomposites as Stable Battery Anodes. *J. Power Sources* **2017**, *348*, 270–280.

(22) Chen, Z.; Liu, Y.; Zhang, H.; Ding, S.; Wang, T.; Zhang, M. In-Situ Phase Transition to Form Porous H-MoO_3@C Nanofibers with High Stability for Li^+/Na^+ Storage. *Sci. China Mater.* **2017**, *60* (8), 755–765.

Chapter 5

Cu-NW Template Based 3D Nanostructure Electrode for LIB

This chapter discusses the fabrication of 3D core-shell MoO_x/Cu nanostructure and their application as an anode in Li-ion battery. How the Cu-nw surface oxidation can be prevented during deposition is also discussed here.

Till now, it has seen observed that the use of CNT as scaffold or template layer for anchoring active material showed a promising approach for realizing high-performance electrodes with both high energy and power densities. These hierarchical nanostructure architectures have greatly influenced the stability and rate performance of the electrodes. However, the complexity and high cost involved in synthesizing CNT have hindered the mass production and thus commercial applications. Thus it is necessary to develop a simple and economical route for 3D nanostructure for practical application.

In this context, our approach is to replace the CNT template layer with an affordable and abandoned material which is 3D nanostructure of Cu. It has been used in most of the integrated circuit and printed circuit board because of superior conductivity. So, active material coated copper nanostructure would be a cost-effective solution for different energy storage devices.

Hybridizing high surface area nanostructured Cu-template with active material matrices to form similar kind of hierarchical structures has been realized to be an effective route to prevail over the above-mentioned issues. Taberna et al. successfully demonstrated two-step fabrication of core-shell structure consisting deposition of Cu-nw followed by Fe_2O_3 coating on them.[182] Those hybrid nanostructured electrodes showed excellent areal capacity and rate performance. Other materials, such as, Cu_2O,[183] GaN,[184] Si,[185] SnO_2,[186] CoO,[187] Bi,[188] Sn[189] and Ni_3Sn_4 [190] have also been successfully deposited onto Cu-nanostructure current collectors, which demonstrate the high-rate capability and longer cycle life.

In this chapter, electrochemical performance of 3D core-shell nanostructured obtained by ALD MoO_x coating on conducting Cu scaffold is showed towards Li/Li^+ system. ALD allows controlled and conformal active layer coating and Cu nanostructure provide conducting pathways for electron transportation. Such ALD coated 3D nanostructure can maintain the growing demand for energy storage for the future.

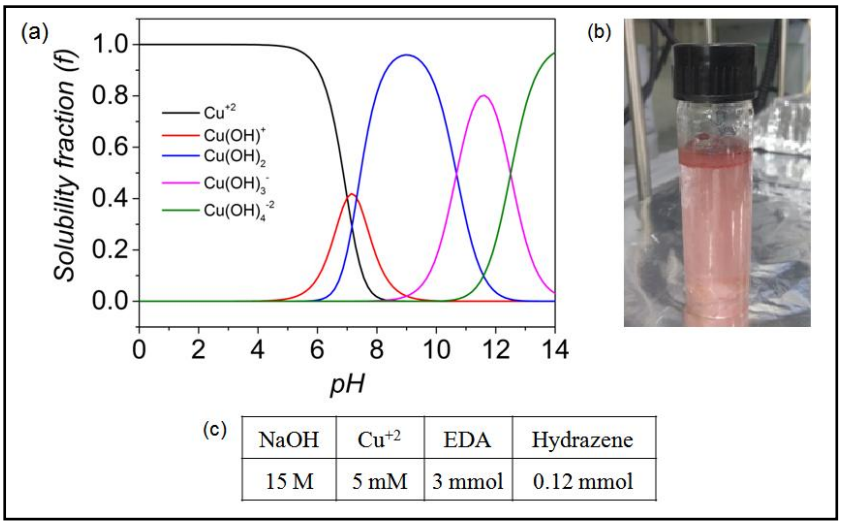
5.1 Results and discussions

5.1.1 Synthesis and characterization of Cu-nw and MoOx@Cu-nw structure

Copper nanostructures are synthesized by using the simple reduction of Cu^{+2} with hydrazine (Hz, N_2H_4) in a highly basic solution containing diethylamine (EDA) as a capping agent. The whole reaction is shown below-

$2Cu^{2+} + N_2H_4 + 4OH^- \rightarrow 2Cu + N_2 + 4H_2O$

Solubility graph of different Cu-species at different pH is plotted to understand the condition needed for the synthesis of Cu nanowire. All the values of solubility products and reaction constants are taken from Lange's Handbook of Chemistry at room temperature. It is found form the Figure 5.1a that a high pH>14 is required to avoid the formation of any Cu-hydroxide. Thus, all reaction is done at pH>14 for the synthesis of metallic Cu.



NaOH	Cu^{+2}	EDA	Hydrazene
15 M	5 mM	3 mmol	0.12 mmol

Figure 5.1 (a) Graph of fraction f of Zn(I1) existing as Cu^{2+}(aq), $Cu(OH)^{+}$(aq), $Cu(OH)_2$(aq), $Cu(OH)^{3-}$, and $Cu(OH)_4^{2-}$(aq) over a range of pH at 25 ^{0}C; (b) photograph of Cu-nw formed during reaction and (c) optimized bath condition for Cu-nw synthesis.

In a typical reaction 20 ml of 15 M NaOH, 1 ml of 0.1 M Cu^{+2} and 90 mM EDA are mixed at temperature 80 ^{0}C under stirring for 3 minutes. After that 0.12 mmol (7 µl) of hydrazine hydrate solution is added into the mixture and stirred for 2 minutes. The solution color changes from blue to colorless and colorless to red-brown indicating the formation of Cu is shown in Figure 5.1b. Optimized bath condition for Cu new synthesis is done by varying the concentrations of EDA, Hz, and Cu^{+2}. Figure 5.2 showing the SEM images of Cu-nws obtained from different bath conditions. The diameter of nanowires increases and length decreases with increasing the concentration of both EDA and Hz. HZ concentration below

0.12 mmol the reaction becomes very slow and yield is also very poor. Sharp difference is observed in terms of morphology when the concentration of Cu^{+2} increased from 5 mM to 10 mM or above. nano or micro-balls are formed when the concentration of Cu^{+2} is 20 mM or above (not shown here). The optimized condition for the Cu nw is given in Figure 5.1c. Cu nw with diameter 100 nm ± 30 nm and length with 12 ± 3 µm are obtained from the optimized bath.

As synthesized Cu-nws are dispersed in ethanol and uniformly deposited on SS substrates by simple drop-casting method. Then electrodes are prepared by depositing ALD MoO_x on to the Cu nw coated SS substrates. Weights of the electrodes are measured before and after the ALD coating.

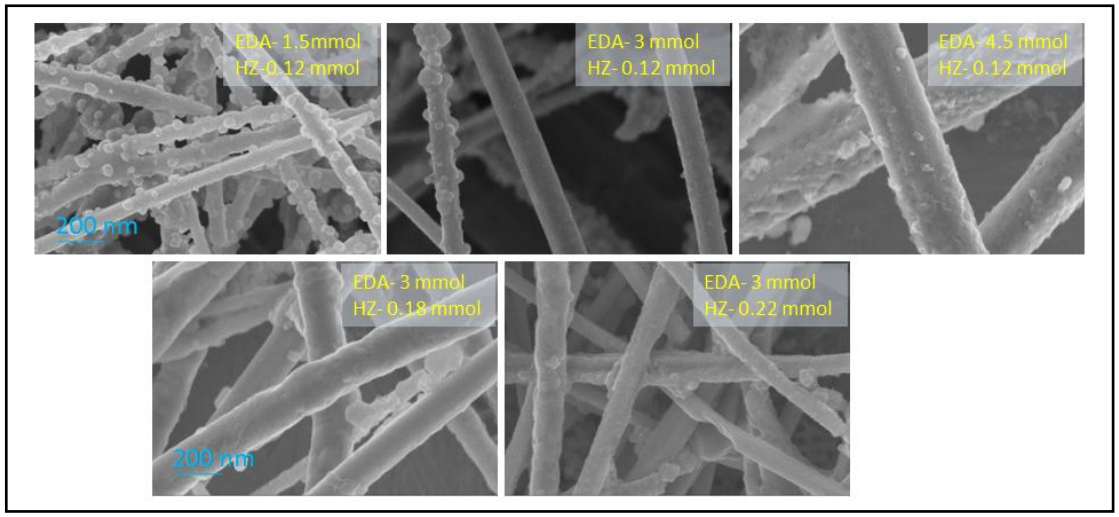


Figure 5.2 SEM images of Cu NWs obtained from different EDA and HZ concentration where other parameters are kept constant

SEM images of as prepared and ALD MoO_x coated Cu nw are shown in Figure 5.3(a-d). As prepared Cu nw layer produced an interconnected mesh network and MoO_x coating do not disturb contact points. Each and every Cu nw is coated uniformly, conformally by ALD coating. No uncoated Cu nw can be found in the images. The porosity of MoO_x/Cu electrode is expected to be good enough for effective interaction with electrolyte.

Figure 5.3e showing the XRD of 300 ALD cycled MoO_x coated Cu-nw electrode. It is observed that the Cu-nws partially got oxidized and formed unwanted surface Cu_2O after deposition of MoO_x layer. This is due to the involvement of ozone during the ALD process.

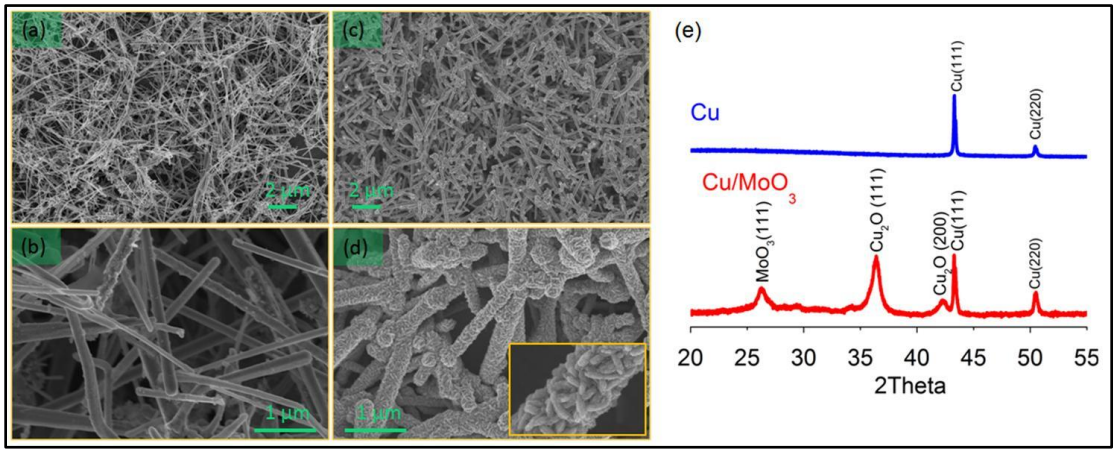


Figure 5.3 SEM images of (a,b) as synthesized Cu nw, (c,d) ALD MoO_x coated Cu nw and (e) XRD of as-prepared Cu-nw and 300 cycles MoO_x coated Cu-nw

As deposited oxide layer is XRD amorphous in nature but, surprisingly it is observed that the oxide layer is crystalline in nature when it is deposited on Cu-nw structure. A single strong peak corresponds to (111) plane of β–MoO_3 is formed. It is also found that the highest intensity peak of Cu_2O which is formed during deposition and Cu-nw are also in (111) direction. Therefore, it was initially thought that probably a strong (111) plane interfacial energy playing a crucial role here to help to form the MoO_3 layer crystalline in (111) direction.

Figure 5.4 represents high-resolution TEM images of plain Cu and MoO_x@Cu nanowires. Cu nanowires are found to be highly crystalline in nature with (111) growth direction with an interplanar spacing of 2.1 Å. The TEM images of MoO_x/Cu hybrid nanorod indicate the uniform MoO_x layer is continuous and conformal. The thickness of the active layer is measured to be around 25 nm, which is consistent with the SEM images obtaineb). All interfaces can be clearly identified from the images. It is also interesting to see that the MoO_3 layer is grown perpendicular manner to the Cu_2O layer. So, there is a probability of epitaxial growth of MoO_3 on Cu_2O or Cu layer. Calculated inter-atomic distances of two planes of MoO_3 observed in HRTEM images are 1.7 Å for (22-2) plane and 1.48 Å for (420) plane, which closely matches with the (220) plane distance of Cu_2O.

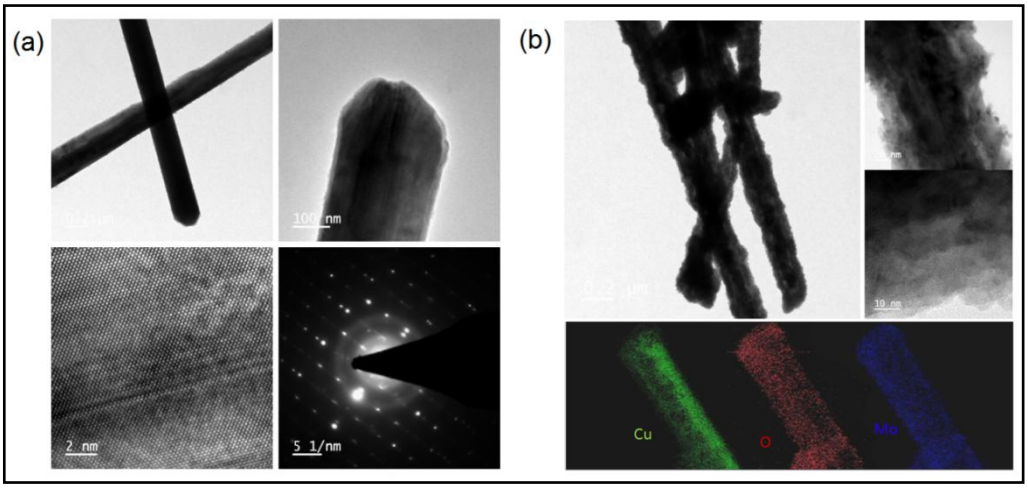


Figure 5.4 High-resolution TEM images of (a) Cu-nw and (b) MoO_x@Cu-nw

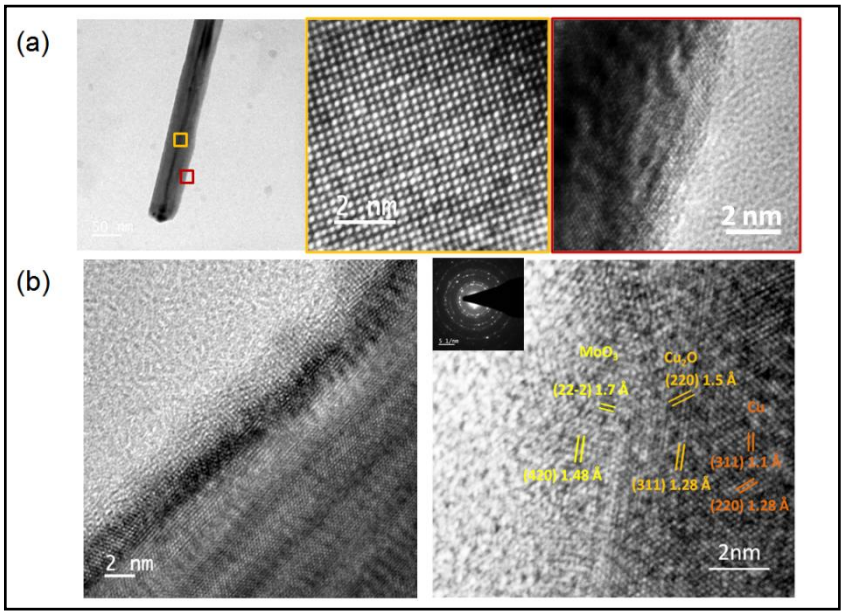


Figure 5.5 HRTEM images of (a) Cu-nw and (b) Cu-MoO_3 interfaces

Furthermore, the same experiment is done on the planar Cu-sheet instead of Cu-nw. Figure xx shows XRD plots and SEM images of molybdenum oxide coated planar Cu-sheet. Here also the same thing is observed, MoO_3 formed to be crystalline and Cu_2O phase appears along with. In the case of Cu-sheet, the intensity of the MoO_3 phase is quite low, which is probably because of the low loading of MoO_3 on planar surface compare to high surface area Cu-nw.

Nevertheless, the formation of crystalline MoO_3 on Cu surface is factual irrespective of any geometry. However, the actual reason of the formation of crystalline MoO_3 is not understood.

Initially, it was thought that the formation of Cu_2O interface is the main reason behind this phenomenon. To establish the fact, we oxidized the Cu surface with ozone with varying time before doing oxide deposition. But, the oxide layer is found to be amorphous with such customized Cu_2O layer before deposition. Thus, Cu_2O layer is not only the reason behind the formation of crystalline MoO_3 layer.

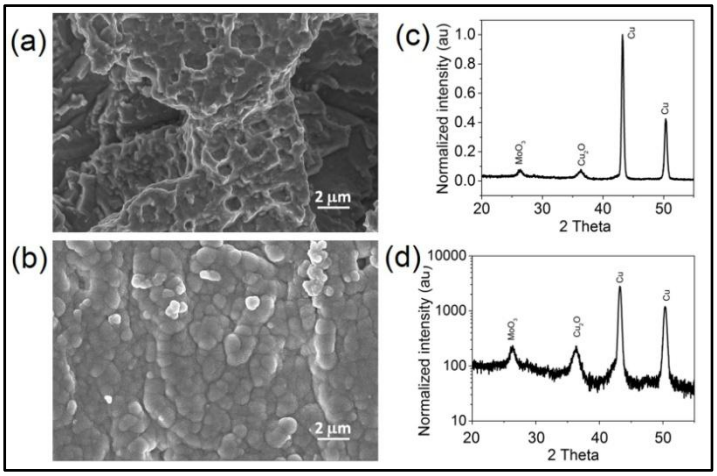


Figure 5.6 Figure 5.7 (a,b) SEM images of pristine and MoO_x coated Cu-sheet respectively and (c,d) XRD of MoO_x coated Cu-sheet and log plot of the same plot respectively

5.1.2 Prevention of Copper oxidation

Copper gets easily oxidized in presence of any oxidant. Formation of the oxide layer is not desired and it creates another insulating path for the electron. There are lots of strategies reported to prevent the oxidation and diffusion of Cu in the literature. It is found that the metal nitrides (like TiN, MoN etc.) and carbides (like WC_x, SiC_x) layers are usually used for a copper diffusion barrier in electronic integrated circuits.[191,192] Jang et al. successfully used molybdenum nitride as an efficient Cu diffusion barrier lower than 600 ^{0}C.[193]

To prevent the Cu_2O formation on the surface, a thin layer of MoN_x layer was applied by ALD on top of the copper surface and then MoO_x was deposited as usual. It is found that around 30 cycles of MoN_x (which is ~3 nm thick) in between Cu and MoO_x found to be the optimized thickness needed to avoid Cu_2O formation. A protective layer of AlO_x was also tried to deposit in between Cu and MoO_x interface by ALD. XRD showed that the AlO_x layer doesn't help to protect Cu surface because of H_2O was used one of the precursors for AlO_x deposition (Figure 5.8).

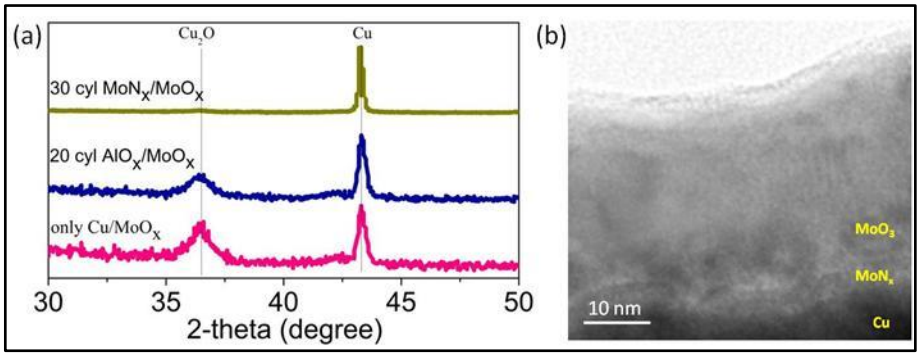


Figure 5.8 protection of Cu from oxidation. (a) XRD of MoO_x/Cu without protecting layer, MoO_x/Cu with AlO_x (20cyl) protection and MoO_x/Cu with MoN_x (30 cyl) protection (b) TEM image of MoNx protection layer sandwiched between Cu and MoO_x layer

5.1.3 Electrochemical characterization

Figure 5.9a represents the cyclic voltammetry (CV) of the bare Cu/MoO_x and MoN_x protected electrodes. Three peaks were obtained from the protected electrode at 2.3, 0.33 and 0.15 V vs. Li/Li^+during the first cathodic sweep when the electrode was cycled within 3.0 V to 0.01 V against Li/Li^+. The broad peak at 2.3 V was ascribed for the irreversible Li^+ insertion into the interlayer of MoO_3.169,170</sup> The other two peaks at 0.33 V and 0.15 V can be assigned to the conversion reaction between MoO_x and Li^+ ion to form Mo metal and Li_2O (MoO_x + xe^- + xLi^+ → Mo + Li_2O).[15] During the anodic sweep, four peaks at 0.45, 1.26, 1.8 and 2.5 V vs Li/Li^+ were observed. The peak at 2.5 V was assigned for the delithiation reaction from unreacted Li_xMoO_x (where $0.3<x\leq0.5$). The peaks at 0.45, 1.26 and 1.8 are originated due to multi-step oxidation of Mo to form MoO_x. Similar observations were also found in previous reports.[16,15,17–19] For the unprotected electrode, peaks obtained in the range of 2-0.8 V during discharge and peak at ~ 2.5 V during charge came due to the formation of Cu_2O layer during MoO_x layer deposition.[20]

Figure 5.9b shows the charge-discharge cycling performance of a protected electrode. The discharge capacity of 1137 mAh g^{-1} is obtained from the first cycle, whereas a capacity of 993 mAh g^{-1} is observed in the second cycle. The electrode produced an average capacity of 960 mAh g^{-1} for 50 cycles of charge-discharge. Rate capabilities of these electrodes are also very promising (Figure 5.9c). Five charge-discharge cycle sequences were carried out at each current density to ensure the stability of the electrodes. A total of approximately 91%, 86.6%, 72.5%, 53.7% and 45.7% of initial capacities are retained when the current density was increased from 0.1 A g^{-1} to 0.2, 0.5, 1, 2 and 4 A g^{-1} respectively. We believe such good rate

capability of the electrodes comes from the MoO_x/Cu core-shell structure, which provides high electronic and ionic conduction through the Cu backbone layer.

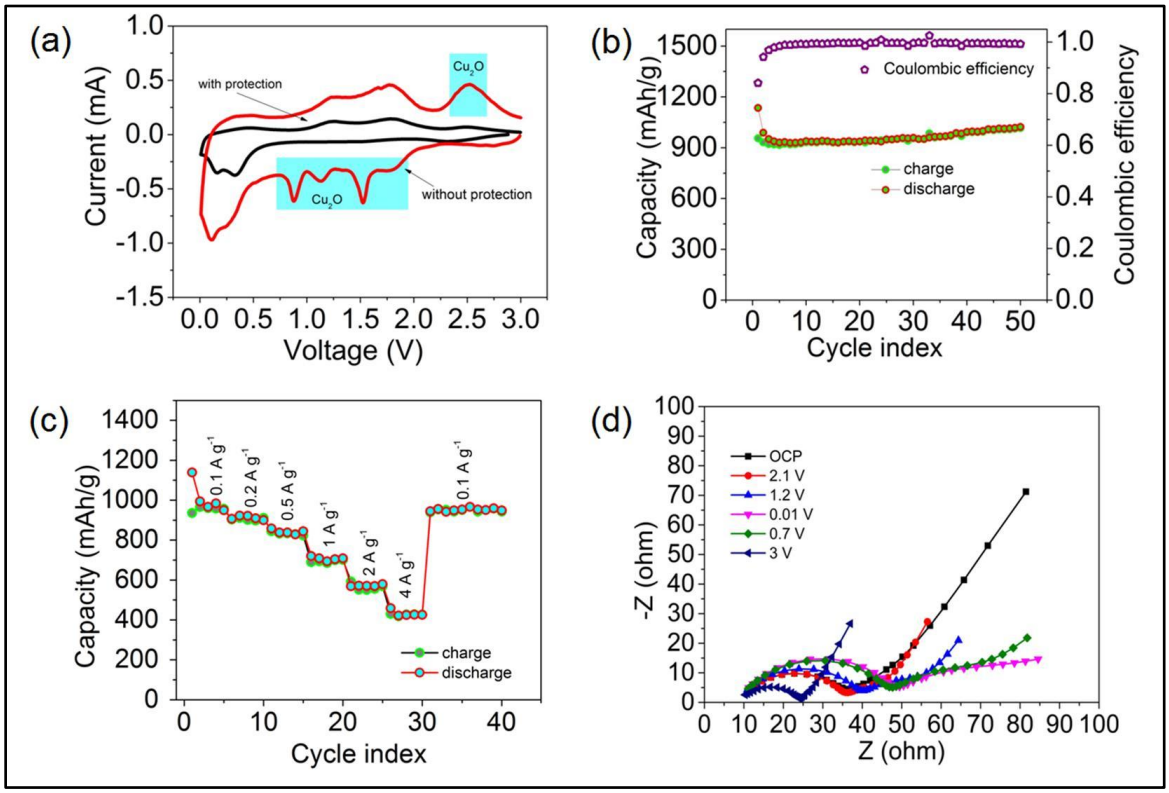


Figure 5.9 Electrochemical activities of a 200 cycle MoO_x ALD coated Cu electrode. (a) Cyclic voltammograms of the electrode with and without protection, (b) charge-discharge cycling, (c) rate performance at different current densities and (d) in-situ electrochemical impedance spectroscopy at different potential during charge-discharge.

The corresponding impedance analysis is carried out to understand the electrochemical behavior during lithiation and delithiation process in Cu/MoO_x electrode. *In-situ* impedance analysis is done during the charge-discharge process at specified potentials as shown in Figure 5.9d. It is found that the electrolyte resistance values remain unchanged for all the measurements which mean that the contribution from electrolyte resistance is independent of charge-discharge behavior. Charge transfer resistance (R_{CT}) which is represented by the first semicircle in the plot, mainly associated with the surface charge transfer, doesn't change much with lithiation till the conversion reaction. The value of R_{CT} increased after the conversion reaction presumed to be due to the formation of resistive LiO_2 matrix in the electrode. The nature of the impedance spectrum doesn't change much while sweeping the potential from 0.01 V to 0.7 V during the charging process, indicating not many electrochemical changes took place in this region. There is a marginal decrease in R_{CT} value

after the full charging process, indicating the electrode doesn't revert back to its initial condition. It was previously also observed that full Li-extraction could not be possible after the first charge and some lithiated phase was still present in the electrode.

5.2 Conclusions

In summary, freestanding Cu/MoO_x nanostructured electrodes are prepared by replacing the CNT template layer via ALD method, and it has been exhibited to be an ideal anode for LIBs. These electrodes demonstrate prominent rate capability and high energy density owing to the high electronic conductivity and stability of hybrid core-shell nanostructure. The nanostructured hybrid electrode delivers a stable capacity of ~960 mAh g^{-1} at a current of 100 mA g^{-1}. Even at very high current (4 A g^{-1}), the electrode retained of 46% of its initial capacity. In 1st discharge, the sample provided a high lithium storage capacity of 1137 mAh g^{-1}. This work demonstrates a promising way to fabricate reliable freestanding 3D nanostructured electrodes using a Cu nanowire template for high-performance LIB anode. Interestingly, it is also observed that the molybdenum oxide deposited on Cu-nw found to be crystalline. It is believed that the formation of Cu_2O layer in between Cu and molybdenum oxide plays a major role in formation of crystalline molybdenum oxide.

References

(1) Taberna, P. L.; Mitra, S.; Poizot, P.; Simon, P.; Tarascon, J. M. High Rate Capabilities Fe3O4-Based Cu Nano-Architectured Electrodes for Lithium-Ion Battery Applications. *Nat. Mater.* **2006**, *5* (7), 567–573.

(2) Liu, D.; Yang, Z.; Wang, P.; Li, F.; Wang, D.; He, D. Preparation of 3D Nanoporous Copper-Supported Cuprous Oxide for High-Performance Lithium Ion Battery Anodes. *Nanoscale* **2013**, *5* (5), 1917–1921.

(3) Ni, S.; Huang, P.; Chao, D.; Yuan, G.; Zhang, L.; Zhao, F.; Li, J. Amorphous GaN@Cu Freestanding Electrode for High-Performance Li-Ion Batteries. *Adv. Funct. Mater.* **2017**, *27* (35), 1–6.

(4) Wang, N.; Hang, T.; Ling, H.; Hu, A.; Li, M. High-Performance Si-Based 3D Cu Nanostructured Electrode Assembly for Rechargeable Lithium Batteries. *J. Mater. Chem. A* **2015**, *3* (22), 11912–11919.

(5) Um, J. H.; Choi, M.; Park, H.; Cho, Y. H.; Dunand, D. C.; Choe, H.; Sung, Y. E. 3D Macroporous Electrode and High-Performance in Lithium-Ion Batteries Using SnO_2 Coated on Cu Foam. *Sci. Rep.* **2016**, *6* (January), 1–9.

(6) Qi, Y.; Du, N.; Zhang, H.; Wang, J.; Yang, Y.; Yang, D. Nanostructured Hybrid Cobalt Oxide/copper Electrodes of Lithium-Ion Batteries with Reversible High-Rate Capabilities. *J. Alloys Compd.* **2012**, *521*, 83–89.

(7) Finke, A.; Poizot, P.; Guéry, C.; Dupont, L.; Taberna, P.-L.; Simon, P.; Tarascon, J.-M. Electrochemical Method for Direct Deposition of Nanometric Bismuth and Its Electrochemical Properties vs Li. *Electrochem. Solid-State Lett.* **2008**, *11* (3), E5.

(8) Bazin, L.; Mitra, S.; Taberna, P. L.; Poizot, P.; Gressier, M.; Menu, M. J.; Barnabé, A.; Simon, P.; Tarascon, J. M. High Rate Capability Pure Sn-Based Nano-Architectured Electrode Assembly for Rechargeable Lithium Batteries. *J. Power Sources* **2009**, *188* (2), 578–582.

(9) Hassoun, J.; Panero, S.; Simon, P.; Taberna, P. L.; Scrosati, B. High-Rate, Long-Life

Ni-Sn Nanostructured Electrodes for Lithium-Ion Batteries. *Adv. Mater.* **2007**, *19* (12), 1632–1635.

(10) Sun, Y. M.; Lee, S. Y.; Lemonds, A. M.; Engbrecht, E. R.; Veldman, S.; Lozano, J.; White, J. M.; Ekerdt, J. G.; Emesh, I.; Pfeifer, K. Low Temperature Chemical Vapor Deposition of Tungsten Carbide for Copper Diffusion Barriers. *Thin Solid Films* **2001**, *397* (1–2), 109–115.

(11) Chen, H. C.; Tseng, B. H.; Houng, M. P.; Wang, Y. H. Titanium Nitride Diffusion Barrier for Copper Metallization on Gallium Arsenide. *Thin Solid Films* **2003**, *445* (1), 112–117.

(12) Jang, Y.; Kim, J. B.; Hong, T. E.; Yeo, S. J.; Lee, S.; Jung, E. A.; Park, B. K.; Chung, T. M.; Kim, C. G.; Lee, D. J.; et al. Highly-Conformal Nanocrystalline Molybdenum Nitride Thin Films by Atomic Layer Deposition as a Diffusion Barrier against Cu. *J. Alloys Compd.* **2016**, *663*, 651–658.

(13) Sun, Y.; Wang, J.; Zhao, B.; Cai, R.; Ran, R.; Shao, Z. Binder-Free α-MoO_3 Nanobelt Electrode for Lithium-Ion Batteries Utilizing van Der Waals Forces for Film Formation and Connection with Current Collector. *J. Mater. Chem. A* **2013**, *1* (15), 4736–4746.

(14) Zhou, L.; Yang, L.; Yuan, P.; Zou, J.; Wu, Y.; Yu, C. α-MoO_3 Nanobelts: A High Performance Cathode Material for Lithium Ion Batteries. *J. Phys. Chem. C* **2010**, *114* (49), 21868–21872.

(15) Lu, P.-J.; Lei, M.; Liu, J. Graphene Nanosheets Encapsulated α-MoO_3 Nanoribbons with Ultrahigh Lithium Ion Storage Properties. *CrystEngComm* **2014**, *16* (29), 6745–6755.

(16) Ahmed, B.; Shahid, M.; Nagaraju, D. H.; Anjum, D. H.; Hedhili, M. N.; Alshareef, H. N. Surface Passivation of MoO_3 Nanorods by Atomic Layer Deposition toward High Rate Durable Li Ion Battery Anodes. *ACS Appl. Mater. Interfaces* **2015**, *7* (24), 13154–13163.

(17) Liu, C.-L.; Wang, Y.; Zhang, C.; Li, X.-S.; Dong, W.-S. In Situ Synthesis of α-MoO_3/graphene Composites as Anode Materials for Lithium Ion Battery. *Mater. Chem.*

Phys. **2014**, *143* (3), 1111–1118.

(18) Ma, F.; Yuan, A.; Xu, J.; Hu, P. Porous α-MoO_3/MWCNT Nanocomposite Synthesized via a Surfactant-Assisted Solvothermal Route as a Lithium-Ion-Battery High-Capacity Anode Material with Excellent Rate Capability and Cyclability. *ACS Appl. Mater. Interfaces* **2015**, *7* (28), 15531–15541.

(19) Martinez-Garcia, A.; Thapa, A. K.; Dharmadasa, R.; Nguyen, T. Q.; Jasinski, J.; Druffel, T. L.; Sunkara, M. K. High Rate and Durable, Binder Free Anode Based on Silicon Loaded MoO_3 Nanoplatelets. *Sci. Rep.* **2015**, *5* (April), 10530 1-5.

(20) Xu, Y. T.; Guo, Y.; Li, C.; Zhou, X. Y.; Tucker, M. C.; Fu, X. Z.; Sun, R.; Wong, C. P. Graphene Oxide Nano-Sheets Wrapped Cu_2O Microspheres as Improved Performance Anode Materials for Lithium Ion Batteries. *Nano Energy* **2015**, *11*, 38–47.

Chapter 6

Summary and Future Sopes

This chapter summarizes the major findings and the achievements of this work. It accordingly describes the importance of the 3D nanostructures prepared by ALD technique for energy storage. It also includes the possible future scopes that can be carried out to achieve a better and safer energy storage device

6.1 Summary and conclusions

The background of this work is to develop 3D nanostructure materials with superior energy density and power density for electrochemical energy storage. Molybdenum oxide is chosen to be the active material for its high capacity and favorable redox reactions towards Li/Li^+ system. ALD method is used to deposit molybdenum oxide (MoO_x) films by using $Mo(CO)_6$ and O_3 as the precursors at 170 ^{0}C. *In-situ* QCM measurements showed a narrow but low ALD temperature window of around 165-175 ^{0}C. RGA study is done to understand and prove two-step half reactions of MoO_x ALD. A series of *ex-situ* characterizations are employed to study this material in detail. The as-grown material has been found to be amorphous in nature but can be converted to a stable crystalline phase upon annealing under ambient. The electrochemical activity of ALD grown MoO_x films is probably first time used against Li/Li^+ system without any carbon or binder and shows comparable electrochemistry with those of conventional MoO_3 anode reported earlier. A slow but gradual capacity fading is observed when the thickness of the films increased because of the resistive nature of the oxide material. 3D hybrid core-shell structure is fabricated by depositing MoOx on MWCNT scaffold layer. Such structure offers better electron and Li transportation. MoO_x thickness is varied to see the effect on capacity and rate performance that enabled to optimize the number of ALD cycles required for the composite. Among all the four different electrodes 300 cycles ALD coated MoO_x/MWCNT electrode possesses an optimized thickness of MoO_x layer in terms of cycling stability and has a moderate areal and specific capacity. Also, that particular electrode showed high capacity retention after 50 cycles (97.5 % with respect to 2nd cycle) with the highest stable capacity of ~915 mAh g^{-1}. This kind of state-of-the-art 3D core-shell nanostructure helps to deposit more amount of active material with the same number of ALD cycles and CNT layer lends a hand to ease the electron transfer during charge-discharge process.

In general, the insulating nature of oxides is one of the major concerns for cycling lifetime. A novel method is used to deal the conductivity issue in oxide materials. Here, different amount of N-atoms are incorporated in a controlled way in the MoO_x layer by ALD technique without reducing the metal centre. N-incorporation is confirmed by *in-situ* QCM study. SIMS measurement proved the uniform distribution of N-atoms throughout the films. Conductivity measurements showed around two orders of magnitude increase after N-incorporation at room temperature. Temperature-dependent Hall measurements showed highly disorder system confirmed by poor hall mobility. The enhancement in conductivity believed to be due to the

formation of shallow level electron donor has positively influenced the electrochemical performance. N-incorporated samples showed enhanced electrochemical activity in terms of energy and power density towards the Li/Li^+ system than the pristine sample.

In the next part, CNT scaffold is replaced by a highly abundant and affordable Cu-nw structure. Thereafter, 3D core-shell nanostructures are prepared by coating MoO_x on Cu-nw template. However, the main problem appeared to be the unwanted oxidation of Cu surface in presence of ozone during ALD process. Protection of Cu is done by applying a thin layer of MoN_x by ALD before the oxide coating. MoO_x/Cu 3D nanostructure showed a capacity of 960 mAh g^{-1} at 0.1 mA g^{-1} and retained 45% of its initial capacity with 40 times higher current rate

6.2 Future scopes

Future works are tabulated as bellow-

- Throughout this work, we discussed the synthesis of highly conformal and controlled 3D nanostructured by ALD method. To this end, the first future work will be to see the full cell capability of those MoO_x 3D structure using commercially available cathode materials like $LiCoO_2$.
- This whole work can be seen as stepping stone for future high performance solid state batteries where controlling active material thickness and pore size would matter the most. Achieving appropriate contact between electrolyte and active material in solid state device is one of the major problems in present scenario.
- Complex, unstable yet excellent and desirable materials like metaphase oxides, phosphides, sulfides, and nitrides can be deposited by ALD method and later on to be used in LIB.
- Fabrication of full cell devices by the monolithic manner which will decrease a lot of resistance and overall weight of the system is also a future prospect.
- All solid-state batteries are in huge demand nowadays where both electrode and electrolyte are in solid state. ALD technique can be a better method to deposit conformal solid electrolyte on the 3D hybrid nanostructure.

Appendix-I

Two-Stage Chemical Bath Deposition of Moo_3 Nanorod Films

In this chapter, we describe the conditions to obtain films of h-MoO_3 by acidification of ammonium heptamolybdate (HMA). A unique two-stage chemical bath deposition (CBD) process is developed. In the first stage, only nucleation occurred on the substrate, followed by film growth during the second stage. Control over the rod length, diameter and orientation is achieved by controlling the deposition conditions.

The aim of this work was to deposit self-standing 3D MoO_3 nanorods on a substrate for the application in LIB as anode material.

7.1 Experimental

MoO_3 films are deposited from a highly acidic bath containing 0.1–0.05 M of HMA and 5.2 M of HNO_3 in a thermostatically-controlled water bath at 85 °C for 1 h. The deposition solution is placed in an airtight glass vial with the FTO-coated glass substrate placed facing down at a roughly 45° angle to the bottom of the vial to avoid accumulation of bulk precipitate on the substrate surface. After deposition, the surface is rinsed thoroughly with DI water before drying with N_2 gas.

For two-stage deposition, 5 ml of 2 M HNO_3 is mixed with 10 ml HMA (concentration varied from 0.1–0.01 M) solution with continuous stirring. About 10 ml of that solution transferred to a vial and kept into a water bath at 85 °C. Then the FTO substrates are placed into the solution as described earlier for another half an hour. This step is considered as nucleation step. After that, substrates are taken out from the solution and rinsed thoroughly with distilled water followed by the growth step where the substrates are again put into the same solution for another half an hour. After deposition, films are washed with distilled water and dried.

7.2 Results and discussions

Under the highly acidic condition, heating of HMA results in precipitation of MoO_3. In this process, isopolymolybdate ions ($Mo_7O_{24}^{6-}$) in the solution are converted to MoO_3 upon heating at 85 °C. X-ray diffraction and SEM imaging confirmed the hexagonal crystallographic nature of the powdery precipitate. Film formation is found only on the FTO surface, no film formation is observed on the glass container surface, activated glass (HNO_3 or $KMnO_4$ treated) or any metal substrates tried by us (stainless steel or Au). However, we did find film growth occurred also on oxide substrate (like TiO_2). We did not devote much effort to trying to understand what is special about the FTO and TiO_2. We do note that, since the solution is highly acidic, all substrates are expected to be positively charged and therefore the reason is unlikely to be due mainly to electrostatic forces. All references to films in this paper refer to films on FTO.

An XRD pattern of a representative as-deposited film is shown in Figure 7.1a. All the peaks can be indexed to the hexagonal phase of MoO_3. Crystallographic analysis of the pattern

reveals $a = b = 10.5756$ Å and $c = 3.7209$ Å which matches with the Rietveld fitting value done by Pan *et al.*[1] as well as with other literature values.[2,3] An SEM image of the same film is shown in Figure 7.1b. A rod-like morphology with rod diameter ranging from 2–10 μm and with flat hexagonal top surfaces is clearly seen. A TEM image of a single rod is shown in Figure 7.1c together with selected point-like ED pattern, reveals the single crystalline nature of the individual rods.

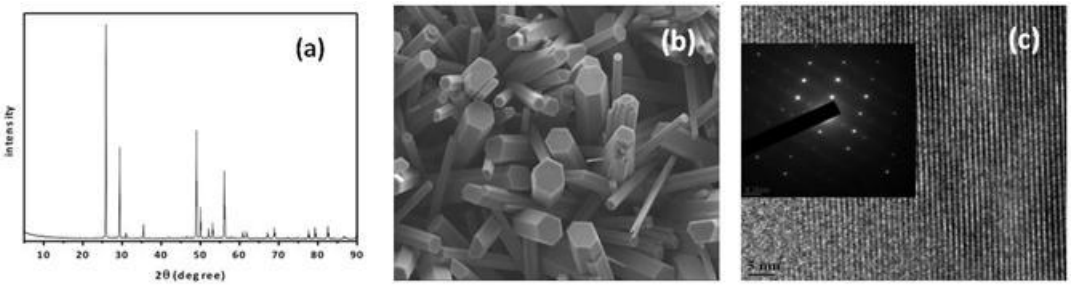


Figure 7.1 (a) XRD pattern of the as-deposited films obtained from 0.1 M HMA and 5.2 M HNO_3 in the Bragg–Brentano configuration. (b) SEM micrograph revealing hexagonal rod-like morphology of the deposit. (c) The TEM image and SAED pattern showing mono crystallinity of the individual rods.

Semi-quantitative XPS elemental analysis of the as-deposited films (Figure 7.3a) shows Mo $3d_{5/2}$ and $3d_{3/2}$ peaks at 232.686 eV and 235.847 eV, agreeing with that reported previously for MoO_3.[4,5] However, a considerable amount of nitrogen at 398.6 eV is observed which is chemically different from the nitrogen in metal nitrides. To understand the chemical nature of the nitrogen in the deposit, we performed FTIR transmission measurements on powder scraped from the substrates. As shown in Figure 7.3c, –NH bending and stretching peaks are clearly observed at *ca.* 1440 cm^{-1} and 3228 cm^{-1} respectively.[2,6] Also absorbance from –OH vibrations is found at 1400, 1610 and 3500 cm^{-1}. The peak at 1600 cm^{-1} corresponds to the deformation of the free water molecule and that at 1410 is probably the MoO–H bending vibration.[2] To understand the nature of the –OH and –NH peaks, samples are annealed at 200 °C. After this annealing, the –OH peak intensity did not change whereas the –NH peak intensity decreased by *ca.* 50%. The lack of change of the water/OH peaks on annealing suggests that these species are inside the crystals rather than predominantly on the surface, where they (at least the water) would be expected to be strongly reduced in concentration on annealing. The N most likely comes from NH_4^+ that is mainly also inside the crystal – either occluded or as $MoO_3 \cdot n NH_3 \cdot m H_2O$.

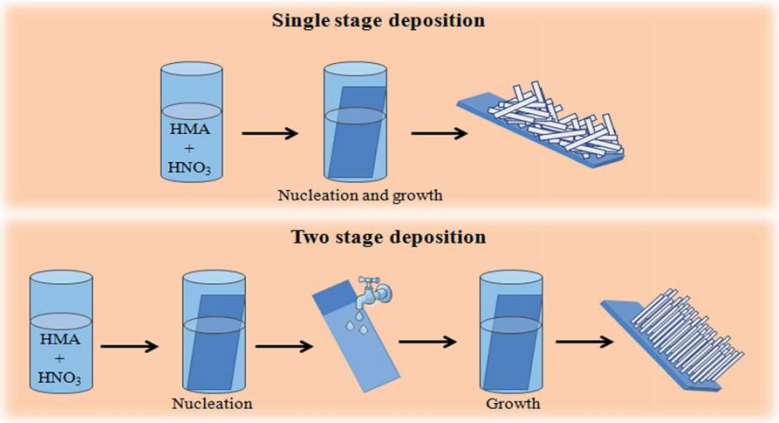


Figure 7.2 Schematic representation of single stage and double stage deposition process of h-MoO_3 nanorod films.

Reducing the relative HMA concentration from 0.1 M to 0.05 M, while keeping the HNO_3 concentration unaltered (5.2 M), resulted in a decrease of both the rod diameter and the surface coverage as shown in Figure 7.4 (a-c). While the rod formation can be attributed to the higher reactivity of the (101) surface, the low material concentration resulted in poor surface coverage. Low ionic concentration favours lower nucleation density on the substrate.

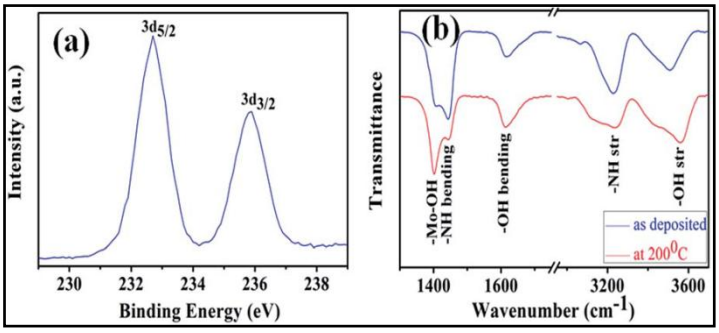


Figure 7.3 (a) XPS Mo peaks obtained from an as-deposited film (b) FTIR transmission spectra showing N–H and O–H stretching and bending vibrations of as-deposited and air-annealed (at 200 ^{0}C) samples.

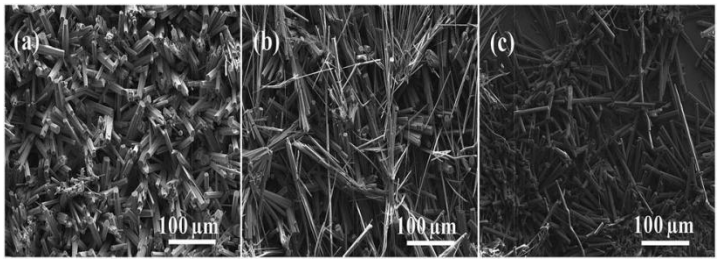


Figure 7.4 Scanning electron micrograph of the films obtained with (a) 0.1 M, (b) 0.065 M and (c) 0.05 M HMA concentration. The HNO_3 concentration was constant at 5.2 M.

The film formation largely depends on the acid concentration in the deposition solution. No visible deposition occurs if the acid concentration is reduced below 5.2 M, other deposition parameters remaining unaltered, although bulk precipitation occurs in the solution even at a much lower acid concentration (>0.05 M). The rate of this precipitation depends on the net acid concentration in the solution. After addition of the acid to the HMA solution at 85 °C, the transparent solution slowly turns increasingly turbid, then gradually transparent again as the suspension precipitates. To exemplify the dependence of these processes on HNO_3 concentration, for 5.2 M HNO_3 with 0.1 M HMA, it takes one min for the solution to become cloudy and another10 min to clear, indicating the completion of bulk precipitation. Reducing the acid concentration, it requires more time for the solution to become turbid and the turbidity persists for a longer time. Thus the reduction in acid concentration in the deposition solution lowers the reaction rate. The above-described behaviour also clearly indicates that homogeneous nucleation occurs in the bulk of the solution, resulting in a suspension that finally precipitates. In parallel with homogeneous nucleation and precipitation, nucleation and growth obviously also occurs on the FTO substrate (but not on most other substrates we tried).

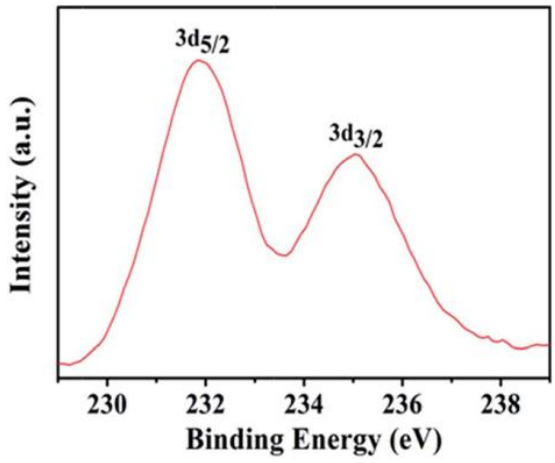


Figure 7.5 Mo 3d XPS spectrum after the 1st stage

However, when a substrate that is removed from the reaction solution after 30 min and showed no visible deposit, is rinsed with DI water and then again immersed in the same (or a fresh) solution, a highly uniform film is deposited. In this paper, we identify such a film as a *second stage* deposition, while the initial 30 min treatment is identified as a *first stage* deposition (Figure 7.2). The bulk precipitation that occurred during the first stage of the two-stage reaction considerably lowered the molybdenum concentration in the solution. Before

describing these deposits, since it is clear that, although no visible deposit formed after the first stage, there is some effect of this first stage treatment, most likely nucleation of some species, we investigated more closely this first stage. We studied the substrate after 30 min in the (5.2 M) deposition solution.

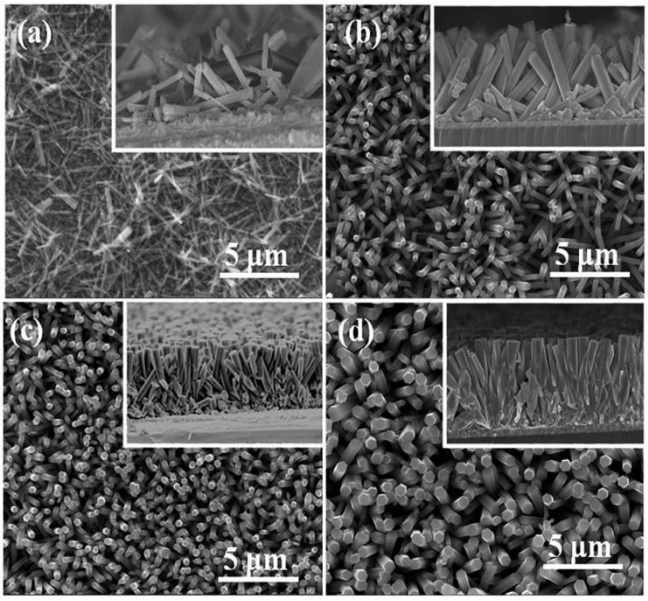


Figure 7.6 SEM images of the as-deposited films obtained from (a) 0.1 M, (b) 0.065 M (c) 0.025 M and (d) 0.01 M of HMA.

While FESEM images revealed no distinct particles that might be attributed to nuclei, XPS clearly indicated the presence of Mo^{+6} species on the substrate (Figure 7.5). The ratio of surface Mo^{+6} to Sn^{+4} (from the FTO substrate) after the first stage is 1 : 4.25. Assuming Mo is in the form of discrete nuclei of a Mo–O material (the most likely expected scenario), this would represent a moderately dense coverage of nuclei with comparable diameter and spacing between the nuclei. Taking into account the relatively close atomic numbers of Mo and Sn, and hence correspondingly low contrast expected, nuclei smaller than *ca.* 10 nm might not be seen in the FESEM. Another, less likely but still possible scenario is that the substrate is covered with a continuous layer, likely to be either amorphous or an adsorbed monolayer. The 1 : 4.25 Mo : Sn ratio measured could then be roughly estimated to correspond to two monolayers of a Mo–O species. The peaks in Figure 7.5 are shifted to lower binding energy by *ca.*0.6 eV in comparison to the reported Mo $3d_{5/2}$ and $3d_{3/2}$ peaks of MoO_3 (in Figure 7.3a). This indicates a different chemical environment of Mo in comparison to the normal MoO_3 lattice. The same XPS peaks of Mo(V), measured in non-stoichiometric amorphous

MoO_3 have been measured to be *ca.* 1 V lower in binding energy compared to Mo(VI) in stoichiometric films.[7]

Figure 7.6 shows SEM images of films obtained after a second stage deposition from a solution that contained 0.65 M HNO_3 and HMA of varying concentrations (0.1, 0.05, 0.025 and 0.01 M, a–d respectively). With reducing HMA concentration in the solution, an increase in the rod diameter and in the film texture is evident. Increase in HMA concentration results in faster bulk precipitation, and it is probable that the actual concentration of soluble Mo species is higher at lower initial HMA concentration and that the concentration falls due to bulk precipitation much more slowly, thus allowing time for more growth. This is supported by the observed effect of aging of the second stage deposition solution.

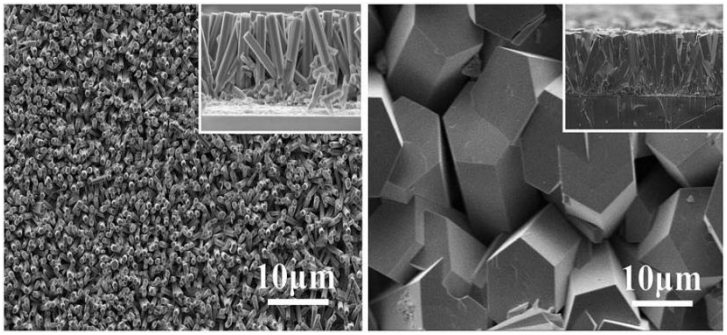


Figure 7.7 SEM images of the films obtained from (a) fresh solution and (b) 30 min aged solution for the 2nd stage deposition. The first stage deposition was kept unaltered at 30 min (the inset shows the cross-section micrograph of the same films).

The chemical bath deposition process consists of two interlinked steps: nucleation and growth. Often these two processes occur simultaneously, resulting in a large particle size distribution in the film. Separating the nucleation and growth stages leads to a narrower size distribution with better control over the film morphology, as demonstrated previously for ZnO nanorod films.[8] Yang *et al.* showed aligned ZnO nanorod arrays on ZnO nanoparticle-coated Si substrates.[9] A pre-nucleated substrate introduces the heterogeneity that assists the growth. The diameter of the rods is primarily determined by the grain size of the ZnO nanoparticles on the seeded substrate. This is also the case where heterogeneous seeding is used, *i.e.* the seed layer is not ZnO but a hydrated Mn oxide.[10]

Since homogeneous precipitation gradually occurs in the second stage solution, the reactant concentrations gradually decrease with time. Therefore we expect similar behavior from a

fresh low-concentration solution and an aged solution with the same eventual concentration as the fresh low-concentration one. Figure 7.7 compares films deposited from a second stage fresh solution (0.025 M HMA and 0.65 M HNO_3) and the same solution, aged for 30 min. We found that the second stage deposition happens also when the concentration of both HMA and HNO_3 is reduced by 50 times, a continuous increase in rod diameter is obtained with a reduction in concentration.

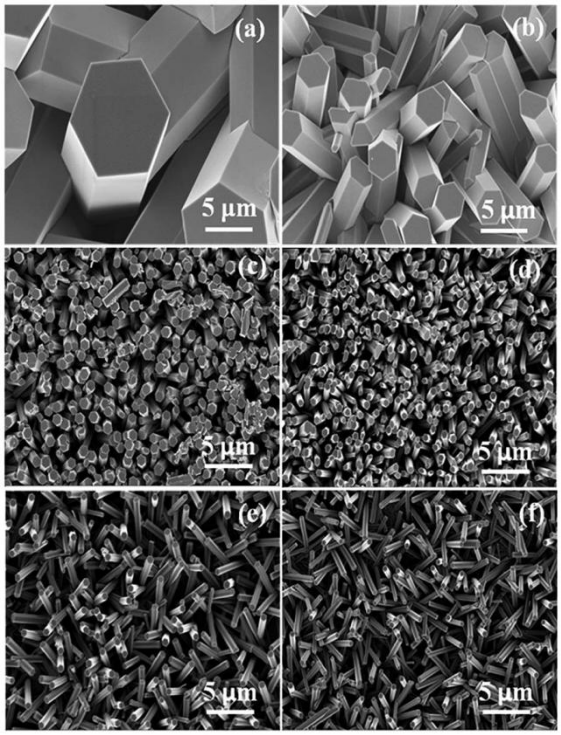


Figure 7.8 SEM image of the films obtained from (a) 2 min, (b) 5 min, (c) 10 min (d) 20 min (e) 30 min and (f) 45 min of 1st stage deposition while the 2nd stage deposition was kept unaltered.

Yet further control of the rod diameter can be obtained by controlling the nucleation at the first stage. Figure 7.8 shows films prepared from a first stage deposition solution containing 0.025 M of HMA and 0.65 M HNO_3. The substrates are taken out from the deposition solution after 2, 5, 10, 20, 30 and 45 min. At the *second stage* of the deposition, these *pre-treated* substrates are re-immersed in the same aged solution kept at 85 °C for 30 min. The shorter the time in the first stage bath, the greater is the width of the rods. This can be explained in general by lower nucleation density on the substrate resulting in larger rods since the same amount of available reactant is divided by a smaller number of nuclei. Figure 7.9 shows a histogram of rod diameters obtained from different films. If nucleation is by a

continuous layer of a Mo species, this explanation could still hold assuming that the layer formation occurs slowly.

We studied the rinsing mechanism in detail to understand the need for the two-stage deposition. Rinsing with water, for example, can cause several changes that might activate the second state deposition process; (a) local change in pH, (b) (another) chemical heterogeneity in the solution, (c) temperature changes at the surface and (d) turbulence.

Rinsing with hot or cold water or even post rinsing heating of the substrate (at 60–70 °C to dry it) has no visible effect in deposition rate. Also stirring the solution or simply shaking it never affected the second stage film growth. The above experiments show that neither temperature changes nor turbulence are likely to initiate the second stage growth.

To understand the effects of local change in pH and the chemical heterogeneity introduced by the rinsing step, we studied the rinsing step extensively by varying the chemical nature of the rinsing medium. There is no difference in film growth or structure if the substrate is rinsed after the first stage process with water (as is normally used) or with acid (both concentrated and dilute), which argues against a pH effect. If the substrate is rinsed with an aqueous solution of high pH (*e.g.*1 M NaOH solution), no deposition occurred during the second stage. However, since Mo oxides and oxide salts are soluble in alkaline solutions, this can be explained by dissolution of Mo–O nuclei formed during the first stage and support the presence of such species after the first stage. However, if the substrate is rinsed with the same solution used in the first stage, there is no deposition in the second stage, regardless of the temperature of the rinsing solution. Therefore, the most likely cause of the rinsing after the first stage leading to deposition during the second stage is some chemical heterogeneity that provides the driving force for deposition in the second stage. Considering the well-known passivation of iron by strong HNO_3, a hypothesis is that rinsing Mo–O nucleation layer removes a passivating film on Mo–O which prevents continued growth during the first stage. However, since growth does occur after rinsing if the nucleated and rinsed substrate is re-immersed in the original solution, this hypothesis would require some difference between the Mo–O species formed in the first stage and that after rinsing with water that prevents the rinsed Mo–O species from being re-passivated. Regardless of the exact mechanism, it is clear that rinsing at the first stage changes the surface of the nucleation layer sufficiently for deposition to continue to occur.

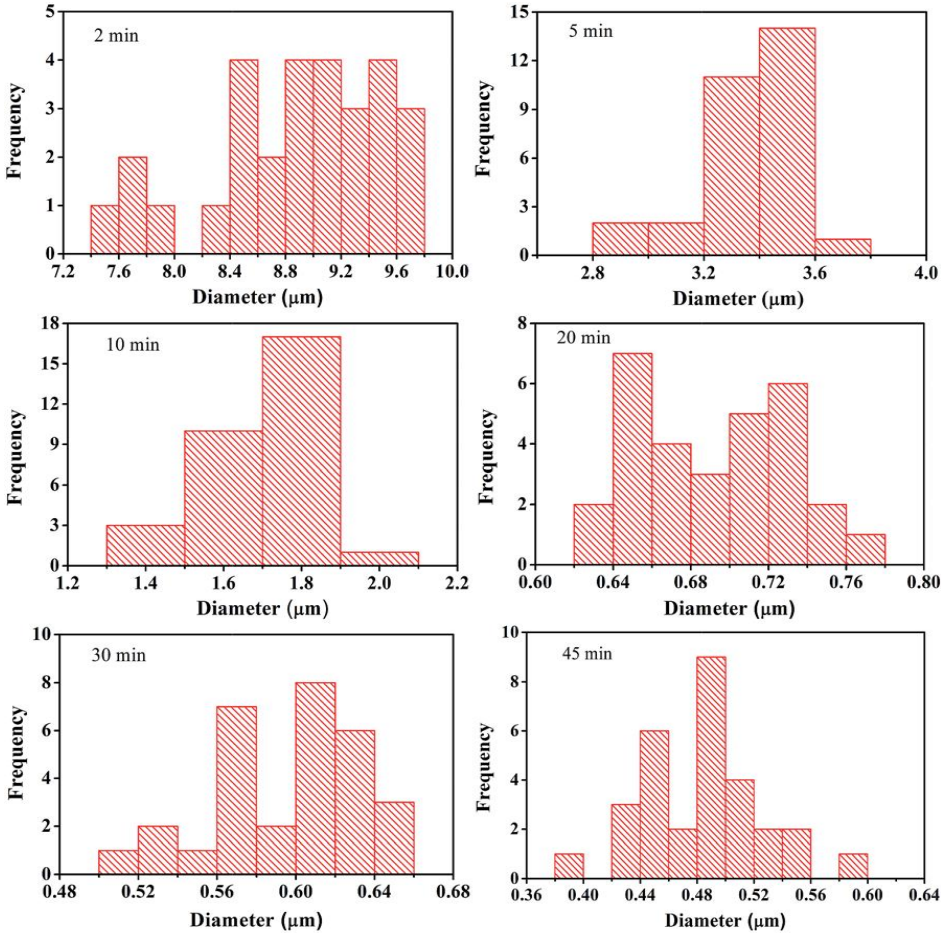


Figure 7.9 Distribution of nanorod diameters of the films obtained from 2 min, 5 min, 10 min, 20 min, 30 min and 45 min of 1ststage deposition while the 2nd stage deposition is kept unaltered.

7.3 Conclusions

Thin films of highly crystalline hexagonal MoO_3 nanorods are deposited by chemical bath deposition. A two-step process where the samples are rinsed between the first and second step is necessary to achieve control over the growth and morphology of the films. Growth at the second stage is believed to be initiated by a chemical change of the nucleation centers formed in the first step caused by the rinsing step. On the other hand, the deposition cannot be done on glass or any metal substrate. Thus, we could not use them as free-standing anode material in LIBs.

7.4 References

(1) Pan, W.; Tian, R.; Jin, H.; Guo, Y.; Zhang, L.; Wu, X.; Zhang, L.; Han, Z.; Liu, G.; Li, J.; et al. Structure, Optical, and Catalytic Properties of Novel Hexagonal Metastable h-MoO_3 nano- and Microrods Synthesized with Modified Liquid-Phase Processes. *Chem. Mater.* **2010**, *22* (22), 6202–6208.

(2) Lunk, H. J.; Hartl, H.; Hartl, M. A.; Fait, M. J. G.; Shenderovich, I. G.; Feist, M.; Frisk, T. A.; Daemen, L. L.; Mauder, D.; Eckelt, R.; et al. "Hexagonal Molybdenum Trioxide" - Known for 100 Years and Still a Fount of New Discoveries. *Inorg. Chem.* **2010**, *49* (20), 9400–9408.

(3) Deki, S.; Béléké, A. B.; Kotani, Y.; Mizuhata, M. Liquid Phase Deposition Synthesis of Hexagonal Molybdenum Trioxide Thin Films. *J. Solid State Chem.* **2009**, *182* (9), 2362–2367.

(4) Song, J.; Ni, X.; Zhang, D.; Zheng, H. Fabrication and Photoluminescence Properties of Hexagonal MoO_3 Rods. *Solid State Sci.* **2006**, *8* (10), 1164–1167.

(5) Lei, Z.; Yang, X.; Dong, J.; Yi, X. Novel Metastable Hexagonal MoO_3 Nanobelts: Synthesis, Photochromic, and Electrochromic Properties. *Chem. Mater.* **2009**, *21* (23), 5681–5690.

(6) Atuchin, V. V; Gavrilova, T. A.; Kostrovsky, V. G.; Pokrovsky, L. D.; Troitskaia, I. B. Morphology and Structure of Hexagonal 3 Nanorods. *Inorg. Mater.* **2008**, *44* (6), 622.

(7) Rouhani, M.; Foo, Y. L.; Hobley, J.; Pan, J.; Subramanian, G. S.; Yu, X.; Rusydi, A.; Gorelik, S. Photochromism of Amorphous Molybdenum Oxide Films with Different Initial Mo^{5+} Relative Concentrations. *Appl. Surf. Sci.* **2013**, *273*, 150–158.

(8) Cheng, H.-C.; Chen, C.-F.; Tsay, C.-Y.; Leu, J.-P. High Oriented ZnO Films by Sol–gel and Chemical Bath Deposition Combination Method. *J. Alloys Compd.* **2009**, *475* (1), 46–49.

(9) Yang, L. L.; Zhao, Q. X.; Willander, M.; Yang, J. H. Effective Way to Control the Size of Well-Aligned ZnO Nanorod Arrays with Two-Step Chemical Bath Deposition. *J. Cryst. Growth* **2009**, *311* (4), 1046–1050.

(10) Kokotov, M.; Hodes, G. Reliable Chemical Bath Deposition of ZnO Films with Controllable Morphology from Ethanolamine-Based Solutions Using KMnO4substrate Activation. *J. Mater. Chem.* **2009**, *19* (23), 3847–3854.

Appendix-II

Low-Temperature Fabrication of Coaxial ALD Cobalt Oxide Coated Carbon Nanotubes and Their Pseudocapacitive Behaviour

This chapter describes the fabrication of low-temperature 3D CoO_x/CNT core-shell structure and their application as supercapacitor electrode. Material fabrication and characterization followed by their electrochemical activities are discussed here.

To extend the effectiveness of 3D hybrid nanostructure, in this work, we report the fabrication of low temperature (50 ^{0}C) ALD cobalt oxide coated MWCNT core-shell structure for its potential application as a supercapacitor electrode. Characterizations of these core-shell structures are performed with the help of several *ex-situ* measurement techniques. We further executed the electrochemical study of these ALD coated MWCNT electrodes with different cobalt oxide thickness. Our synthesis and fabrication strategy would be useful for all the polymer and wearable substrates for energy storage and other applications.

8.1 Experimental

***CNT deposition*:** It is well known that pristine CNTs have nucleation problem because of their inert side walls. So, the as-received MWCNTs are pre-treated with the concentrated acid mixture of HNO_3 and H_2SO_4 (1:3) for 12 hours at room temperature to functionalize CNT surface and also to remove catalyst particles, amorphous carbons and other unwanted species. Acid-treated CNTs are then filtered through the Whatman filter paper and fished several times with DI water followed by drying in a hot air oven. Pre-treated MWCNTs are further added in IPA solution (20 mg of pre-treated MWCNTs in 25 ml of IPA) and sonicated for 15 min. A stable colloidal solution of MWCNTs is then sprayed over cleaned FTO glass substrates of 1×3 cm^2 area heated at 100 ^{0}C. After the deposition, the films are dried at 60 ^{0}C for 12 hours.

ALD of CoO_x: ALD of cobalt oxide is carried out using dicobaltoctacarbonyl [$Co_2(CO)_8$] (Alfa Aeser, USA) and ozone (O_3) precursors in a custom build flow type reactor with N_2 (99.995 %) as the carrier and purging gas. Base pressure of the reactor is fixed at 1 Torr for all the reactions. The reactor chamber temperature is maintained at 50 ^{0}C whereas the precursors are kept at room temperature. Dose time of each precursor is 1 sec followed by 15 sec of N_2 purging. Soda lime glasses and silicon substrates are used to study the film characterizations, whereas MWCNT spray coated FTO glasses are used for the electrochemical characterizations. The schematic representation of CoO_x coating with different ALD cycles on MWCNT electrodes is shown in Figure 8.1.

Electrochemical Characterization: Three electrode electrochemical measurements are done using CHI-604D workstation where CoO_x coated MWCNT electrode behaved as the working electrode, a Pt plate as a counter electrode and Ag/AgCl as a standard reference electrode. Cyclic voltammograms (CVs) are performed with the voltage swept from 0-1 V with different scan rates of 5-50 mV/S. 0.5 M Na_2SO_4 is taken as the electrolyte for all the characterizations.

Full cell devices are fabricated using two symmetrical electrodes separated by a Nafion separator soaked with electrolyte.

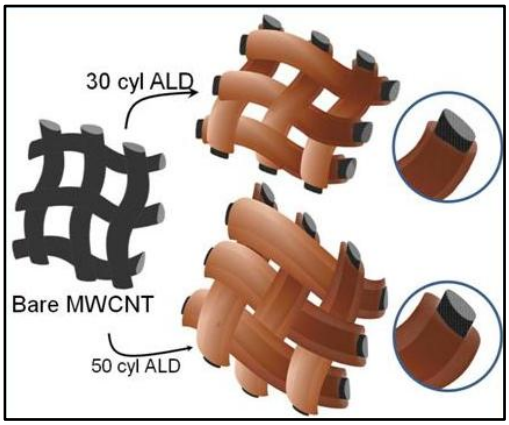


Figure 8.1 Schematic representation of different CoO_x coatings on porous MWCNT layer. As deposited MWCNT layer forms an interconnected mesh kind of structure. ALD helps to deposit cobalt oxide on the free CNT surfaces. Interconnections remain undisturbed after deposition

8.2 Results and Discussion

In-situ residual gas analysis (RGA) study is carried out to explore the possible two-step reaction mechanism during the ALD of CoO_x. RGA is performed with INFICON CPM transceptor gas analyzer consisting of quadrupole mass filter and anion detector. By-products of each half cycle are measured in between 1-100 amu scale with 512 ms of gas dwell time. For the RGA study, Ar is used as the carrier gas instead of N_2 because of the same molecular weight of CO and N_2 (both 28amu). However, during the measurements, Ar is kept off because of a huge peak corresponds to Ar is observed suppressing all other peaks.

The expected by-products of both the half reaction are carbon monoxide along with the un-reacted species. Figure 8.2 shows the spectra taken immediately after $Co_2(CO)_8$ dosing. A single peak at 28 amu represents the emission of CO as the only by-products. We did not find any peak after purging for few second which indicates the completion of the first half reaction. Similarly, for the other half-reaction, the spectrum is taken immediately after dosing ozone into the reactor. As expected, peak at 28 amu came from the CO molecule which got replaced with O to form one layer of CoO_x film. Other peaks coming at 16 and 32 amu are due to the un-reacted atomic oxygen and oxygen molecules respectively. A blank spectrum again is found after purging for few seconds. The next dose of metal precursor showed a similar spectrum as obtained after the first dose of $Co_2(CO)_8$. So the two half-reactions during ALD of CoO_x could be written as follows-

$\Vert$-Co(CO)$_x$* + O_3 → $\Vert$-Co-O* + xCO (A)

$\Vert$-Co-O* + $Co_2(CO)_8$ → $\Vert$-Co-O-Co(CO)*$_x$ + yCO (B)

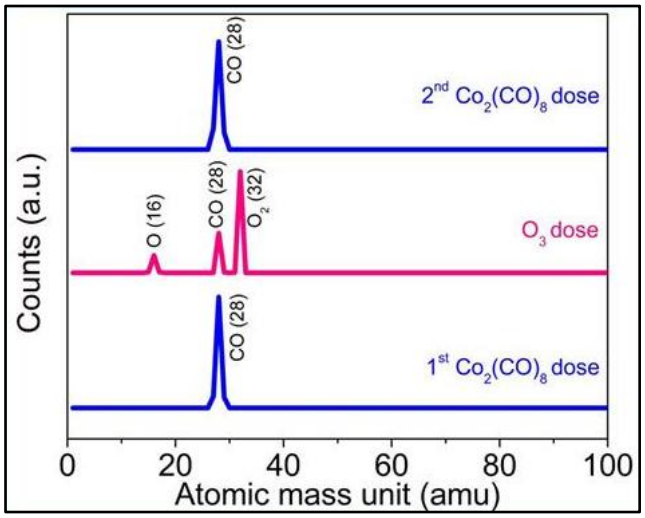


Figure 8.2 RGA spectra recorded after 1st dose of [$Co_2(CO)_8$], 1st dose of O_3 and 2nd dose of [$Co_2(CO)_8$]

Grazing incident XRD (GIXRD) of the as-deposited film showed the presence of both amorphous and mix crystalline phases of cobalt oxide. Peak obtained at 37^0can be attributed to the cubic phase of Co_3O_4 (JCPDS-00-42-1467) whereas the peaks at $43^0$and 62^0 correspond to the cubic phase of CoO (JCPDS-00-048-1719) as shown in Figure 8.3a. However, the as-deposited film completely converted to cubic Co3O4 after annealing at 500 ^{0}C for half an hour under atmospheric condition. A hump at 26^0 present in the CoO_x coated MWCNT films came from the (002) plane of MWCNTs along with the other peaks as obtained in as-deposited CoO_x film.

Figure 8.3b shows the full XPS survey of an as-deposited film along with the individual peaks for Co 2p electrons. The two peaks obtained at 780.5 and 795.8 eV correspond to the binding energy of 2p3/2 and 2p1/2 electrons of Co.[1] XPS peaks for cobalt in both CoO and Co_3O_4 appear exactly at these same binding energies. So only the careful study of satellite peaks can give a hint about the valency state of cobalt. In our case, the film contains both CoO and Co_3O_4mix phase making it very difficult to differentiate between Co(II) and Co(III) states.No other impurities in the as-deposited film are observed except a small amount of carbon. The presence of carbon at this low-temperature ALD is expected from any of the metal organic precursors. The further calculation of the ratio of oxygen to cobalt in the as-deposited film is estimated by taking the ratio of the normalized area of the XPS peaks

divided with their corresponding sensitivity factor. The ratio of O to Co came out to be ca. 1.12 indicating the as-deposited film as a mixture of CoO and Co_3O_4.

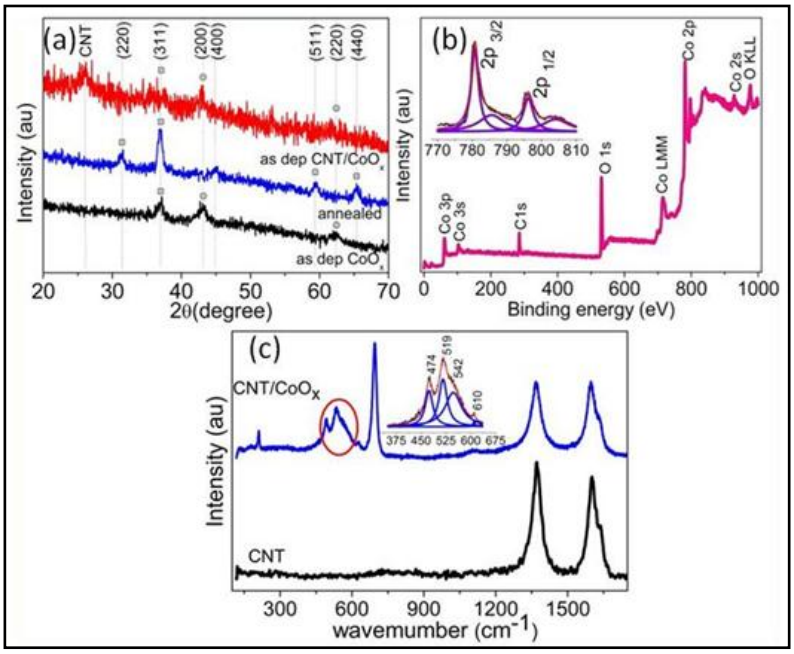


Figure 8.3 (a) Grazing incident XRD of as-deposited film, (b) XPS survey of the as-deposited and inset showing the 2p peaks of Cobalt and (c) Raman spectra of MWCNT and CoOx@MWCNT

Raman spectroscopy of the bare MWCNT and as-deposited CoO_x coated MWCNT films are performed to characterize the material further (Figure 8.3c). As shown in the XRD of the as-deposited film, it consists of individual CoO phase as well as Co_3O_4 both of which not being very strongly crystalline leaves some amorphous nature in the film. However, the annealed film exhibits all of the five Raman active modes that can be assigned to Co_3O_4. The peaks located at 197, 519, 610cm^{-1} are corresponding to F_{2g} whereas the peak at 484 and 684 cm^{-1} correspond to E_g and A_{1g} Raman active modes of Co_3O_4.[2–5] The broad peak at 542 cm^{-1} corresponds to CoO asymmetric stretch (A_g).[2,4] Other two vibration modes of CoO at 516 and 682 cm^{-1} overlaid with the Co_3O_4 peaks. Peaks at 1365 and 1590 cm^{-1} are attributed to D and G vibration modes of CNTs.

SEM images of different ALD cycle CoO_x coated MWCNTs are shown in Figure 8.4. As deposited CNT layer make a mesh kind of interlinked structure where all the CNTs are connected with each other. ALD helps to deposit on the exposed surface of the CNTs without disturbing the interconnection points. A highly uniform coating is seen throughout the electrodes because of the conformal nature of ALD reactions. The outer diameter of the CNTs increases with increasing ALD cycles without cluster or bundle formation. On the other hand,

increasing ALD cycles eventually leads to the fewer pore dimensions left in the structure. The porosity almost disappeared for the electrodes prepared with 100 or more cycles of ALD.

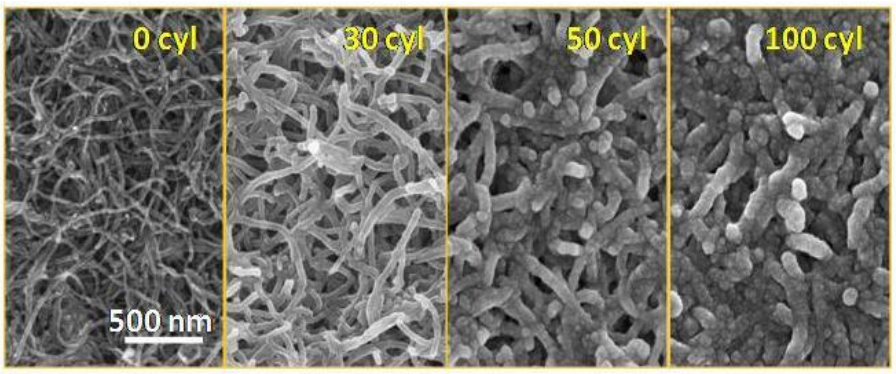


Figure 8.4 surface SEM images of different CoO_x/MWCNT electrodes

Figure 8.5 (a,b) shows the TEM images of a 50 ALD cycle CoO_x/MWCNT sample. Highly uniform and conformal core-shell structure is formed and there are no CNTs which can be found uncoated. The coating of CoO_x consists of small nanocrystals covered homogeneously on CNT surface. High-resolution image shows that the formation of 18-20 nm CoO_x layer (growth rate of approximately 4 Å/cycle slightly below than that of the planar sample which is around 4.5 Å/cycle) obtained from 50 cycles of ALD reaction. Selective area electron diffraction (SAED) pattern of MWCNT and as deposited CoO_x coated MWCNT is shown in Figure 8.5 (c,d). Four crystal planes of MWCNTs viz. (002), (100), (101), (004) are clearly visible in both of the SAED patterns. The co-centric rings obtained from CoO_x/MWCNT structure once again proved the presence of both CoO and CO3O4 phases. Rings with d-values of 4.65, 2.82, 1.84 Å can be indexed to the (220), (311) and (111) planes of Co_3O_4 (JCPDS 00-42-1467) whereas (200) and (220) planes with d-values of 2.3 and 1.6 Å has come from the CoO phase (JCPDS 00-048-1719).

In order to know the charge storage and redox characteristics of MWCNT and 30cyl, 50cyl and 100cyl ALD electrode films, cyclic voltammograms (CVs) are recorded in 0.5M $NaSO_4$ in working potential range from 0.0V to 1.0V. The CV of all samples are recorded in 3 electrode cell arrangement with Ag/AgCl as a reference electrode, platinum as a counter and the MWCNT/CoO_x, deposited films as working electrodes. The comparative CV curves at 5mV/s in Figure 8.6a clearly shows that maximum current response is found to be in 30cyl and a further increase in the ALD cycles resulted in a decrement in the charge storage capacity. The specific capacitance values calculated from the CV curves are as follows: 778 F/g (30cyl), 461 F/g (50cyl), 205 F/g (100cyl) and 59.5 F/g (CNT). The large capacitance in 30 cyl is could be assigned to

the fast ion diffusion and good electronic conduction of the 30cyl MWCNT/CoO_x electrode, the decrement of specific capacitance value with increasing electrode film thickness is attributed to the compact MWCNT/CoO_x film growth in ALD process. Furthermore considering the electrode morphology the MWCNT/CoO_x film deposited for 30cyl is more porous as compared to 50cyl and 100cyl. Interparticle porosity of the electrode material is very crucial for the electrochemical performance and the dense MWCNT/CoO_xfilms with increasing ALD cycles showed dense morphology that consequently inhibits the bulk contribution of the electrode materials. Different scan rate CV of 30cyl in Fig. (b) showed the optimum rate capability of the MWCNT/CoO_x electrode from a fast scan of 100 mV/s to 5 mV/s.

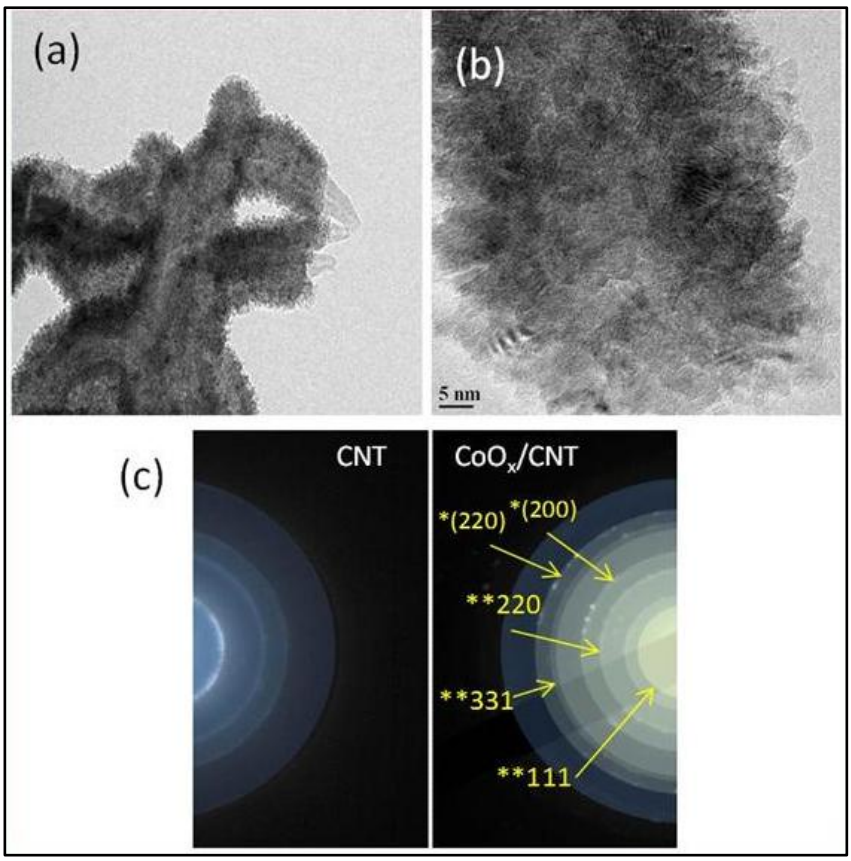


Figure 8.5 (a,b) TEM images of CoO_x/MWCNT structure showing the core-shell structure throughout all the MWCNTs, (c) SAED pattern of MWCNT and CoO_x/MWCNT sample

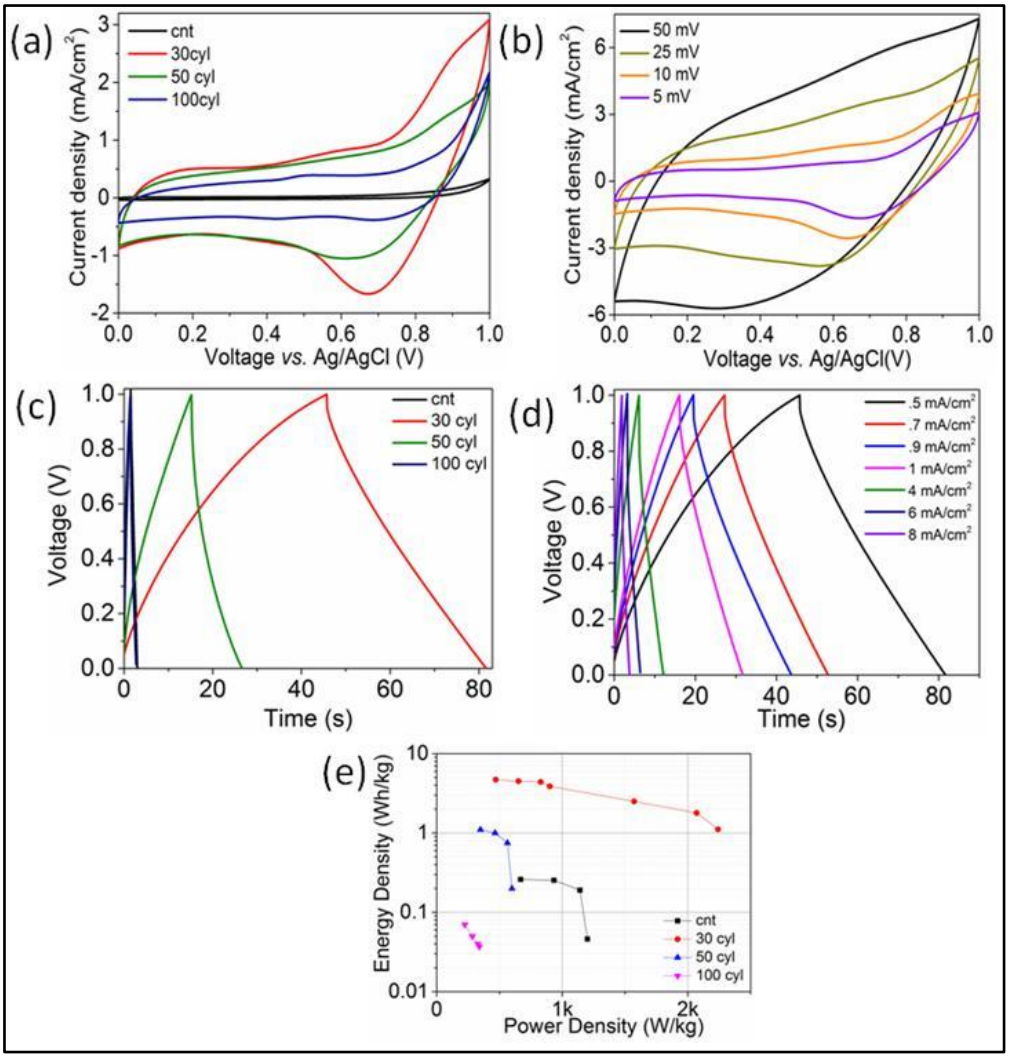


Figure 8.6 (a) CV curves of MWCNT, 30cyl, 50cyl and 100cyl at 5mV/s, (b) 30cyl CV at different voltage sweep rate, (c) GCD graph of all four device at 0.5 mA/cm^2, (d) 30cyl GCD curves at different current loads, (e) Ragone plot showing energy and power density of all four symmetric device.

The supercapacitor device characteristics of all four electrodes are tested by making their symmetric supercapacitor using a Nafion membrane as a separator. The GCD (Galvanostatic charge-discharge) curves at a same current load of 0.5 mA/cm^2 in Figure 8.6(c) depicts that maximum time is taken by MWCNT/CoO_x electrode deposited for 30cyl. The device capacitance calculated from GCD cycles are found to be 2.92 F/g (MWCNT), 38.19 F/g(30cyl), 10 F/g(50cyl) and 0.95 F/g(100cyl). It is worth mentioning that except 30cyl deposited MWCNT/CoO_x electrode no other device works beyond 1 mA/cm^2. Further, the MWCNT/CoO_x film deposited for 30cyl demonstrated low *iR-drop* compared to other thick CoO_x film electrodes. *iR-drop is* an important feature of the device to exhibit high capacitance. The energy density at particular power density delivery are calculated as 30cyl (4.7 Wh/kg @ 470 W/kg) > 50cyl (1.1 Wh/kg @ 347.6 W/kg) > CNT (0.26 Wh/kg @ 667.4

W/kg) > 100cyl (0.07 Wh/kg @ 223.21 W/kg) respectively (Figure 8.6e). These values are interesting and reveal that the ALD film thickness is an important parameter that significantly affects the device performance.

8.3 Conclusion

ALD helps one to deposit uniform metal oxide coating on porous CNT, hence offer a novel strategy in fabricating binder-free supercapacitor electrodes. Unlike batteries, a very thin oxide layer is required for supercapacitor electrodes because the reactions occur at the surface only. Thicker layer will add more resistance to the system. In this work also, electrode with thinnest CoO_x layer performs better than other.

8.4 References

(1) Burriel, M.; Garcia, G.; Santiso, J.; Abrutis, A.; Saltyte, Z.; Figueras, A. Growth Kinetics, Composition, and Morphology of Co_3O_4 Thin Films Prepared by Pulsed Liquid-Injection MOCVD. *Chem. Vap. Depos.* **2005**, *11* (2), 106–111.

(2) Melendres, C a; Xu, S. In Situ Laser Raman Spectroscopic Study of Anodic Corrosion Films on Nickel and Cobalt. *Corrosion* **1984**, *131* (10), 2239–2243.

(3) Hadjiev, V. G.; Iliev, M. N.; Vergilov, I. V. The Raman Spectra of Co_3O_4. *J. Phys. C Solid State Phys.* **1988**, *21* (7), L199–L201.

(4) Jing Yang, Hongwei Liu, Wayde N. Martens, and R. L. F. Synthesis and Characterization of Cobalt Hydroxide, Cobalt Oxyhydroxide, and Cobalt Oxide Nanodiscs. *J. Phys. Chem. C* **2010**, *13* (114), 111–119.

(5) Choi, H. C.; Jung, Y. M.; Noda, I.; Kim, S. Bin. A Study of the Mechanism of the Electrochemical Reaction of Lithium with CoO by Two-Dimensional Soft X-Ray Absorption Spectroscopy (2D XAS), 2D Raman, and 2D Heterospectral XAS-Raman Correlation Analysis. *J. Phys. Chem. B* **2003**, *107* (24), 5806–5811.

List of Publications (Published)

[1] **A. Dhara**, G. Hodes, and S. K. Sarkar, "*Two stage chemical bath deposition of MoO_3 nanorod films*," *RSC Adv.*, 53694–53700, 2014.

[2] D. K. Nandi, U. K. Sen, S. Sinha, **A. Dhara**, S. Mitra, and S. K. Sarkar, "*Atomic layer deposited tungsten nitride thin films as a new lithium-ion battery anode*," *Phys. Chem. Chem. Phys.*, 17445–17453, 2015.

[3] D. K. Nandi, J. Manna, **A. Dhara**, P. Sharma, and S. K. Sarkar, *Atomic layer deposited cobalt oxide: An efficient catalyst for $NaBH_4$ hydrolysis*, *J. Vac. Sci. Technol.*A, 01A115, 2016.

[4] D. K. Nandi, U. K. Sen, **A. Dhara**, S. Mitra, and S. K. Sarkar, "*Intercalation Based Tungsten Disulfide (WS_2) Lithium Battery Anode, Directly Grown by Atomic Layer Deposition*" RSC Adv., 38024-38032, 2016.

[5] **A. Dhara**, D. K. Nandi, U. K. Sen, S. K. Sarkar and S. Mitra, "*Controlled 3D Carbon Nanotube Architecture Coated with MoO_x Material by ALD technique: A High Energy Density Lithium-ion Battery Electrode*" *Advance Materials Interfaces*, 2017.

[6] C. Das, B. Ananthoju, **A. Dhara**, M. Aslam, S. K. Sarkar, and K. R. Balasubramaniam, *Electron-Selective TiO_2/CVD-Graphene Layers for Photocorrosion Inhibition in Cu_2O Photocathodes*, *Advance Materials Interfaces*, 2017.

Manuscript Under Preparation

[1] **A. Dhara**, S. Mitra and S. K. Sarkar, *Development of Nitrogen Incorporated Molybdenum Oxide by Atomic Layer Deposition and Its Enhanced Electrochemical Activity*.

[2] **A. Dhara**, Vikrant Sahoo, Dip K Nandi, Raj K Sharma and Shaibal K Sarkar, *Low temperature fabrication of coaxial ALD cobalt oxide coated CNT nanostructured electrodes and their pseudocapacitive behaviour*.

[3] **A. Dhara**, Sagar Mitra and Shaibal K Sarkar, *Cu-NW supported ALD molybdenum oxide hybrid nanostructure for high performance lithium ion battery anode*.

Acknowledgements

After an intensive period of several years, today is the day: writing this note of thanks for my thesis gives a great happiness and bliss. It's been an extreme learning process for me in the scientific arena as well as on a personal level. I would like to express my gratitude to those without whom this journey would not have been completed.

Firstly, I would like to express gratitude to my advisors Prof. Shaibal K Sarkar and Prof. Sagar Mitra for the continuous support throughout my Ph.D. study and research, without their constant contribution and effort this work would not have been possible. Thank you, sir, for being there for me always. Next, I express my deep respect for my research progress committee (RPC) members Prof. Balasubramaniam Kavaipatti and Prof. Parag Bhargava for their invaluable suggestions during year wise evaluation. My sincere gratitude goes to all the former and present head of the departments Prof. Anurada Ganesh, Prof. Santanu Bandopadhyay and Prof. Rangan Banerjee for providing all the facilities during my stay at IITB. I am also grateful to SAIF and Department of Physics for providing several instrumental facilities during my research work.

I express my sincere gratitude towards Dr. Uttam Sen, Dr. Soumyadeep Sinha and Dr. Dip Nandi whose direct involvements and expertise in battery and ALD made a significant part of this thesis feasible. A massive credit goes to all my co-authors, it was pleasure working with them. I thank all of them from bottom of my heart.

A big credit goes to all my nicest labmates from 'Devices and Interfaces Lab' and 'Electrochemical Energy Lab' where I spent most of the time during my PhD. Special thanks to seniors Dr. Neelam, Dr. Soumyadeep, Dr. Devika, Dr. Suman, Dr. Debabrata and Dr. JK for inspiring me trough their scientific and social knowledge. A big thank you to my collegues Dr. Anand, Dr. Neha, Ansuman, Roja, Vidya and Sudeshna. I express my love towards all the juniors Bireswar, Alok, Aditya and Gaurav. I also thank all my past labmates. The list cant be completed without mentioning Mr. Vilas, Mr. Arvind and Mrs. Rupali for their help whenever needed during my stay.

I would like to extend my thank from my friends Subhankar, Tathagata, Binayak, Pranay, Vikul, Hrusikesh, Nitish, Vikas, Uttam, Sreeparna, Arpita, Bandita to my seniors Dr. Som

Mandal, Dr. Joydev Mana, Dr. Debanand Singdeo all of you whose close association made this journey so beautiful.

I sincerely acknowledge MHRD for proving scholarship and NCPRE, IRCC, SERIIUS, IIT Bombay for providing the fund during my research from all prospects.

Finally, it’s the family, without their support it’s impossible to think about my existence. I have no words to convey my regards and love to them. All I can do is thank god for keeping them in my life.